Order Number 9417515

Low temperature charge transfer

Xia, Bo, Ph.D.

City University of New York, 1994

U·M·I
300 N. Zeeb Rd.
Ann Arbor, MI 48106

LOW TEMPERATURE CHARGE TRANSFER

by

Bo Xia

A dissertation submitted to the Graduate Faculty in Physics in partial fulfillment of the requirements for the degree of Doctor of Philosophy, The City University of New York.

1994

This Manuscript has been read and accepted for the Graduate Faculty in Physics in satisfaction of the dissertation requirement for the degree of Doctor of Philosophy.

11/24/93 — Narciso Garcia
Date — Chair of Examining Committee

11/30/93 — Joseph B. Krieger
Date — Executive Officer

Arthur Damask

Michael A. Gurvitch

Leonard O. Roellig

Myron Strongin
Supervisory Committee

The City University of New York

Abstract

Low Temperature Charge Transfer

by

Bo Xia

Advisor: Dr. Myron Strongin

Alkali metal-ammonia films were chosen as a vehicle to study the phenomena of low temperature charge transfer. Photoelectron spectroscopy and resistivity measurements were used to detect small changes within these films. The results of the resistivity measurement show that some chemical reactions happened in the alkali metal-ammonia films at temperatures as low as 7 K. As the sample temperature increased to above 25 K, drastic changes were observed in both photoelectron spectroscopy and resistivity measurement. In the resistivity measurement, the film resistance decreased and the change was irreversible, which is contrary to the results of the controlled experiment using alkali metal-inert gas films. The resistance change with temperature in these control films is a purely physical process and gives us basis

for understanding the chemical process in the alkali metal-ammonia films. In the photoemission spectra for the alkali metal-ammonia films, peaks which have molecular nitrogen characteristics were observed. A modified Mott's low temperature oxidation model was used to interpret the experimental results. Electrons tunneling into the ammonia media and dissolving into it are the cause for the low temperature chemical reactions in the alkali metal-ammonia film. Experimental results demonstrated that a small amount of ammonia-covered alkali metal films did not show any chemical changes with temperature and significant amount of ammonia was needed in order to observe the irreversible changes in alkali metal-ammonia films.

The last chapter of the thesis is a photoemission study of ytterbium-C_{60} bilayers at room temperature. The experimental results are compared to those reported for alkali metal fullerides and ytterbium isolated in xenon or solid ammonia.

ACKNOWLEDGEMENTS

I am very grateful to Dr. Myron Strongin for the opportunity to work and learn under his direction, for his support, advice and continual source of ideas throughout the whole thesis work, for many discussions and conversations with him in which the real physics always emerged and for the critical reading of the manuscript.

I will always remember that it was Dr. Arthur Damask and Dr. Narciso Garcia who introduced me into Brookhaven National Laboratory, one of the great institutions in the world. I am grateful to Dr. M. W. Ruckman and Dr. P. D. Johnson for their help, support and discussions. I thank Mr. J. F. Moore, Dr. M. A. Gurvitch and Dr. L. O. Roellig for proof reading the manuscript. I also thank Mr. Fran Loeb for his technical support.

I give special thanks to my wife Fang Shi and my parents, Gui-fen Liu and Xi Xia, for their continuing encouragement and support.

This work was supported by the U.S. Department of Energy under contract DE-AC02-76CH00016.

Brookhaven National Laboratory, New York

November, 1993

Table of Contents

Chapter 1. Introduction..... 1

Chapter 2. General Background for the Conductivity of Thin Films..... 6

2.1 Homogeneous Films..... 6

2.2 Granular Films..... 7

2.3 Hopping Conductivity..... 9

2.4 Charging Energy and Conductivity..... 13

Chapter 3. Experimental Techniques..... 18

3.1 Introduction..... 18

3.2 Sample preparation..... 22

3.3 Photoelectron Spectroscopy (PES)..... 26

3.4 X-ray Absorption Spectroscopy (XAS)..... 34

Chapter 4. Physical Properties of Discontinuous Film: an Introduction to Chapter Five..... 43

4.1 Introduction..... 43

4.2 Experimental Details..... 44

4.3 General Properties of Granular Metal Film..... 46

4.4 Effect of Dielectric Media on Film Resistance.... 57

Chapter 5. Study of Low Temperature Charge Transfer in Alkali Metal-Ammonia Thin Film..... 69

5.1 Introduction..... 69

5.2 Resistivity Study of Alkali Metal-Ammonia Films...71

5.3 Photoemission Study of Ammonia-Potassium Films....87

5.3.1 Experimental Details.....87

5.3.2 Work Function Change of Ammonia-Potassium Films...88

5.3.3 PES Study of Ammonia-Potassium Films.....91

5.3.4 NEXAFS Study of Ammonia-Potassium Films.....100

5.4 A Discussion of Possible Models.....105

5.4.1 Solvation Model.....105

5.4.2 Reaction Model.....110

Chapter 6. Photoemission Study of Yb-C_{60} System.....118

References.....138

List of Figures and Tables

Figure 3.1 Layout of experimental chamber.....20

Figure 3.2 Energy dependence of the electron mean free path.....28

Figure 3.3 Schematic of the potential of diatomic molecules.....37

Figure 3.4 Energy level diagram and schematic photoemission spectra at different photon energies.....39

Figure 4.1 Annealing of a granular potassium film.....49

Figure 4.2 Temperature dependence of the resistance for a potassium film (lnR versus $T^{-0.5}$).....52

Figure 4.3 Temperature dependence of the resistance for a gold film (lnR versus $T^{-0.5}$).....53

Figure 4.4a Temperature dependence of the resistance for a gold film (lnR versus 1/T).....54

Figure 4.4b Temperature dependence of the resistance for a gold film (lnR versus $T^{-0.25}$).....55

Figure 4.4c Temperature dependence of the resistance for a gold film: a computer curve fitting result....56

Figure 4.5 The time volution of xenon condensed on a potassium film.....58

Figure 4.6 The time evolution of xenon condensed on a gold

film..... 60

Figure 4.7 The effect of xenon as a dielectric media on the film resistance of a granular potassium film.. 61

Figure 4.8 The effect of xenon as a dielectric media on the film resistance of a granular gold film..... 62

Figure 4.9 The time evolution of krypton condensed on a granular gold film..... 65

Figure 4.10 Comparison of the film resistance of a granular gold film before introducing krypton and after removing krypton by warming up to 90 K..... 66

Table 4.1 Dielectric constants of xenon and krypton..... 68

Figure 5.1 The time evolution of ammonia condensed on a granular potassium film..... 72

Figure 5.2 The potassium film resistance change with time at different temperatures..... 76

Figure 5.3 The time evolution of ammonia condensed on a granular lithium film..... 80

Figure 5.4 The time evolution of ammonia condensed on a granular sodium film..... 81

Figure 5.5 The time evolution of ammonia condensed on a granular caesium film..... 82

Figure 5.6 Annealing curve for potassium deposited into a solid ammonia matrix..... 83

Figure 5.6a Curve fitting result for potassium deposited into solid ammonia matrix.....84

Figure 5.7 The time evolution of ammonia condensed on a potassium film using AC measurement.....86

Figure 5.8 Work function change versus ammonia exposure for potassium at different temperatures..... 89

Figure 5.9 Valence band photoemission spectra of 3 L NH_3 condensed on a potassium film at different temperatures..... 92

Figure 5.10 K 2p core level spectra of 3 L NH_3 condensed on a potassium film at different temperatures.... 96

Figure 5.11 N 1s core level spectra of 3 L NH_3 condensed on a potassium film at different temperatures.... 97

Figure 5.12 N K-edge NEXAFS spectra of 3 L NH_3 condensed on a potassium film at different temperatures... 101

Figure 5.13 Schematic energy diagram for the ammonia-potassium system..... 107

Figure 5.14 The time evolution of different amount ammonia condensed on a granular lithium film..... 114

Figure 6.1 Schematic illustration of a C_{60} molecule..... 119

Figure 6.2 Valence band photoelectron spectra for the incremental deposition of C_{60} on Yb..... 122

Figure 6.3 Valence band photoelectron spectra for the incremental deposition of ytterbium on a fullerene film..... 125

Figure 6.4 Valence band photoelectron spectra for ytterbium deposited on a xenon film..... 130

Figure 6.5 Valence band photoelectron spectra for ytterbium isolated in solid ammonia..... .131

Figure 6.6 Computer based fitting of the valence states 0-4 eV below the Fermi level for Yb deposited on C_{60}.....134

List of Abbreviations

AES	Auger Electron Spectroscopy
AEY	Auger Electron Yield
CMA	Cylindrical Mirror Analyzer
EDC	Energy Distribution Curve
EELS	Electron Energy Loss Spectroscopy
EXAFS	Extended X-ray Absorption Fine Structure
FWHM	Full Width at Half Maximum
LEED	Low Energy Electron Diffraction
NEXAFS	Near-edge Extended X-ray Absorption Fine Structure
NSLS	National Synchrotron Light Source (at Brookhaven National Laboratory, USA)
PES	Photoelectron Spectroscopy
PEY	Partial Electron Yield
RGA	Residual Gas Analyzer
TEY	Total Electron Yield
TGM	Toroidal Grating Monochromator
UHV	Ultra High Vacuum
UPS	Ultraviolet Photoelectron Spectroscopy
XANES	X-ray Absorption Near Edge Structure
XAS	X-ray Absorption Spectroscopy
XPS	X-ray Photoelectron Spectroscopy

Chapter 1. Introduction

From our daily experience, we know that chemical reaction rates vary with temperature. About a century ago, the Swedish physical chemist Svante Arrhenius proposed a law of classical chemistry that relates the chemical reaction rate to temperature. According to Arrhenius, the chemical reaction rate is described by an exponential function and at absolute zero the rate of all chemical reactions is zero. Experimental evidence, however, reveals that although in general the Arrhenius equation accurately describes the rate of chemical reactions at most temperatures, the equation fails to predict reaction rates at low temperatures. A few experiments have been done at low temperature to validate this idea and V. I. Goldanskii, *et al.* [1.1] gave a review on the progress in this field recently.

The study of alternative mechanisms for chemical reactions and electron transfer from one atom to another is an interesting physical problem that has important implications for biology, chemistry and physics. The importance of this area of research to the advancement of chemistry was recognized in 1992 by the award of the Nobel

Prize in chemistry to Rudolf Marcus for electron transfer theory. An example of electron transfer is the solvation of alkali metals in ammonia, which is a process whereby electrons are removed from the alkali metal and the ion and electron are dressed by solvent molecules. Recent photoemission studies show that alkali metal atoms can dissolve into solid ammonia even at liquid nitrogen temperature [1.2, 1.3]. In liquid ammonia, Jortner proposed that the solvated electron is localized in a cavity formed in the ammonia media [1.4]. To get to the cavity an electron has to be removed from the metal atom. At or near absolute zero, any solvation that happens must be due to tunneling effects because the Boltzmann factor is small. Electrons have a greater chance to tunnel than atoms do. Based on the above argument, we chose the potassium-ammonia system as a vehicle to study low temperature reactions requiring electron transfer. We monitored the progress of the solvation process using resistivity measurements (bulk) and photoelectron spectroscopy (atomic level).

Chapter two is a review of resistivity measurements for granular films. This is a developing, and yet controversial, area due to the intrinsic complexity of the problem [1.5]. A brief introduction to the most popular theories is given.

A general discussion of the photoemission techniques and experimental setup is given in chapter three. Section 3.1 describes the experimental setup and conditions employed. Sample preparation and granular film growth is discussed in section 3.2. The basic principles of photoelectron and x-ray absorption spectroscopy are given in sections 3.3 and 3.4, respectively.

Chapter four is an introductory chapter for the discussion of the alkali metal-ammonia system in chapter five. The characteristic experimental results for the resistivity measurements of pure metal films or metal films with condensed xenon or krypton are presented in this chapter. A short introduction is given in section 4.1. Section 4.2 describes details about the resistivity measurement. The properties of the granular metal films in our experiments were discussed in detail in section 4.3. The effect of the dielectric media on the resistance of granular films is discussed in section 4.4. To the best of our knowledge, the results in this section are the first direct experimental observation of the effect of dielectric media on granular films resistivity.

Chapter five is the central part of the thesis, which

discusses low temperature charge transfer in the alkali metal-ammonia system. This chapter projects an experimentalist's point of view and attempts to present as clear a picture as possible of the experimental results. This chapter consists of four major sections. An introduction is given in section 5.1. Section 5.2 presents the resistivity measurement results for alkali metal-ammonia system. Section 5.3 discusses photoemission studies of the ammonia-potassium system, which includes four subsections. Subsection 5.3.1 addresses the experimental details of the photoelectron studies. The results for the work function measurements, photoelectron spectroscopy and NEXAFS are given in subsections 5.3.2, 5.3.3 and 5.3.4, respectively. The effort to reveal the quantum nature of low temperature chemical reaction in alkali metal-ammonia system is presented in section 5.4. Although possible models from an experimentalists' point of view are presented and used to explain the experimental results, they are by no means perfect.

The discovery of superconductivity in the alkali-metal fullerides has been followed by attempts to synthesize other types of metallic and superconducting fullerides. The metals studied so far which can form superconducting fullerides can

also dissolve into liquid ammonia. Ytterbium can dissolve into ammonia and had not been studied previously. We did the photoemission study of the Yb-C_{60} system and compared it to the data for the Yb-NH_3 and Yb-Xe systems which had been studied before by this group. The results are presented in chapter six.

Chapter 2. General Background for The Conductivity of Thin Film

2.1. Homogeneous Films

The technique of quench condensation to make metal films, or the thermal evaporation of solid materials onto liquid helium cooled substrates, was pioneered by Shal'nkov [2.1] and subsequently investigated in detail by Buckel and Hilsch [2.2]. It was found that electrically connected films could be fabricated with much lower thicknesses than could be achieved by deposition onto room temperature substrates. Furthermore these films were often times quenched into a metastable amorphous phases as verified by electron diffraction experiments.

Quench condensed metal films grown on Ge substrates were first investigated in detail by Strongin *et al.* [2.3]. In their studies, a variety of materials and substrates were investigated with the resistance versus temperature measured between consecutive *in-situ* depositions. Films grown on Ge , SiO and Al_2O_3 exhibited measurable electrical conductivity at extremely low substrate coverages i.e. less than 10 Å nominal thickness of metal on the substrate. In contrast to this, for

films grown on glass or LiF the onset of electrical conduction usually occurred at thickness greater than 30 Å. It was conjectured that this difference in the onset thickness was due to some subtle chemical interaction at the metal substrate interface which results in superior wetting properties of the metal on Ge [2.4]. It is now known that most transition metals and aluminum spontaneously react with semiconductor substrates to form a thin metal silicide layer. Metal films grown in this way have been called homogeneous films.

2.2. Granular Films

In contrast to films grown on Ge, metal films quenched onto glass or quartz substrates typically have immeasurable electrical conductivity until they are from 30 Å to 50 Å thick [2.3, 2.5]. For this reason the metal films grown on glass have been called granular films, which suggests that they consist of small metal "islands" in a sea of insulating material. The islands are mesoscopic in size, which means that their size is intermediate to the microscopic scale of atoms (~ 5 Å) and the macroscopic scale of solids in the thermodynamic limit (~ 10^8 Å). The prefix meso comes from the

Greek *mesos* meaning middle. At this scale interesting physical phenomena appear whose theoretical description borrows from both macroscopic and microscopic theory. Of interest to us is the charging energy associated with the moving of one electron on and off of a mesoscopic grain. An estimate of this energy can be obtained by using the macroscopic theory of Electrostatics. Abeles *et al.* [2.6] calculated the charging energy, E_c^0, by elementary electrostatic theory using concentric sphere model. In that model the charging energy is given by:

$$E_c^0 = e^2/Kd = e^2/d\varepsilon[1 + (d/2s)] \qquad (2.1)$$

where d is the sphere diameter, ε is the dielectric constant of the external medium, s is the distance between inner and outer sphere, e is the electronic charge and K is defined as effective dielectric constant of the granular metal. From eqn. (2.1) it follows that $K = \varepsilon[1 + (d/2s)]$. For d = 200 Å and K = 10, this gives $(E_c^0/k_B) \sim 100$ K. Energies of this order of magnitude will have a profound effect on the low temperature transport properties of a mesoscopic granular metal film.

Early work on granular films consisted of numerous studies of transport carried out on granular films which were

not ultra-thin and were fabricated at room temperature by evaporation of metals in an oxygen background pressure (see review by Abeles *et al.* [2.6]), or by co-evaporation Al and Ge [2.7]. The granular structure was observed by Scanning Electron Microscopy (SEM) and Transmission Electron Microcopy (TEM). These films were found to be comprised of small (~ 50 Å to ~ 500 Å) metal grains separated in a non-metallic matrix [2.6]. The resistance as a function of temperature was found to fit the relation [2.8]

$$R = R_0 \exp[(E_c/k_B T)^{1/2}] \qquad (2.2)$$

where E_c is the energy associated with the creation of a pair of neighboring grains of charge +e and -e respectively. Several other experiments [2.9 - 2.11] have found R(T) as given in equation (2.2), and this temperature dependence is generally accepted as the best form to fit R(T) data on granular films.

2.3. Hopping Conductivity

In disordered systems, be they granular or homogeneous, the electrical transport in the low conductivity regime, can be modeled by a hopping mechanism. The simplest form of hopping is fixed range hopping, where transitions from

localized site to localized site occur with the adsorption or emission of a phonon [2.12]. This phonon assisted hopping will lead to an activated temperature dependence of the conductivity of the form

$$\sigma = \sigma_0 \exp(-T_1/T) \qquad (2.3)$$

A more sophisticated model takes into account the possibility of tunneling to other localized states, as well as activation over the energy barrier. The result of this approach is the variable range hopping model [2.13].

In the variable range hopping model there is a competition between hopping to a state further away in space which has a smaller energy barrier and requires less thermal energy for activation, and tunneling through a larger energy barrier to a state which is closer in space. To see the physical origin of this variable range hopping, we can make the simplest assumption that the wave function of the electron localized at site i, falls off exponentially as $\Psi(r) = \Psi_0 \exp(-|r-R_i|/\lambda)$, in which case the intrinsic transition rate, w_{ij} between two sites i and j, separated by a distance $R = |R_i - R_j|$, is proportional to $\exp(-2R/\lambda)$. Another contribution to w_{ij} comes from the probability of adsorbing or releasing a phonon. The probability associated with this

process is proportional to the Boltzmann factor, $\exp(-w/k_BT)$. Combining these two contribution we arrive at the total transition probability:

$$w_{ij} = w_0 \exp(-2R/\lambda - |w|/k_BT) \qquad (2.4)$$

At sufficiently high temperatures, the second exponential in (2.4) is small compared with first one, so that the spread of the hopping probabilities and , accordingly, the current are governed by the random spatial distribution of the sites. This is the situation of so-called "R-hopping", where the dc (direct current) conductivity is determined by nearest-neighbour hops and exhibits an activated form.

At low temperatures the hopping transport will eventually move to within a few k_BT of the Fermi level. Under these conditions one will observe the so-called variable-range hopping, a mechanism first suggested by Mott [2.14, 2.15] to cover the situation where the energy between non-nearest neighbor hopping sites is a function of their spatial separation. According to Mott, the dc conductivity is governed by hops for which the exponent in (2.4) becomes an extremum. That is to say the electron will hop so as to maximize the distance R and minimize the energy w. The energy w can be related to the distance R through the density of states, n_0, which we take to be constant and independent of

energy. The total number of states per unit energy in the sphere of radius R′ surrounding a localized site is $(4/3)\pi n_0 R'^3$, or alternatively, the energy per state is

$$w' = 3/4\pi n_0 R'^3 \tag{2.5}$$

We can think of w′ as the energy required to find another state at distance R′. Using this relation, w(R), in the exponent of (2.4) and optimizing the hopping probability, we have

$$R_c = (9\lambda/8\pi n_0 k_B T)^{1/4} \tag{2.6}$$

Substituting for R in (2.4), we obtain the famous Mott "$T^{-1/4}$ law"

$$\sigma = \sigma_0 \exp[-(T_0/T)^{1/4}] \tag{2.7}$$

where σ_0 is a constant and $T_0 = 512/9n_0\pi\lambda^3$.

Equation (2.7) is Mott's variable range hopping law for three dimensions. A more correct and thorough derivation of (2.7) is given by Ambegaokar *et al.* [2.16]. For two dimensional systems, the formula is

$$\sigma = \sigma_0 \exp[-(T_1/T)^{1/3}] \tag{2.8}$$

$T_1 = 9(3)^{-1/3}(n_0\pi\lambda^2 k_B)^{-1}$ where n_0 is now the two-dimensional density of states. The main assumptions which may limit the applicability of the model is the assumption of a transition probability of the form of (2.4) and the assumption that the

density of states is constant and independent of energy. Questioning the later assumption leads us to considerations of the Coulomb gap as discussed in the next section.

2.4. Charging Energy

Electrical conduction in the dielectric regime of granular metal results from transport of electrons and holes by tunnelling from one isolated metallic grain to the next. In order to generate a charge carrier, an electron has to be removed from one neutral metal grain and placed on another neutral metal grain, thereby creating a pair of positively and negatively charged grains [2.17, 2.18]. Due to the fact that every metal grain has a small capacitance, such a process of carrier generation requires a non-negligible charging energy $E_C \sim e^2/C$, where e is the electronic charge and C the capacitance of a grain. In a granular metal, the charging energy has the form

$$E_C = (e^2/d)\ F(s/d) \qquad (2.9)$$

where d is the size of the grain, s is the separation between grains, and F is a function whose form depends on shape and arrangement of the grains and on the interaction between the pair of charges. Abeles et al. [2.6] showed that for a three

dimensional granular system, under certain assumptions, the function F(s/d) is equal to $\{\varepsilon[1+(d/4s)]\}^{-1}$, where ε is the dielectric constant of the intergrain material. For a two dimensional granular film, as is the case for ultra-thin films, an approximate form for the function F(s/d) is a non-trivial calculation, however we shall assume that the form of E_C will be as in (2.9).

The early work of Neugebauer and Webb [2.17] pointed to the importance of charging energy in granular materials. They originally discussed this in the context of an activated model for conduction in a granular system where grain size is very uniform so that the system can be modeled as a homogeneous and uniform array of grains. There are two essential features: firstly, charge transfer between islands is by tunneling; secondly, activation arises from the need to supply non-negligible electrostatic energy to place a single electronic charge on an island. If the charging energy E_C is large compared with k_BT, the concentration of "carriers" - charged grains - will be proportional to a Boltzmann factor so that, applying the model at its most naive level, the conductivity σ should be of the form

$$\sigma \propto \exp[-(2\alpha s + E_C/k_BT)] \qquad (2.10)$$

where α is the tunneling exponent for wavefunctions in

insulating regions between grains and s is the separation between grains.

In real system, s and E_C are distributed quantities because the random nature of the structures. Sheng *et al.* [2.8] conjecture that the films grow in such a way that s/d = constant, which by equation (2.9) leads to the relation sE_C = constant. The charging energy of a spherical island is assumed to be

$$E_C = (e^2/4\pi\varepsilon)[r^{-1} - (r+s)^{-1}] \qquad (2.11)$$

where r is the radius of the island. Putting E_C in terms of s in the exponent of equation (2.10) and finding the extremum of the exponent of equation (2.10) will lead to the characteristic s and E_C which the electron will experience on it's path of maximum conductance. The result is that

$$\sigma = \sigma_0 \exp[-(T_2/T)^{1/2}] \qquad (2.12)$$

where $T_2 = 4\alpha s E_C/k_B$. Equation (2.12) should be valid for both three dimensional and two dimensional films as long as equation (2.9) holds, and the film grows in such a way that s/d = constant. The later constraint may seem somewhat artificial, but there are some reasons to believe that some growth process will result in such a constraint being satisfied [2.6]. The fact that a conductivity of the form of

$T^{-1/2}$ is observed in most granular systems may also be explained by an analysis of charging energy effects in a continuous system.

Considering electron-electron interaction, a microscopic treatment of the effects of Coulomb interactions in continuous disordered systems was carried out by Efros and Shklovskii [2.19]. Their argument may be summarized as follows. Consider the ground state of a disordered system of localized electrons. States below the Fermi energy will be occupied, those above empty. Let E_i be the site energies including Coulomb terms with all other charges. Consider a filled state of energy E_i and an empty state E_j (These will be the energies associated with removing the electron from state i or with placing one on state j, all other charges remaining unchanged.). Now consider the transition of the electron from i to j. The net energy change will be

$$w = E_i + E_j - e^2/4\pi\varepsilon_0\varepsilon_r r_{ij} \qquad (2.13)$$

where $\varepsilon_0\varepsilon_r$ is the permittivity of the medium and r_{ij} the separation of the sites. The last term is the Coulomb potential between the negative charge added at j site and the positive (effective) charge added at i. But for stability of the ground state we require $w \geq 0$. This limits the density of states at low energies. Efros and Shklovskii argue that the

charges will adjust their configuration to form a ground state such that $w = 0$ at all r_{ij}. This condition results in the three and two dimensional densities of states

$$3D \quad g(E) = (3^8\pi^2\varepsilon_0{}^3\varepsilon_r{}^3/2^5e^6)E^2 \tag{2.14}$$

$$2D \quad g(E) = (2^{11}\pi\varepsilon_0{}^2\varepsilon_r{}^2/3^4e^4)E \tag{2.15}$$

In neither case can the density of states continue to increase and it is assumed to level off when g(E) rises to g_0, the density of states neglecting Coulomb interactions. Using equations (2.14) or (2.15) and by analogy with the Mott variable range hopping derivation, the conductivity is found to have the similar form of (2.12) in both two dimensions and three dimensions. The only difference is that in Efros-Shklovskii's formula the T_2 is given by (2.16)

$$T_2 = e^2/\varepsilon rk \tag{2.16}$$

where "r" denotes the localization radius of states near the Fermi level, "e" the electronic charge, "k" the Boltzmann constant, and "ε" the dielectric constant of the media.

Chapter 3. Experimental Techniques

3.1. Introduction

In order to understand the behavior of solid ammonia-alkali metal system, various surface and bulk sensitive techniques were used to study the electronic structure, chemical properties and transport properties of this system. The experiment was carried out in two stages. First, the transport properties and chemical properties of the solid ammonia-alkali metal system were studied by resistivity measurements. Second, the electronic and chemical properties of the solid ammonia-alkali metal system were studied by photoemission at the National Synchrotron Light Source (NSLS) U7A beam line. In the following sections I will describe briefly the physical principles of these measurements and experimental details.

The experiment described in this work took place in an apparatus that evolved over time. The bulk of the work was performed with an ultra-high vacuum (UHV) system consisting of a 14 inch stainless steel bell jar atop a base chamber maintained at UHV by a 400 liter per second Vacion pump. The pump could be isolated by a poppet valve. A titanium

sublimator provided additional pumping at low pressures. A Bayard-Alpert ionization gauge with tungsten filaments, operated at 4 mA emission, was mounted in a port of the base chamber for measuring the chamber pressure. Figure 3.1 shows the system layout in a middle stage of the work.

Photoemission excitation in the vacuum ultraviolet was provided by a differentially-pumped cold cathode discharge lamp based on a design by Shevchik [3.1]. An oil-sealed zeolite-trapped rotary pump was used both as second stage and as forepump for the liquid nitrogen trapped diffusion pump, the first stage of the lamp pump. Discharge gas (typically helium, of 99.99% purity) was leaked into the discharge region of the lamp such that the first stage pressure was 50 millitorr. An eight-inch quartz capillary of one millimeter bore limited gas flow to the chamber while transmitting ultraviolet light by internal reflection. The base post-bakeout ambient chamber pressure of 1×10^{-10} Torr rose to typically 5×10^{-9} Torr during lamp operation, but all the partial pressure rise can be accounted for by the helium gas.

Detailed photoemission studies were carried out at the U7A beam line at the National Synchrotron Light Source (NSLS) at Brookhaven National Laboratory. The U7A toroidal grating

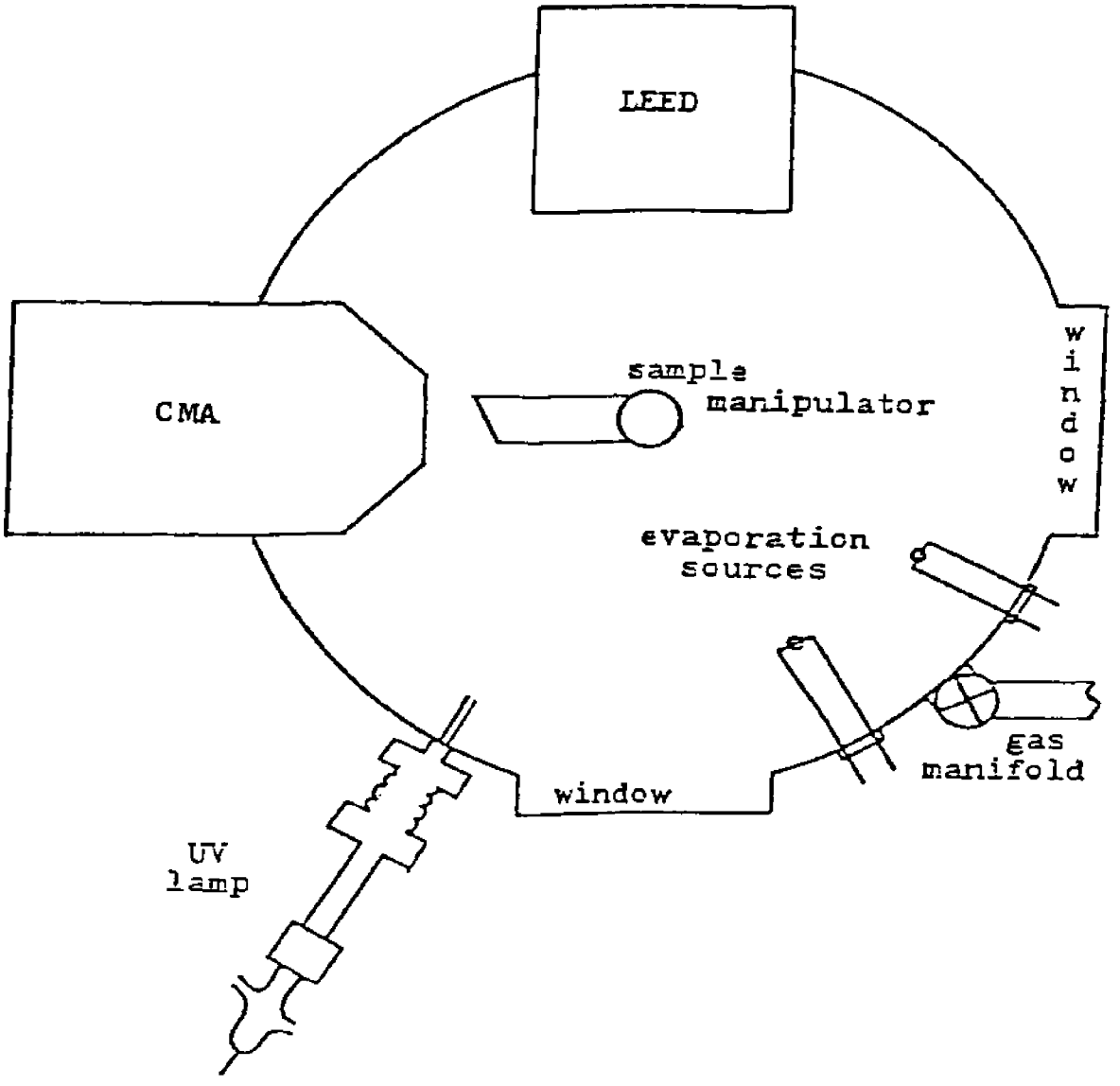

Figure 3.1. Plan view of experimental chamber set up.

monochromator (TGM) beam line had a continuous energy range of 120 - 400 eV using 400 1/mm grating, and 300 - 1000 eV using the 1000 1/mm grating. The resolving power of U7A was about 750, with a beam flux of 10^{11} photons/(sec. Amp.). The experimental apparatus included a vacuum chamber with a post-bakeout ambient chamber pressure of 1 x 10^{-10} Torr, and facilities for cooling a copper substrate to below 6 K. To maximize cooling to the sample, the sample holder, which was a single block of copper rod, extended into the inner liquid helium dewar and was sealed by a conflat-type flange.

The ammonia gas (of 99.998% purity) was introduced into the chamber through a doser which was connected to a gas manifold. A residual gas analyzer was used to determine the constituents of the background pressure which is typically in the low 10^{-10} Torr range, and can act as a sensitive leak detector for helium contamination from the cryostat. Hydrogen and carbon monoxide are the dominate background species each with partial pressures usually less than 1 x 10^{-10} Torr. In the photoelectron spectroscopy (PES) measurements, photoelectrons were detected by a Vacuum Science Workshop (VSW) HA-100 hemispherical electron energy analyzer.

3.2. Sample preparation

For the resistivity measurements, the standard four-terminal method was used. Four silver strips were evaporated onto a masked and pre-cleaned glass slide. The glass slide was pretreated in acid, rinsed out in water, dried out, then treated in acetone and ethanol before use. The deposited silver strips were 10 mm long, 1 mm wide and about 800 Å thick. The distance between any two adjacent strips was 2 mm. Electrical measurement leads were indium-soldered onto these silver strips, then the glass substrate was glued onto the copper block of a liquid helium cryostat by Stycast 2850FT epoxy.

The continuous flow cryostat was specially designed so that cryogen is delivered directly to the copper cold head by inserting a long transfer tube into the cryostat. The flow of cryogen was regulated either with a needle valve located at the end of transfer line or by two valves at the exhaust gas outlet. The cryostat was mounted onto a differentially pumped rotary feedthrough and the whole assembly was seated on a manipulator so that full 360 degree rotation as well as X, Y and Z motion is possible. The sample could be cooled down to 6 - 7 K within 45 minutes with a reasonable helium flow rate.

The temperature of the sample is a very important variable in the experiments. A silicon diode cryogenic temperature sensor (Omega Technologies Company Model CY7-SD) was glued onto the top of the glass slide to measure the temperature of the sample.

The thin films were prepared by thermal evaporation. The following sequential basic steps take place: (1) A vapor is generated by boiling or subliming a source material; (2) the vapor is transported from the source to the substrate; and (3) the vapor is condensed to a solid film on the substrate surface. The gold films were prepared by direct heating a tungsten basket which held a piece of gold. Alkali metal films were prepared by heating alkali metal getter sources (SEAS Getters/USA Inc.). All the evaporation sources were thoroughly degassed under ultrahigh vacuum (UHV) before use. After that, the evaporation pressure in the vacuum chamber was normally below 5×10^{-10} Torr. Such low pressures are necessary in order to grow clean films. The vapor pressure for a reasonable evaporation rate of 1 ML/min is on the order of 10^{-8} Torr.

At the early stages of film growth, the adsorbate metal atoms may form three-dimensional metal clusters instead of

laying flat on the substrate, making it difficult to accurately measure the thickness of very thin films. Rough estimates of film thickness can be obtained by using a quartz-crystal thickness monitor, photoemission measurements, or Auger electron spectroscopy (AES). The thickness of the gold film in our experiments was about 100 Å measured by a quartz-crystal thickness monitor inside the chamber. We could not use the quartz-crystal thickness monitor to estimate the thickness of alkali metal films, because at room temperatures only a very small amount of alkali metal sticks on quartz substrates and such rate monitors are inaccurate in measuring thicknesses below a few angstroms. In our experiments, the alkali metal evaporation rate was calibrated using photoemission, after which all evaporations were done at the same conditions (e.g. using same power, opening the shutter after warming the getter sources for 20 seconds, etc.). The estimated thickness of alkali metal film was between 100 - 200 Å. For nonreactive thin films without inter-diffusion at the interface, either the attenuation of characteristic substrate peaks or the intensity of the overlayer peaks in the photoelectron spectra can be used to estimate the adsorbate thickness. Considering that material A with electron mean free path λ_A forms a thin overlayer of

thickness d_A on the substrate B, the photoelectron intensity from substrate B is given by

$$I_B = I_B^0 \exp[-d_A/\lambda_A(E_B)\cos\theta] \qquad (3.1)$$

and that from the overlayer A by

$$I_A = I_A^0\{1 - \exp(-d_A/\lambda_A(E_A)\cos\theta)\} \qquad (3.2)$$

where I_B^0 is the photoemission intensity from the clean substrate B, I_A^0 is that of a very thick overlayer material A, and θ is the photoelectron emission angle. The determined d_A value usually is within the factor of two or three of the correct value assuming two-dimensional film growth. The major factor limiting the accuracy of the measurement is the uncertainty in the electron mean free path λ_A.

In gas adsorbate studies, gases were admitted to the vacuum system through bakeable dosing valves which allow controlled inlet rates into UHV directly from atmospheric pressure. The gas exposure is expressed frequently in Langmuirs (1 Langmuir = 10^{-6} (torr)(sec) = 1.33 x 10^{-6} (mbar)(sec)). It should be pointed out that the exposure is not the adsorbate thickness because of the non-unit sticking coefficient. Assuming a monolayer capacity of 6 x 10^{14} molecules/cm^2, 1 L exposure of ammonia corresponds to 4.65 monolayer at 10 K if the sticking coefficient is one. Since the gas exposure in Langmuir is measured by recording the

pressure and time, one should also consider the ion gauge correction for different gases and pressure difference between sample and ion gauge caused by expansion of the gas from the gas doser.

3.3. Photoelectron Spectroscopy (PES)

It has been known for many years that energetic photons can knock off electrons from a sample. Photoemission usually can be treated in the one-electron picture: The emitted electron comes from a one-electron orbital within the sample without suffering losses in the escape process, the spatial distributions and energies of the other electrons left are the same as in the initial state before emission of the electron (Koopmans' approximation, [3.2]). In this case the energy of the emitted electron equals the photon energy ($h\upsilon$) minus the binding energy (E_B) of the corresponding bound electronic state: an analysis of the energy distribution of the photoexcited electrons yields information about the energies of occupied one-electron states.

$$K.E. = h\upsilon - \phi - E_B \qquad (3.3)$$

where ϕ is the work function of the sample. The binding

energy of a core electron is a sensitive function of atomic identity.

On their way to the sample surface, primary photoelectrons may suffer various kinds of scattering depending on their kinetic energies. Quasielastic scattering by phonons may alter the direction of the outgoing electron and reduce the electron energy by a few meV. The electron may also lose a substantial amount of energy through the creation of electron-hole pairs or the production of collective many-body excitations of the electron gas known as plasmons. At low energies, single particle excitations account for most electron energy losses. Above the plasmon energy (typically 10 - 15 eV, depending on materials), the energy losses are dominated by plasmon creation which becomes weaker as the electron energy increases. Because the electron density in the valence band is nearly a constant for most materials - about 0.25 electrons/$Å^3$ [3.3], the mechanism of valence band electron excitation means the existence of a universal electron energy loss curve for most materials within a certain energy range. This "universal curve" which has been demonstrated both experimentally [3.4, 3.5] and theoretically [3.6] is shown in Figure 3.2. The electrons with kinetic

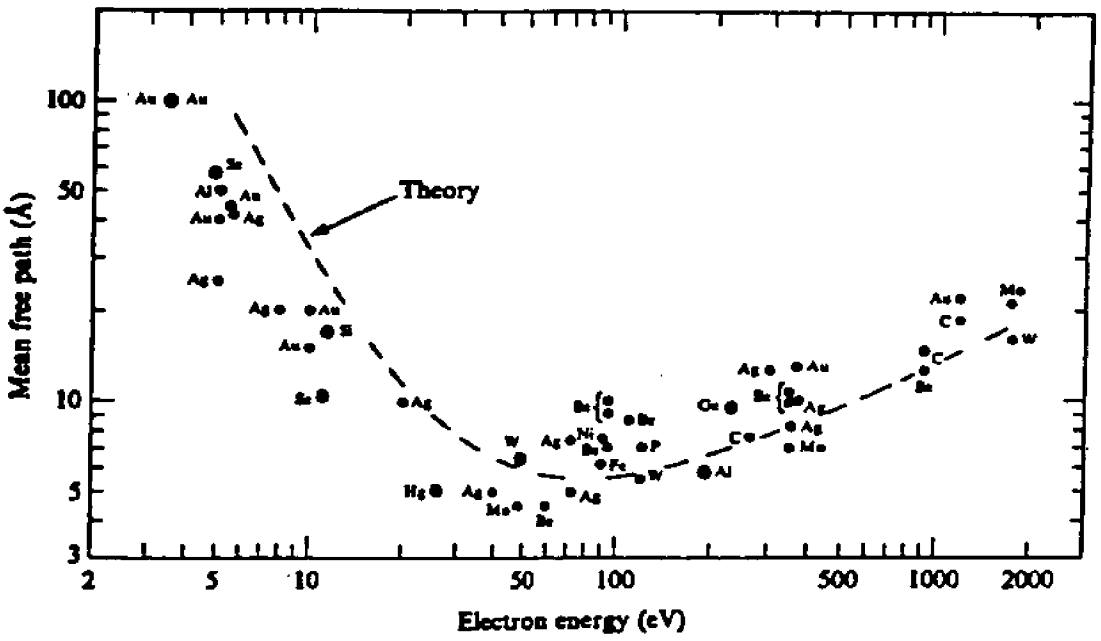

Figure 3.2. Energy dependence of electron mean free path: experiments [3.4, 3.5];theory [3.6].

energies in the range 15 - 1000 eV have a very short mean free path in matter (< 10 Å) and those which can emerge without substantial loss of their kinetic energy must originate very close to the surface. The intrinsic surface sensitivity of these electrons and the tunability by varying energy and angle make the measurements of the kinetic energy of electrons ejected from a solid after photon or electron bombardment very useful tools in surface science.

A "three-step model" of photoemission developed by Berglund and Spicer [3.7] is widely used in interpreting experimental data. In this model, photoemission is treated as a sequence of (1) optical excitation of an electron, (2) transport of the excited electron through the solid to the sample surface, and (3) the escape of the electron into the vacuum. The energy distribution curve (EDC) of photoemitted electrons $I(E, \omega)$ is the sum of a distribution of primary electrons $I_p(E, \omega)$ that have not suffered any inelastic scattering and a background of secondary electrons $I_s(E, \omega)$ that have suffered an energy loss due to the mechanism mentioned before.

$$I(E, \omega) = I_p(E, \omega) + I_s(E, \omega) \qquad (3.4)$$

The photoemission intensity of primary electrons can be factorized into a distribution function of photoexcited

electrons $P(E, \omega)$, a transmission function $T(E)$, and an escape function $D(E)$

$$I_p(E, \omega) = P(E, \omega) \times T(E) \times D(E) \qquad (3.5)$$

Assuming that the inelastic scattering probability can be characterized by an isotropic electron mean free path $\lambda_e(E)$ that only depends on the energy E, then $T(E)$ is given by

$$T(E) = \lambda_e(E) / (\lambda_e(E) + \lambda_{ph}(\omega)) \qquad (3.6)$$

where $\lambda_{ph}(\omega)$ is the attenuation length of the photon in the solid. The escape from the solid is possible only for those electrons with a kinetic energy component normal to the surface that is sufficient to surmount the potential barrier $E_F + \phi$. This defines an escape cone with an opening angle θ_c relative to the surface normal [3.8], $\cos\theta_c = [(\phi + E_F)/E]^{1/2}$. For an isotropic distribution of electrons inside the solid, the escape function $D(E)$ is then given by

$$D(E) = 0.5 \{1 - [(E_f + \phi)/E]^{1/2}\} \quad E > E_F + \phi \qquad (3.7)$$

$$= 0 \quad E < E_F + \phi$$

Both $T(E)$ and $D(E)$ are smooth functions of E beyond the low energy cutoff. Although they may distort the energy distribution of photoexcited electrons, they are not expected in themselves to give rise to structure in $I_p(E, \omega)$. $P(E)$ is given by the golden-rule expression of the transition

probability between an initial state ψ_i with a binding energy E_i inside the solid and a final state ψ_f with an energy E

$$P(E, \omega) \propto [< \psi_f \mid \mathbf{P}\cdot\mathbf{A} \mid \psi_i >]^2 \, \delta(E - E_i - h\upsilon) \qquad (3.8)$$

$P(E, \omega)$ strongly depends on the density of each of the two states involved, the coupling between the two states and the incident photon energy. If the coupling varies slowly with energy and the final state density is fairly flat, then the photoelectron energy spectrum reflects the energy distribution of occupied electronic states of the sample surface.

The above single-electron interpretation ignores the fact that after excitation of the photoelectron the remaining electrons can relax towards the hole created in order to screen the suddenly appearing positive charge. As a result of this screening is the lowering of the measured binding energy. This binding energy shift is commonly referred to as the relaxation energy E_r [3.9]. In an isolated atom, the relaxation energy can not be measured since it is simply a theoretical concept which makes use of the one-electron approximation for an n-electron system. The relaxation energy in molecules is nearly always larger than in atoms, because in molecules more charge can flow towards the positively charged hole. It is convenient to split the relaxation energy

into two parts [3.10]: the 'atomic' part discussed above usually called intra-atomic relaxation, and the 'extra-atomic' part which arises from the relaxation of the rest of the system. Extra-atomic relaxations are observed in solid and are particularly severe in metals where the delocalized valence charge can easily polarize and screen the core hole.

The reorganization of the electronic structure after creation of a core hole may also lead to the formation of excited states. If an electron is excited to higher-lying bound states, the corresponding satellite lines in the spectrum are called "shake-up" satellites. If excitation occurs into free continuum states, leaving a doubly ionized atom with holes in the core as well as valence shell, this is called a "shake-off" process. In solids the latter effects usually do not show up in the form of discrete peaks, because they tend to fall into the energy region of inelastic secondary electrons and often show no resolvable structure. In metals, the higher density of unfilled states above the Fermi level causes the appearance of low kinetic energy tails of the photoelectron peaks due to such multi-electron events, that is, the peaks become asymmetric.

In addition to these relaxation shifts, the binding energies associated with a given element also depend on its

chemical environment. The basic physics underlying the change in binding energy is straightforward. The energy of an electron in a tightly bound core state is determined by the attractive potential of the nuclei and the repulsive core Coulomb interaction with all other electrons. A change in the chemical environment of a particular atom involves a spatial rearrangement of the valence charges of this particular atom and a different potential created by the nuclear and electronic charges on all the other atoms in the compound. In practice, the chemical shift can be used to identify the chemical environment of an element by comparison with the binding energies of a set of reference compounds involving the same element. For example, the 2p core level of Al has a binding energy of 72.6 eV in Al metal and an energy of 75.3 eV in Al_2O_3 [3.11]. This shift of 2.7 eV is typical for the chemical shifts encountered when the oxidation state of an atom is changed by several formal elementary charges. An extensive list of chemical shifts for various states of oxidation of many elements has been compiled by Holm and Storp [3.12]. This fingerprinting technique is of considerable value in a variety of applications ranging from catalysis to environmental studies.

3.4 X-ray Absorption Spectroscopy (XAS)

Ionization of a core level in an atom by absorption of a photon with high enough energy creates a photoelectron which propagates as a spherical wave. Its wavelength is determined by the difference between the photon energy $h\upsilon$ and the ionization energy E_i. Scattering of this wave at the neighboring atoms causes interference effects which depend on the local geometry and the wavelength. As a consequence, the absorption coefficient for the exciting radiation is modulated with varying photon energy instead of a smooth decreasing $(1/E^3)$ predicted by the atomic theory as the incident photon energy is above the absorption edge. The observed structures near the absorption threshold was first explained in general terms by a theory of Kossel [3.13], and for many years was referred to as "Kossel structure". It is now called near edge x-ray absorption fine structure (NEXAFS), or x-ray absorption near edge structure (XANES). The term XANES is more commonly used for solids and inorganic complexes while NEXAFS is used more in conjunction with surfaces. The features extending from 50 to hundreds of electron volts past the edge was called "Kronig structure" after the scientist who provided its theoretical explanation

[3.14]. Sayers et al. [3.15] predicted that structural information can be obtained relatively easily from analysis of the Kronig structure, which is now called extended x-ray absorption fine structure (EXAFS).

In EXAFS the excited atom acts as source as well as detector. When the outgoing photoelectron encounters a neighboring atom, only a relatively small fraction will be backscattered, and sideway scattering is even less probable. In order for an electron of the latter type to return to the source it has to undergo at least another process of this type. Since the total path will then be considerably longer than that for directly backscattered electron, multiple scattering contributions will be very weak. Since multiple scattering is not important in EXAFS [3.16], a simple single scattering model has been formulated [3.17, 3.18]. By comparison of the EXAFS spectra for an unknown compound and a model compound, one can determine the coordination number of the absorber, the bonding length between the absorber and its neighboring atoms and the Debye-Waller factor which accounts for thermal vibrations and static disorder of the central atom. NEXAFS, on the other hand, can select specific atomic species through their K-edge and determine the intra-

molecular bond length of the selected molecule, the precise orientation of the molecule and functional groups on surfaces or in solids (for a review on these subjects, see [3.19]). By comparison of spectra for free and chemisorbed molecules, one can also find out which orbitals are involved in chemisorption.

The NEXAFS region is distinguished from the higher energy EXFAS region by the stronger multiple scattering of excited electrons by the surrounding atoms. The spectrum is also complicated by the onset of shake up (off) transition, which is inaccessible to the simple single scattering EXAFS analysis. Therefore, it is more appropriate to regard the electron as being excited into a localized antibonding state of the system rather than to describe it as an outgoing plane wave as in the case of EXAFS. The K-edge spectra of atoms and molecules contain a variety of pronounced resonance features. These resonances correspond to electronic transitions of a K-shell electron to states near the vacuum level or to continuum states with a large scattering amplitude (Figure 3.3). The features below the ionization potential, called bound state resonances, are due to transitions from the K-shell to valence states or Rydberg states or a linear

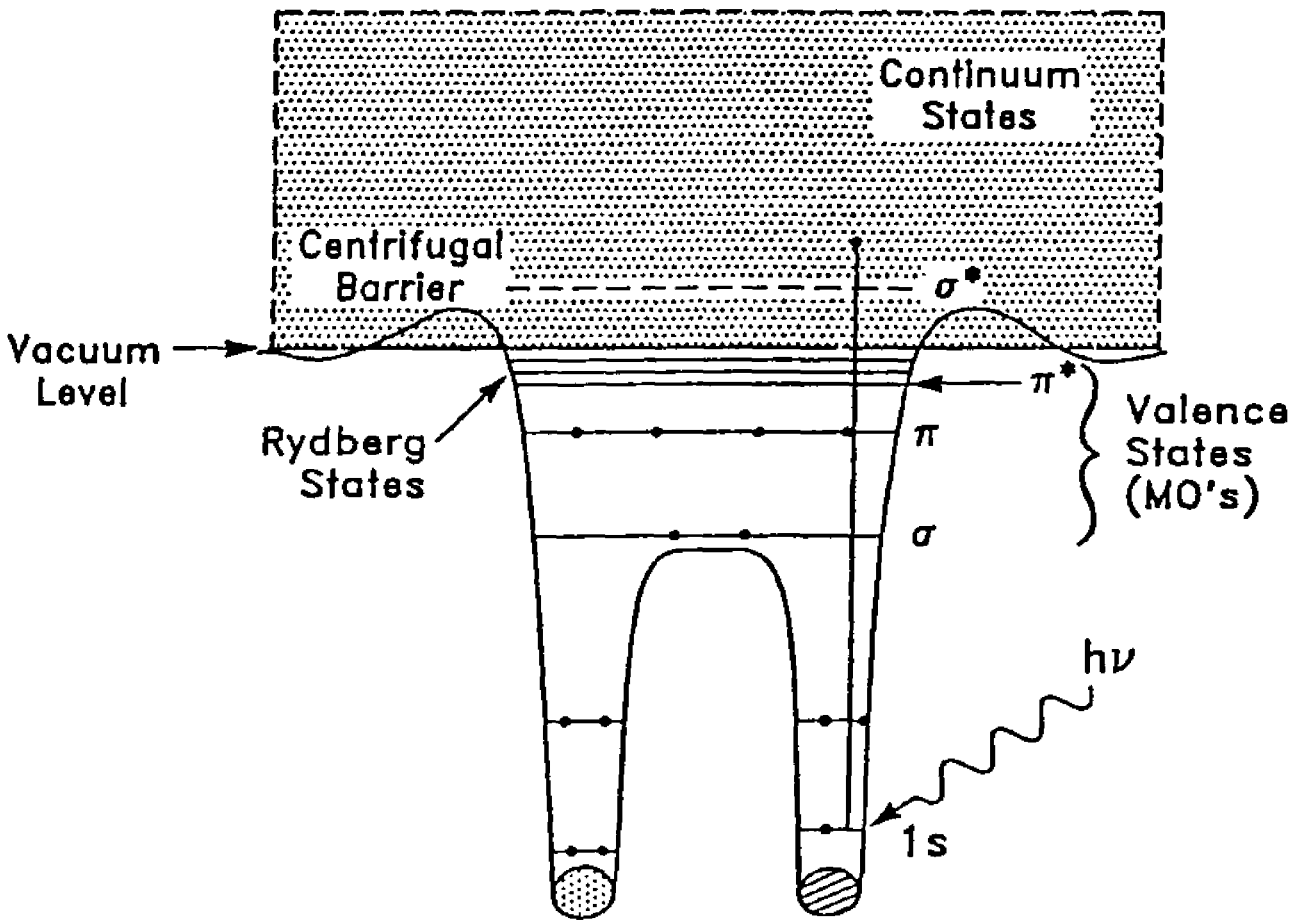

Figure 3.3. Schematic potential of diatomic molecules.

combination of them. The features above the ionization potential called shape, or continuum, resonances are due to transitions to quasi-bound molecular states. In a scattering picture the excited photoelectron can be trapped by the molecular potential in the direction along the internuclear axis. Photoelectron scattering back and forth between the absorbing atom and its neighbor results in shape resonances.

Since the resonance is a result of multiple scattering process along the internuclear axis, its energy position is directly related to the internuclear distance [3.20]. A quantitative correlation between the energy position of the resonance and bond length has been observed [3.21]. For gas phase molecules, there is a simple linear correlation between the σ^* resonance position and the intra-molecular bond length [3.22]. NEXAFS studies of the K-shell absorption spectra of chemisorbed diatomic molecules showed that the resonance energy position relative to that observed in the gas phase can provide valuable information on the intra-molecular bond length and the changes in the electronic structure upon chemisorption [3.23, 3.24].

The x-ray absorption spectrum can be measured by detecting the electron yield. There are three electron yield detection techniques being used today. Figure 3.4 shows a

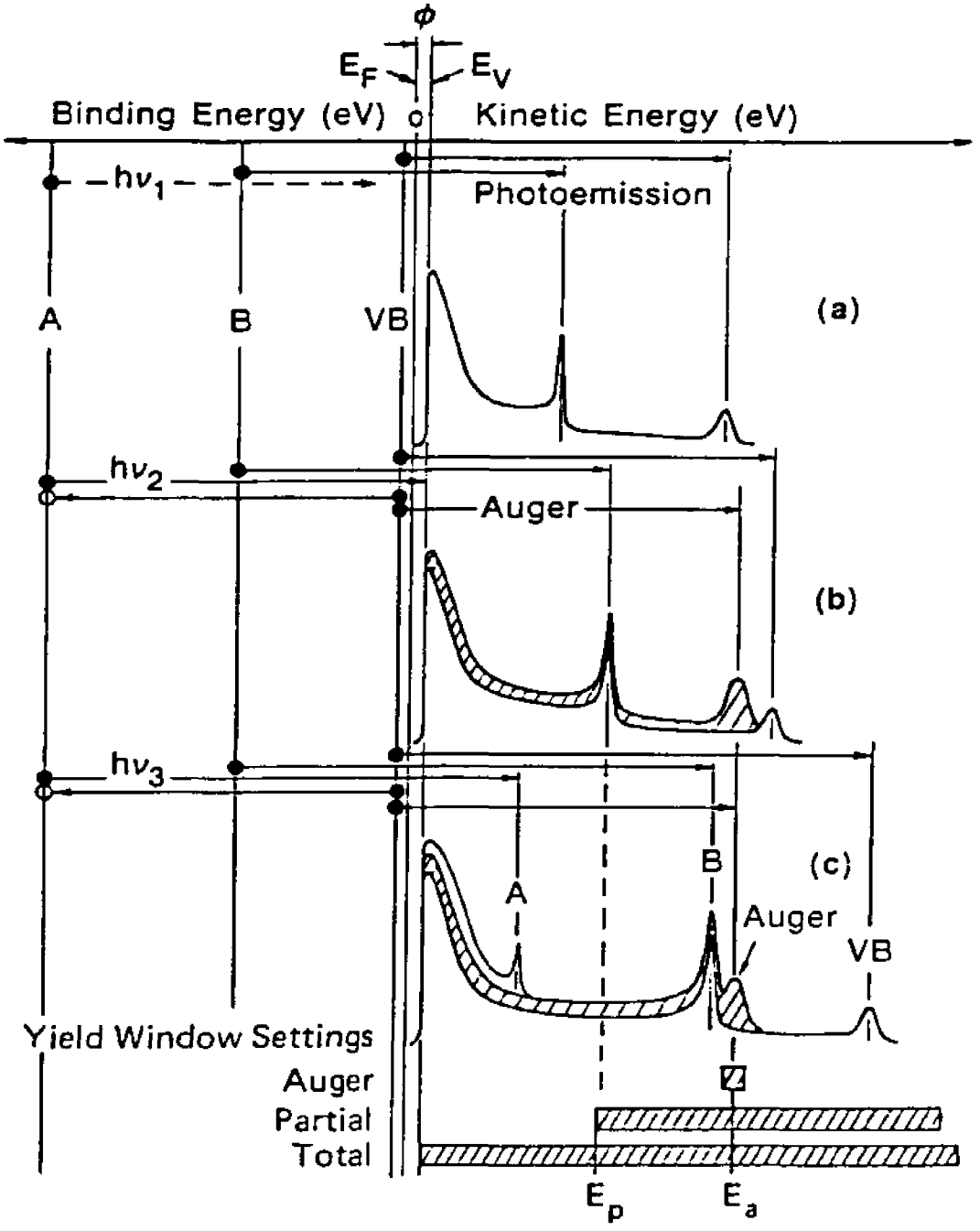

Figure 3.4. Energy level diagram and schematic photoemission spectra at different photon energies for a sample containing atoms with two core level A and B and a valence band VB [3.19].

schematic photoemission spectrum of a dummy sample containing atoms with two core levels labelled A and B, and a valence band. The Fermi level is defined to be zero for both the electron binding energies and the photoelectron kinetic energy and is separated from the vacuum level by the work function ϕ. When the incident photon energy $h\upsilon_1$ is less than $E_b(A)$ only regular photoelectrons can be observed. As the photon energy is increased above the absorption threshold of shell A, a characteristic Auger peak shows up in the photoemission spectrum at a kinetic energy E_a while the photoemission peaks shift with the photon energy. The position of Auger peak is determined by the relative binding energy of the three energy levels which are involved in the Auger process and is independent of incident photon energy. But the intensity of the Auger peak will change with the incident photon energy and follow the x-ray absorption cross section of shell A. When the photon energy is increased even more ($h\upsilon_3$), a photoemission peak corresponding to level A is observed while the Auger peak remains at the same position. By use of an electron energy analyzer, one can select a window and center it at the fixed energy of the Auger peak. This is so-called Auger electron yield (AEY) detection. The

recorded intensity will directly give the x-ray absorption cross section of shell A.

On their way to the sample surface, a fraction of the Auger electrons may suffer inelastic scattering and emerge from the sample with smaller kinetic energy. The energy distribution of the inelastic Auger electrons (shown as a cross-hatched area in Figure 3.4) is independent of photon energy. In the partial electron yield (PEY) measurement, one can select a threshold energy with a retarding grid detector to avoid that new photoemission peaks enter the kinetic energy window of the detector over the NEXAFS energy range. For the same solid detection angle the PEY mode gives a higher count rate than AEY mode, but the signal to background ratio is reduced.

The total electron yield (TEY) detection technique collects electrons of all energies from the sample. The signal is dominated by low energy electrons with kinetic energies below about 20 eV which come from the inelastic scattering of both photoelectrons and Auger electrons. The inelastically scattered Auger electrons are responsible for the desired NEXAFS signal. When the incident photon energy exceeds the K-shell ionization potential, the 1s photoemission peak (peak A in Figure 3.4) starts to

contribute to the TEY. In principle, this could cause a step-like increase in the TEY. But in practice, no such step is observed because the measured elastic 1s photoemission intensity increases gradually at threshold to a maximum about 20 eV about the ionization potential [3.25] and it is small compared to the total Auger electron intensity. Because the elastic Auger electrons have higher kinetic energy than that of the elastic photoelectron, the K-shell TEY signal is always dominated by the inelastic Auger channel [3.26]. For this reason, all of the three electron yield measurements give almost identical NEXAFS spectra, except for having different signal-to-background and signal to noise ratios.

Chapter 4. Physical Properties of Discontinuous Film: an Introduction to Chapter Five

4.1. Introduction

Investigations of the charge transport mechanism of granular films have been an active research field for a long time due to the industrial demand for microminiaturized electronic components. There are a lot of studies on Au [4.1], Ag, Ni [4.2], In, Al [4.3], Cu [4.4], Ga [4.5], Pb [4.6, 4.7], Sn and Bi films, but relatively little work has been done on alkali metal films. Part of the reason is that due to the high chemical reactivity of alkali metals, it is much more difficult to prepare an uncontaminated film and the experimental period is relatively longer. The work here aims to further our understanding of the potassium-ammonia system. In the following sections, I will first discuss the properties of unmodified metal films and point out the reason we use the resistivity measurement to detect small chemical change in alkali metal-ammonia system. After that I will present results for the introduction of non-interacting dielectric media (Xe and Kr) onto these metal films to show the effect of changing the dielectric constant between metal

clusters. This is necessary step in order to distinguish the differences between the physical change and the chemical change in alkali metal-ammonia system discussed in chapter five.

4.2. Experimental details

The resistivity measurements were carried out in an ultrahigh vacuum chamber described in chapter 3. The electric circuit for the resistivity measurement consisted of a 1.5 Volts battery, two 10 MΩ resistors and the sample. A Keithley 485 picoammeter was placed in series with the circuit. When the sample resistance was larger than 100 MΩ, only a two probe small current measurement was used because the input impedance of Keithley 181 nanovoltmeter is 1 GΩ. When the sample resistance became smaller than 100 MΩ, it was switched to a four probe measurement with the two inner probes connected to the Keithley 181 nanovoltmeter. The vacuum system achieves a base pressure of 7×10^{-11} Torr at 7 K and reached the mid 10^{-10} range during potassium or gold evaporation. While flow rate of liquid helium was adjusted during evaporations, little or no rise in temperature was

observed. The gold was sublimed from a small chunk in a tungsten wire basket. Potassium was evaporated from a SEAS getter source. Due to the low work functions of alkali metal and alkali metal-ammonia systems [4.8], precautions were taken to keep the chamber in the dark to eliminate photoelectric effects. The only exceptions were during the evaporations of the metals and the introduction of ammonia, krypton and xenon gases. One test run showed that the light from the ion gauge caused a 6% decrease of the film resistance of the sample; in this experiment ammonia were condensed on a potassium film. AC measurements were conducted by using a Wavetek (Model 19) function generator and a lock-in amplifier (Princeton Applied Research, Model 124A). The lock-in amplifier was used as a phase sensitive voltage detector. The lock-in amplifier was not connected across the sample because the relatively large dynamic range was needed during the measurement. Instead, it was connected to a series of sampling resistors. The film resistance was then calculated using elementary circuit theory.

4.3. General Properties of Granular Metal Films

The granular metal films were made by evaporating metals onto glass substrates. The films are assumed to be granular because the metals do not easily bond to the glass surface. Atomic mobility is reduced by condensing vapor atoms onto a substrate cold enough to reduce thermal diffusion considerably and also to absorb the heat of condensation without an appreciable rise in temperature. But there is substantial mobility of the metal atoms on the substrate even at temperatures of 10 K or so. Thus the metal atoms would tend to form small clusters or islands separated by vacuum. The concentration of impurities in the films is very small because the films were grown under ultrahigh vacuum conditions.

As the metal is deposited onto the substrate, the randomly distributed three dimensional nucleation sites are first formed and rapidly approach a saturation density with a small amount of deposit. These nuclei then grow to form bigger islands whose shapes are determined by interfacial energies and deposition conditions. The growth is diffusion-controlled; as islands increase their size by further deposition and come closer to each other, the large ones

appear to grow by coalescence of the smaller ones. Under equilibrium conditions, discrete islands will be formed which conform to a distribution such that the average inter-island distance corresponds to the mean diffusion distance of the random walk process.

Annealing the quench-condensed metal film is a very important step which is necessary in order to get reproducible experimental results. The final geometrical structure of the film is a function of the substrate, the pressure inside the evaporation chamber, the sticking coefficient and the surface mobility. If we choose the same kind of substrate and keep the same evaporation condition and evaporation rate, then, roughly speaking, the grain size of the film only depends on the annealing temperature. After quench-condensing onto the glass slide at about 10 K, the gold films in our experiments usually had film resistances of 250 MΩ. When annealed to 90 K, 200 K and 290 K and cooled down to about 10 K, the film resistance became 1000 MΩ, 1500 MΩ and 7815 MΩ, respectively. The absolute value of the temperature coefficient of resistance (TCR) of the granular film became smaller as the film was annealed to higher temperatures. This is understandable because right after

quench condensation the film consists of lots of small clusters separated from each other by vacuum. The electrical conduction was made possible only due to electrons tunneling to the nearest neighboring cluster across a very small distance, and electrons hopping to a cluster which is further away in space but has a lower activation barrier. (I will discuss the electric transport properties of these granular films later.) As the annealing temperatures increase, more and more small clusters are able to gain enough energy to overcome the surface diffusion barrier and coalesce into bigger islands. As a result of annealing, the average size of metal clusters and distances between the metal clusters increases, as does the film resistance. This conclusion is consistent with the results of Chopra [4.9] by the direct electron microscope observations of a 100 Å thick Au film deposited on a NaCl substrate. The annealing process removed the unstable metal clusters, and the change of film resistance was found irreversible in both gold and potassium samples. After annealing, the film resistance change with temperature was reversible up to the annealing temperature. Figure 4.1 shows the experimental results for a potassium film.

The electrical resistivity of an evaporated film

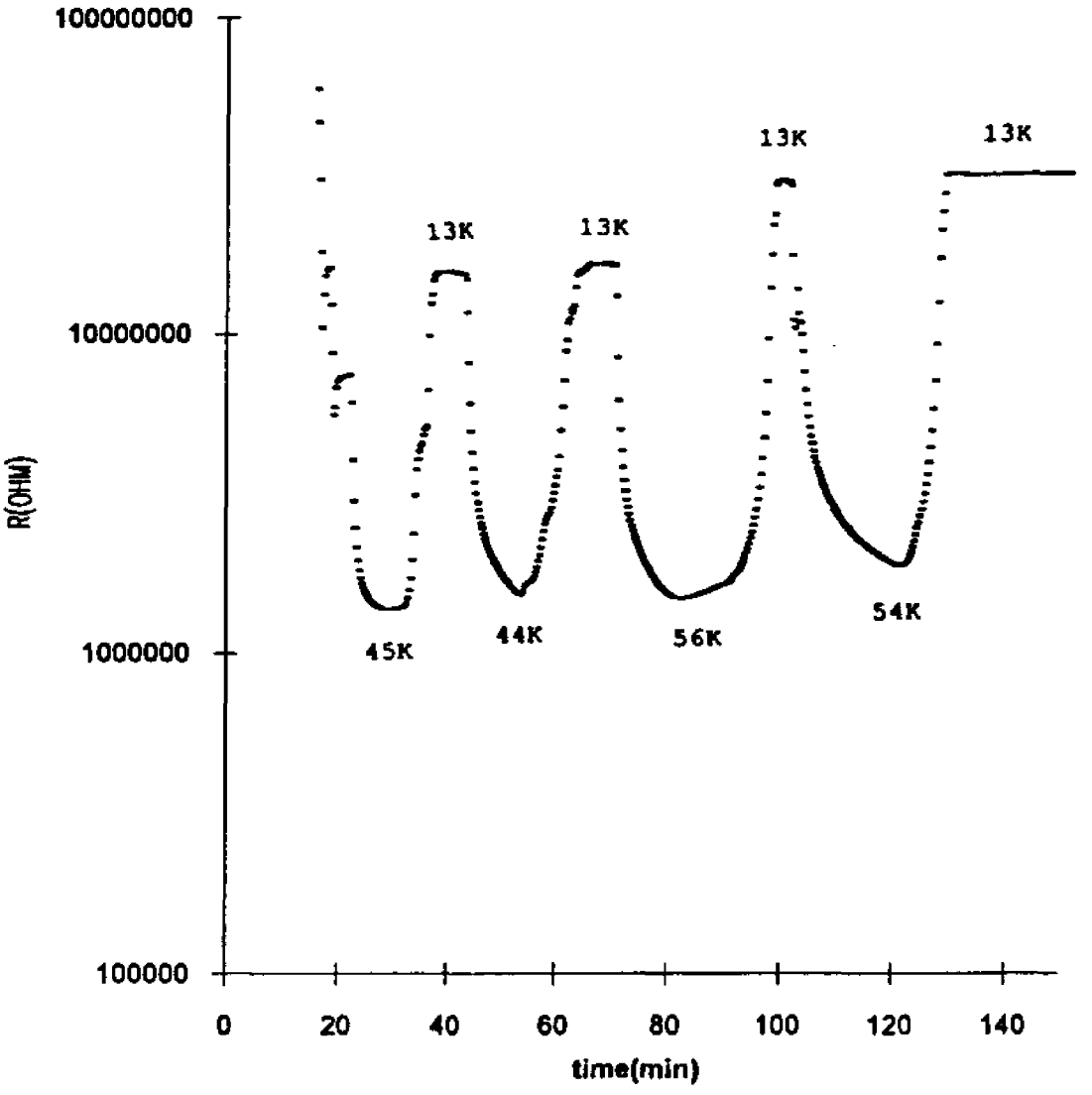

Figure 4.1. The annealing process for a granular potassium film. After annealed to a high temperature (e.g. 45 K), then up to that temperature the annealing process was reversible. Two different annealing cycles are shown in the figure, one annealed to 45 K first, the other to 56 K.

depends on how much metal has been deposited at a given temperature. The electrical resistivity of thick films (those films for which the thickness is much larger than the mean free path of the conduction electrons) is generally much higher than the bulk value. This excessive resistivity may be ascribed to the scattering of electrons by structural defects and impurities. Although impurities have a profound effect on the film resistivity, their role in ultrahigh vacuum prepared films of pure materials can be negligible. But many structural defects such as dislocations or vacancies are frozen during deposition of a film. The electrical resistivity of thin granular films is even higher than the thick films because the thin granular films consist of small clusters and the electric conduction between clusters is possibly only through electron tunneling and hopping. Due to the difference in the conduction mechanism, thick metal films are much less sensitive to the change of temperature and dielectric medium than thin granular films. In our experiments, we used the change of film resistance as a sensor to indicate small structural changes caused by chemical reactions between potassium clusters and ammonia. Since only thin granular films can serve this purpose, we will concentrate on thin granular films in the following

discussion and only use the word "film" instead of "granular film". It is worthwhile to point out that this method was sensitive enough to see the resistivity change of a potassium film caused by an estimated oxygen exposure of 0.002 L. This is the reason we use the change of film resistivity to measure small chemical reactions at low temperatures.

Figure 4.2 shows the change of potassium film resistance with temperature after first annealing the evaporated potassium film to 56 K. Figure 4.3 is the change of gold film resistance with temperature after first annealing the evaporated gold film to 91 K. The logarithm of film resistance fits best to the $T^{-1/2}$ term, which is given in formula (2.12), in both cases. The other possible fittings for the gold film, using the thermal activated conduction model and Mott's variable range hopping model, are shown in figures 4.4a and 4.4b, respectively. Computer curve fitting for lnR versus T^{-X} gave $x = 0.5$ and 0.6 for the potassium and gold films, respectively. To date, no satisfactory general explanation for fractional power law dependence of the conductivity has been found, although it has generally been attributed to the distributed nature of particle size and separation [4.10]. In the low electric field regime, the

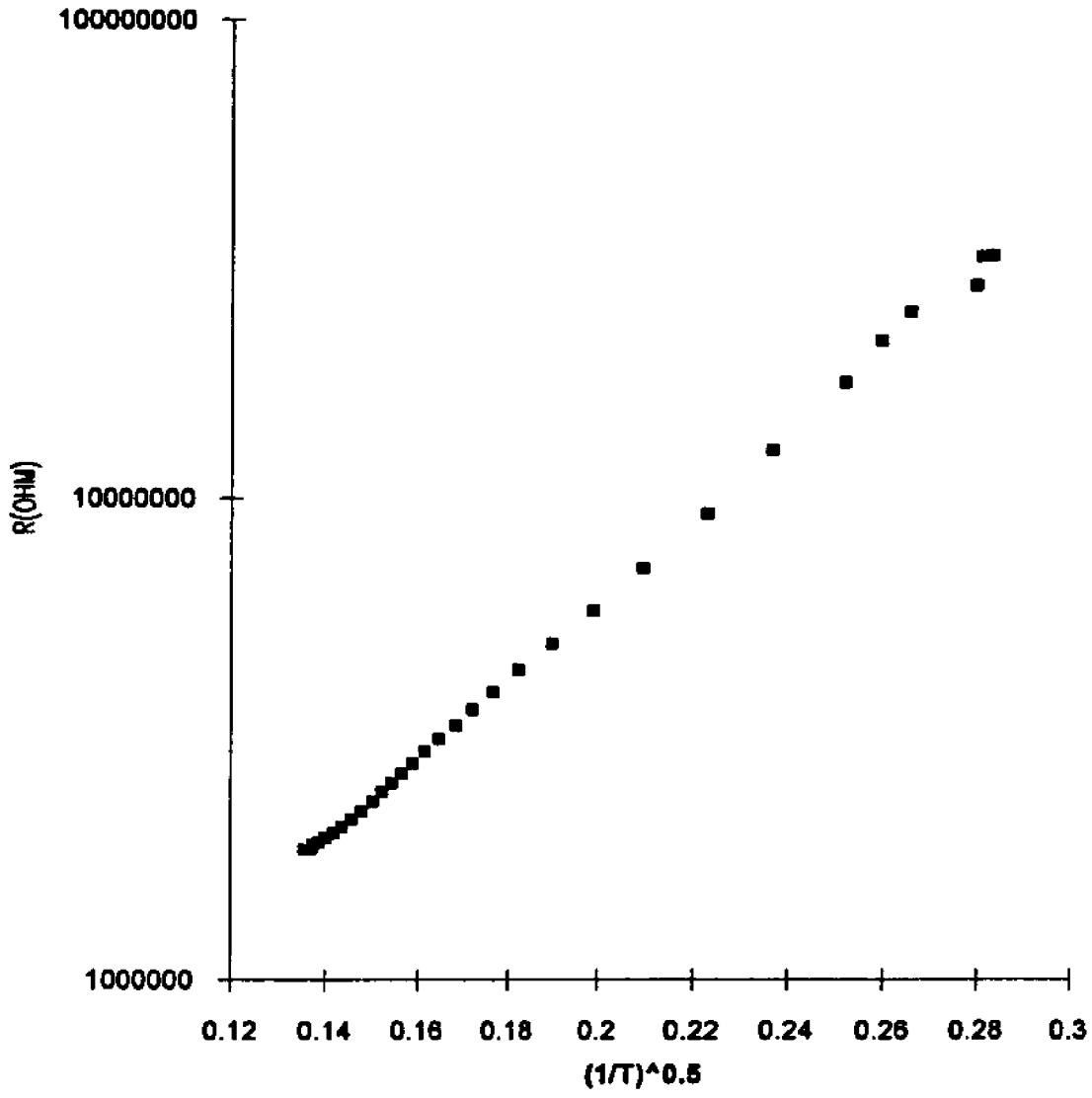

Figure 4.2. Granular potassium film after annealing to 56 K. The lnR versus the square root of 1/T shows linear dependence.

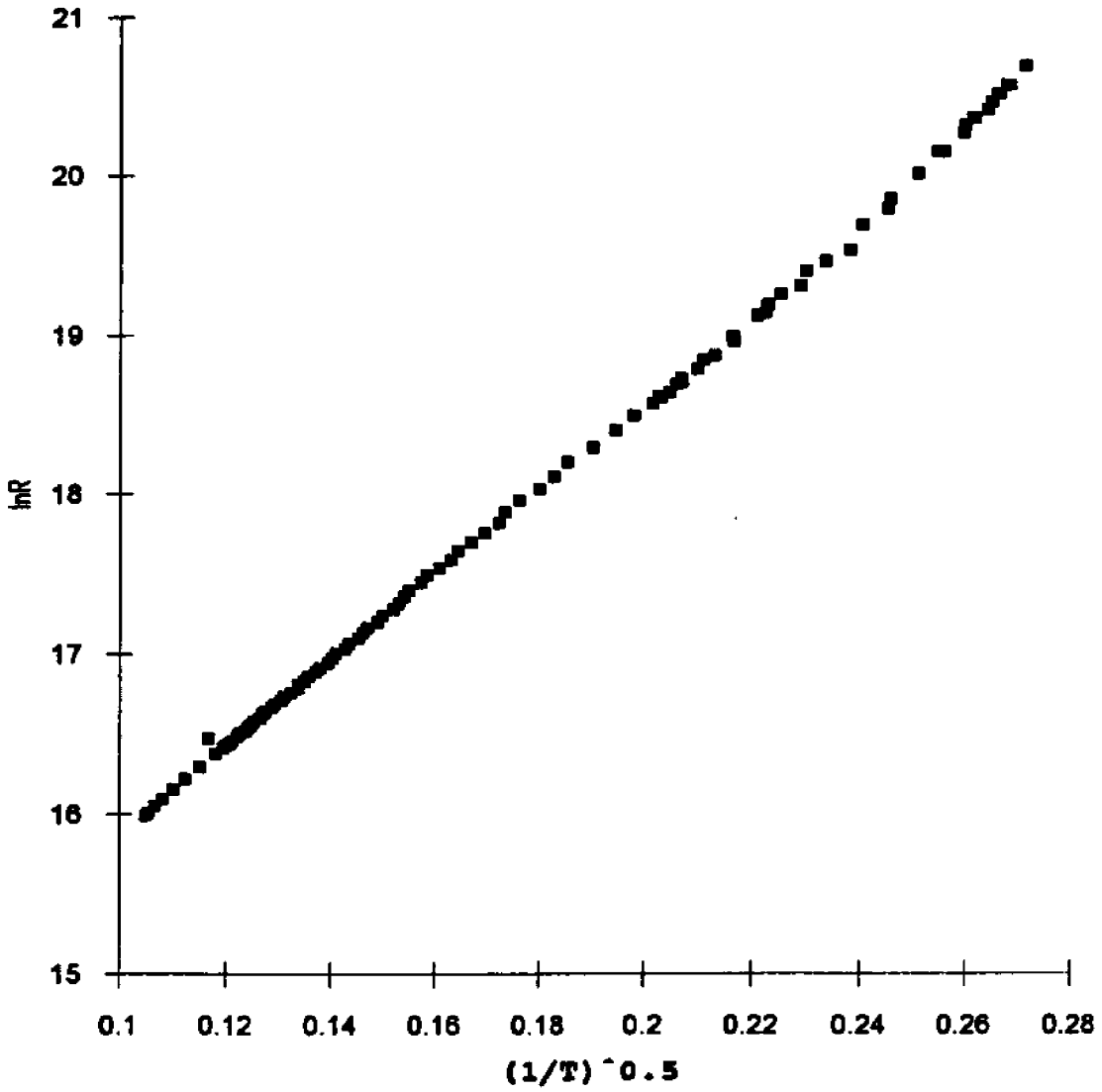

Figure 4.3. Granular gold film after annealing to 90 K. The lnR versus the square root of the 1/T also shows linear dependence.

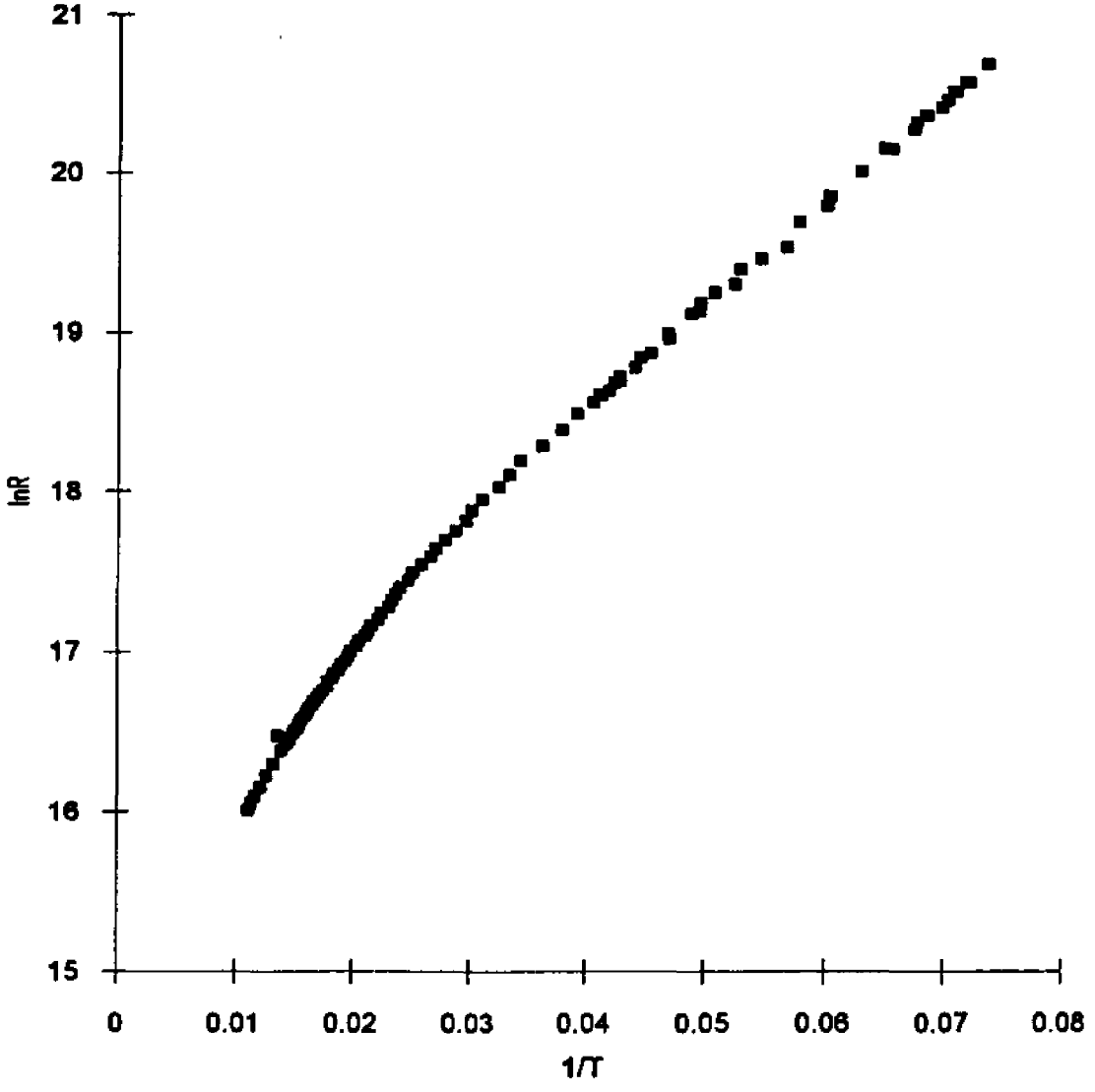

Figure 4.4a. Granular gold film after annealing to 90 K. One of the possible fits: lnR versus 1/T.

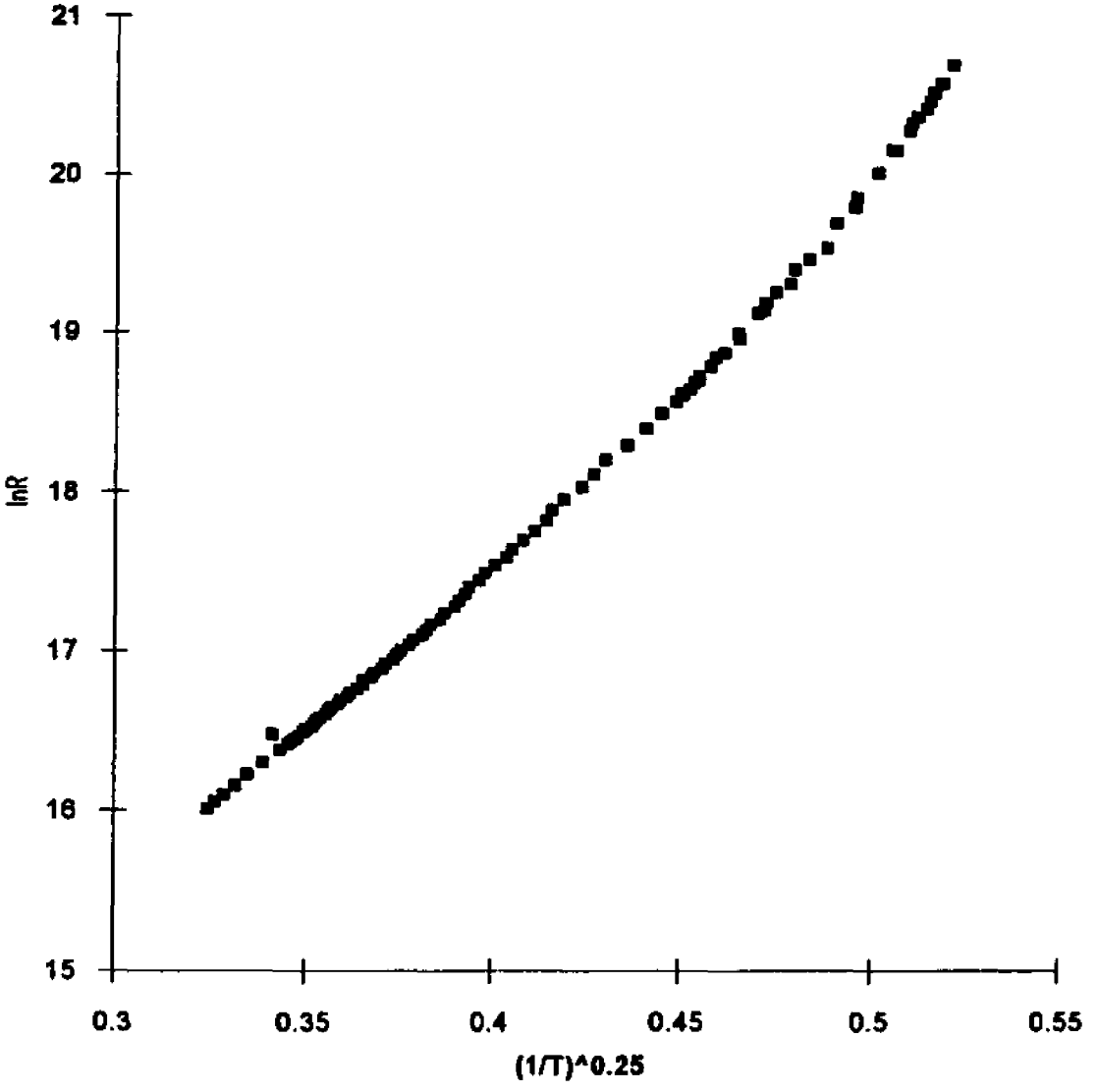

Figure 4.4b. Granular gold film after annealing to 90 K. The other possible fit with Mott's variable range hopping model: lnR versus (1/T)^0.25.

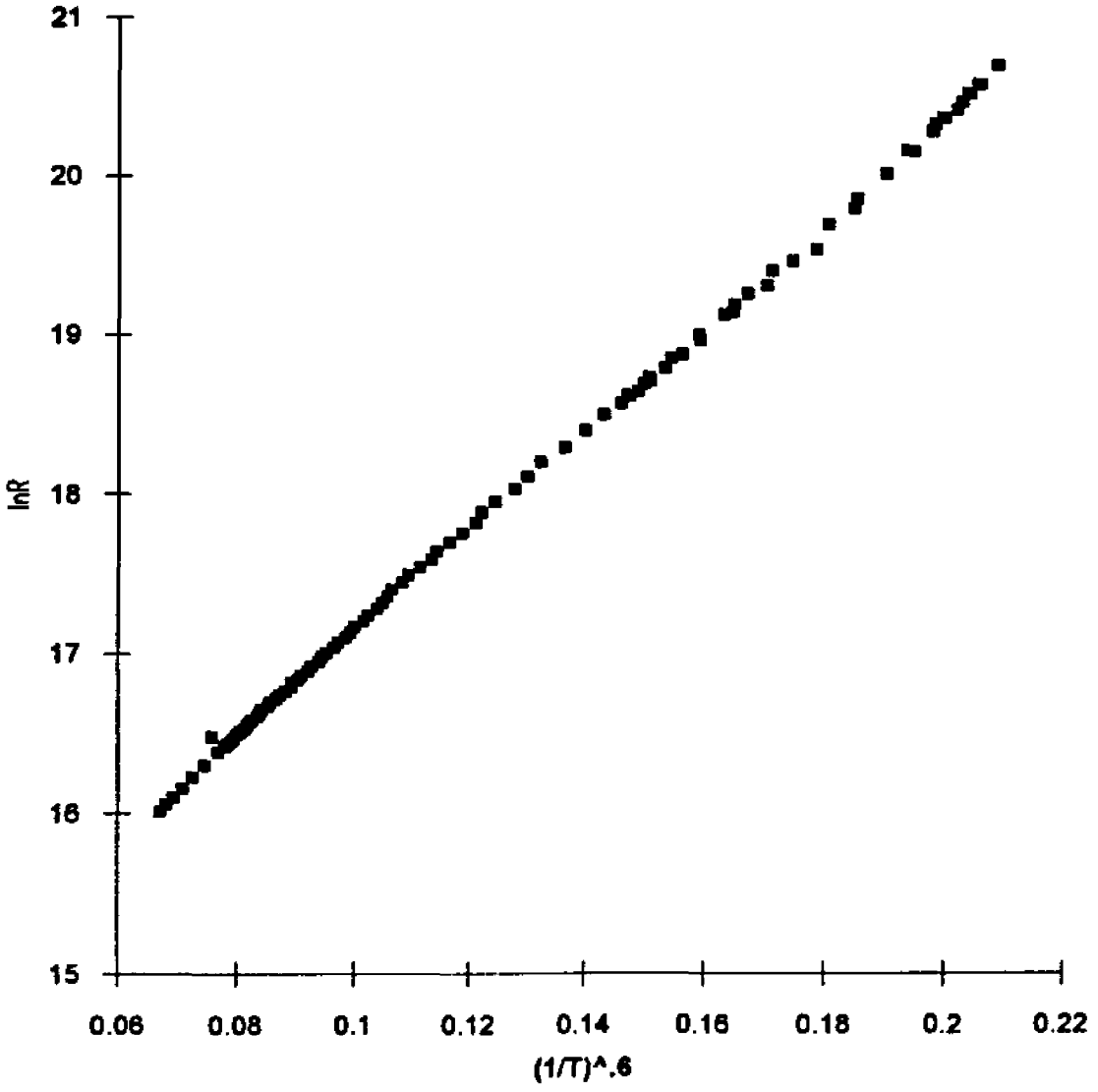

Figure 4.4c. Granular gold film after annealing to 90 K. Computer curve fitting result: lnR versus (1/T)^0.6.

transport of charge between grains is dominated by quantum mechanical tunneling, and activation is required because of the significant electrostatic energy associated with placing a single electronic charge on a grain. In the high electric field limit, the current density is proportional to the generation rate of charge carriers through field induced tunneling [4.11]. In this case, formula (2.12) is not valid any more. Because in our experiment we use a granular film as a detector, the low electric field regime applies.

4.4. Effect of Dielectric Media on Film Resistance

When dielectric media are introduced onto the annealed metal clusters, the film resistance should decrease because the Coulomb barrier is lowered by the screening effect. Figure 4.5 shows the experimental results for condensing xenon gas onto the granular potassium film. The potassium film was annealed to 50 K before introducing xenon. Then xenon gas was introduced into the experimental chamber at time = 110 minutes in figure 4.5. As the xenon gas was introduced into the chamber at 1×10^{-7} Torr, the film resistance began to drop. The initial rate of decrease of the film resistance was fast, and then it slowed down. When the

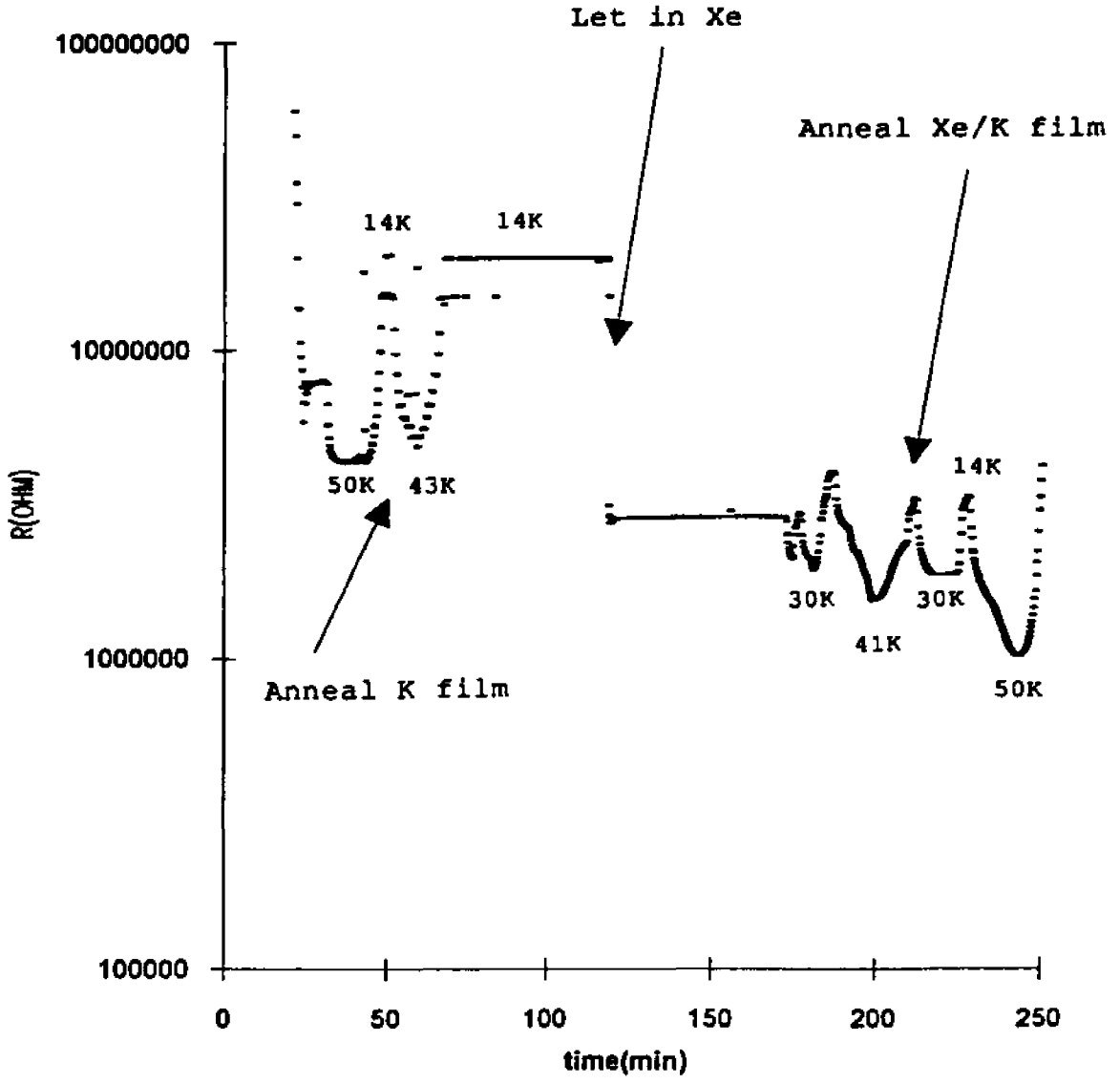

Figure 4.5. The time evolution of xenon condensed on granular potassium film.The potassium film was annealed several times in the time interval between 20 and 70 min. The xenon was introduced into the chamber at t = 110 min. From 160 to 240 min, the potassium film with condensed xenon was annealed several times again.

rate of decrease of the film resistance was less than one xenon to the chamber was closed. During the condensation of xenon, the pressure inside the chamber was about 1 x 10^{-6} Torr as indicated by the ionization gauge; the time of exposure was about 5 minutes. A heat shield, which was cooled by the exiting liquid helium gas, protected most of the sample holder from thermal radiation; only a small opening on the shield allowed gas molecules to reach the sample. Compared to the gas exposure without the heat shield, only about six percent of the molecules could reach the sample. Therefore, the estimated total xenon exposure was about 20 Langmuir. After this procedure, we annealed the potassium film with the condensed solid xenon again in order to get the temperature dependence of the film resistance. Similar results of xenon condensed on the granular gold film is shown in Figure 4.6.

Figure 4.7 is the plot of the natural logarithm of the potassium film resistance versus the square root of the inverse of the sample temperatures. Similar experimental results for xenon condensed on gold film is shown in Figure 4.8. The upper curve, with a larger film resistance, was characteristic of the resistance of pure granular metal films versus temperature in the regime which we are interested. The

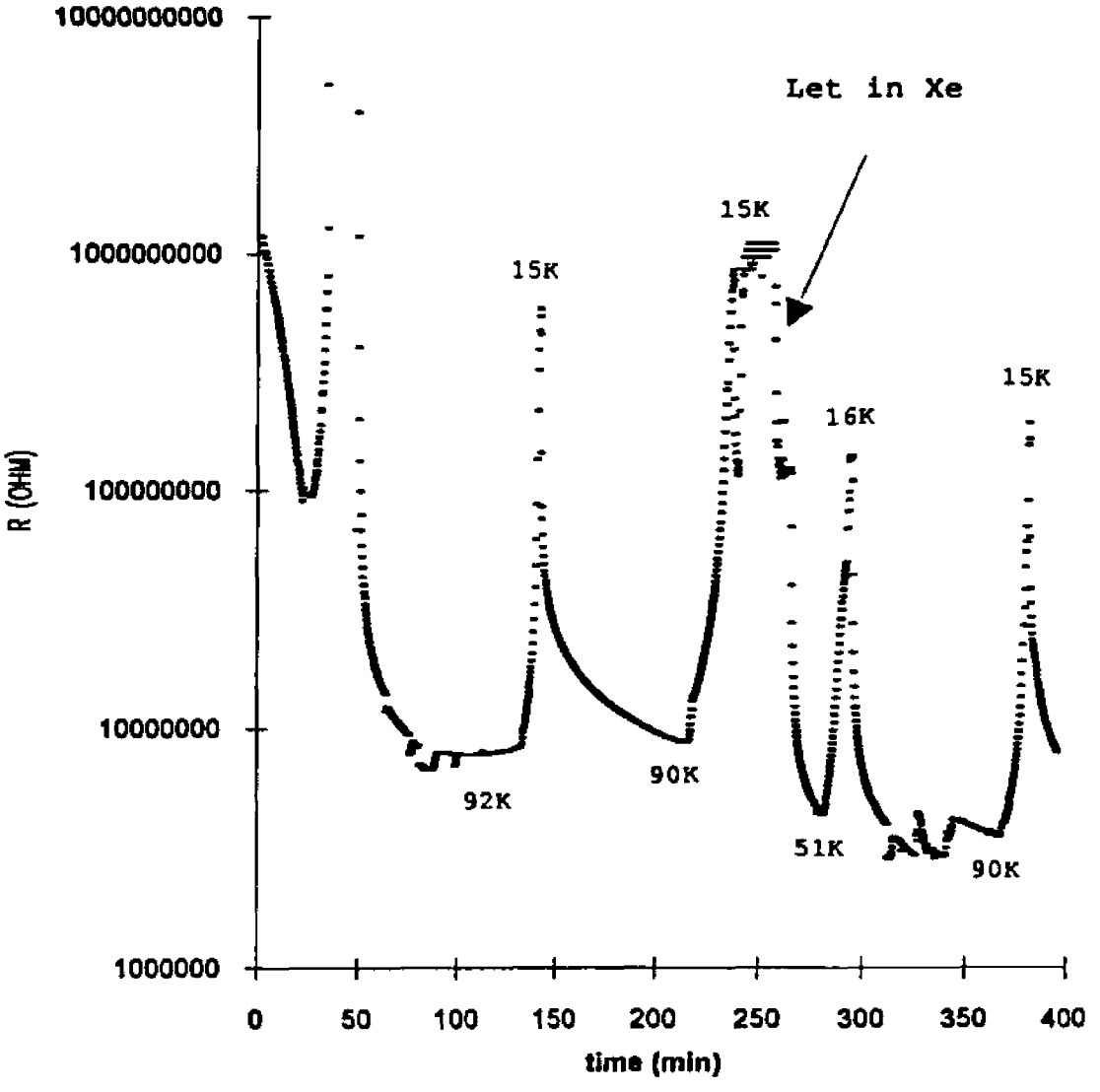

Figure 4.6. The time evolution of xenon condensed on granular gold film. From 50 to 230 minute, the gold film was annealed twice. The xenon was introduced into the chamber at t = 260 minute. From 270 to 400 minute, the gold film with condensed xenon was annealed several times.

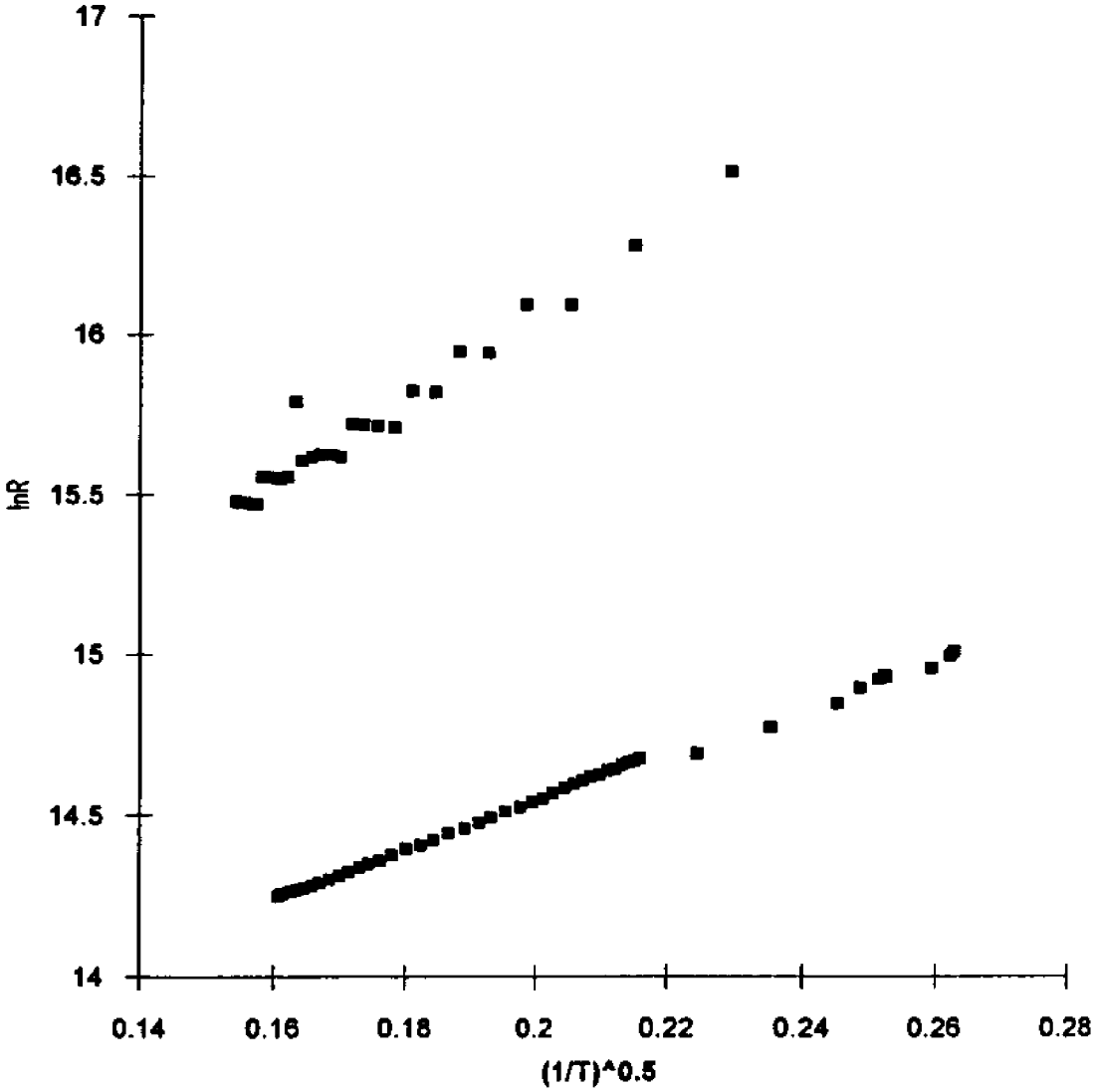

Figure 4.7. The effect of xenon as a dielectric media on granular potassium film. The upper curve is a pure potassium film. The lower curve is the xenon-covered potassium film.

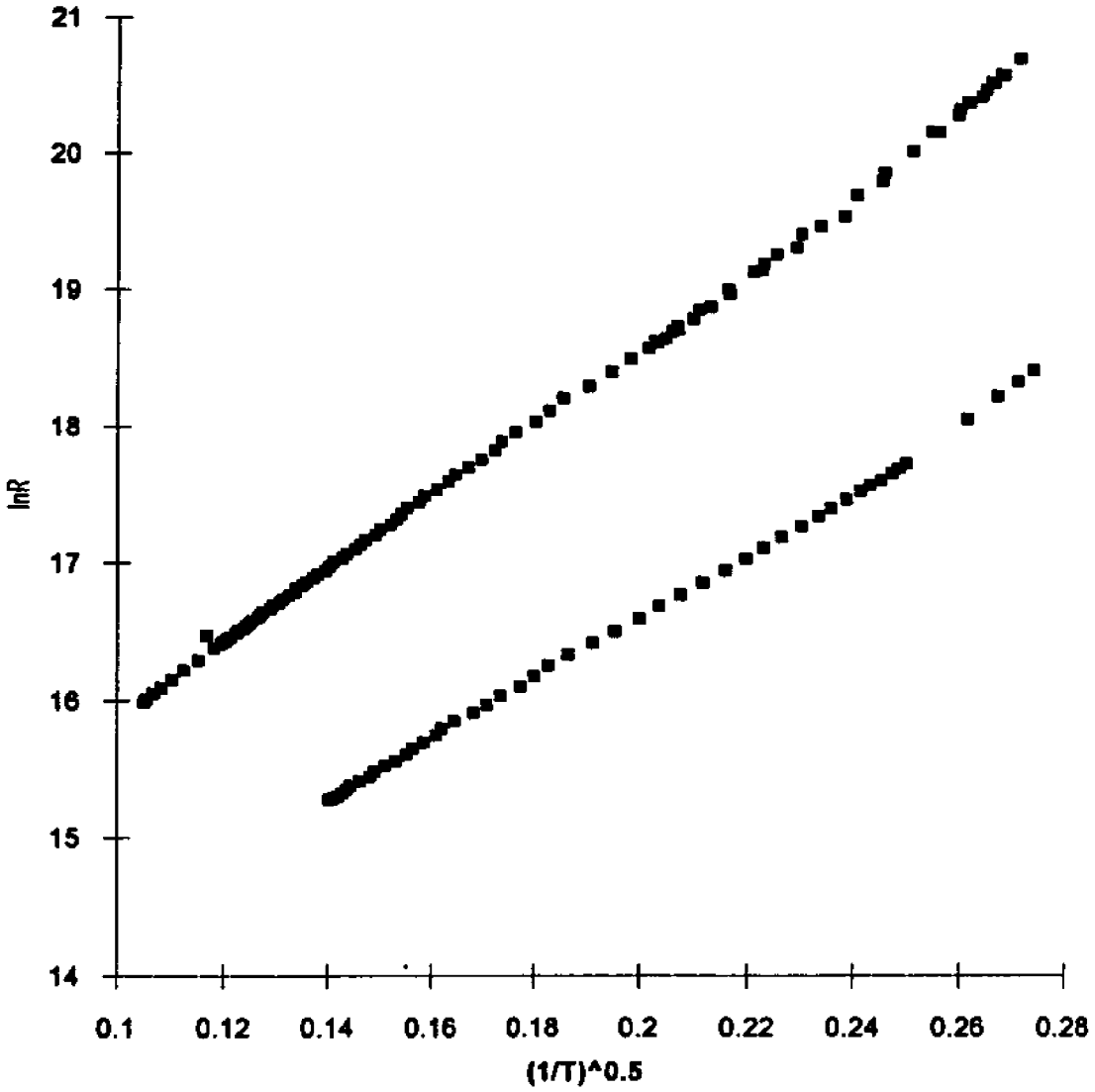

Figure 4.8. The effect of xenon as a dielectric media on granular gold film. The upper curve is a pure potassium film. The lower curve is the xenon-covered gold film.

lower curve, with a smaller film resistance, showed the differences caused by the condensed solid xenon. Both the slope of the straight line and the initial resistance (R_0) were changed after xenon was condensed on the metal film. The change of the slope could be understood by looking at formula (2.12), where the dielectric constant is very important in determining the height of the activation barrier for electrons hopping in between metal clusters. According to formula (2.12), the slope of the granular potassium film in Figure 4.7, divided by the slope of xenon on potassium film is proportional to the square root of the dielectric constant of solid xenon. From this, the average dielectric constant of solid xenon was found to be about 2.3 ± 0.8 which is in relatively good agreement with published experimental results 2.0 using different methods [4.12, 4.13]. This measurement was the first direct experimental proof of dielectric media changing the coulomb barrier in granular films.

Observing the change of film resistance by introducing an inert gas is significant considering that the glass substrate had a dielectric constant of 4. This raises a question about what caused the change of film resistance. Was the change due to some artificial effect when the film was

exposed to the inert gas (for instance, if the film geometric structure was changed by condensing an inert gas on top of it) or just due to the change of the dielectric constant between the metal clusters? To answer this question, we repeated the same experiment using gold films (which could be annealed to a higher temperature of 90 K, and are less reactive with the ambient gas than the potassium film) and krypton as the dielectric media, This was done since krypton has a higher vapor pressure than xenon; about 10 Torr at 90 K and thus we could check if the film resistance returned to the starting value after the krypton was boiled off. The experimental result is shown in Figure 4.9. The quench condensed gold film was annealed to 90 K first, then the krypton gas was introduced into the chamber. The change of film resistance caused by condensing krypton gas was smaller than that of xenon due to the smaller dielectric constant. After a few short temperature range annealing cycles, the film was warmed up to 90 K. As most of the krypton was pumped out, the film resistance went back to almost the same value before exposure to the krypton gas. Figure 4.10 is a comparison of the resistances of the gold film before introducing krypton and after boiling off the krypton. At the lower end of the x-axis (higher temperature end) of the

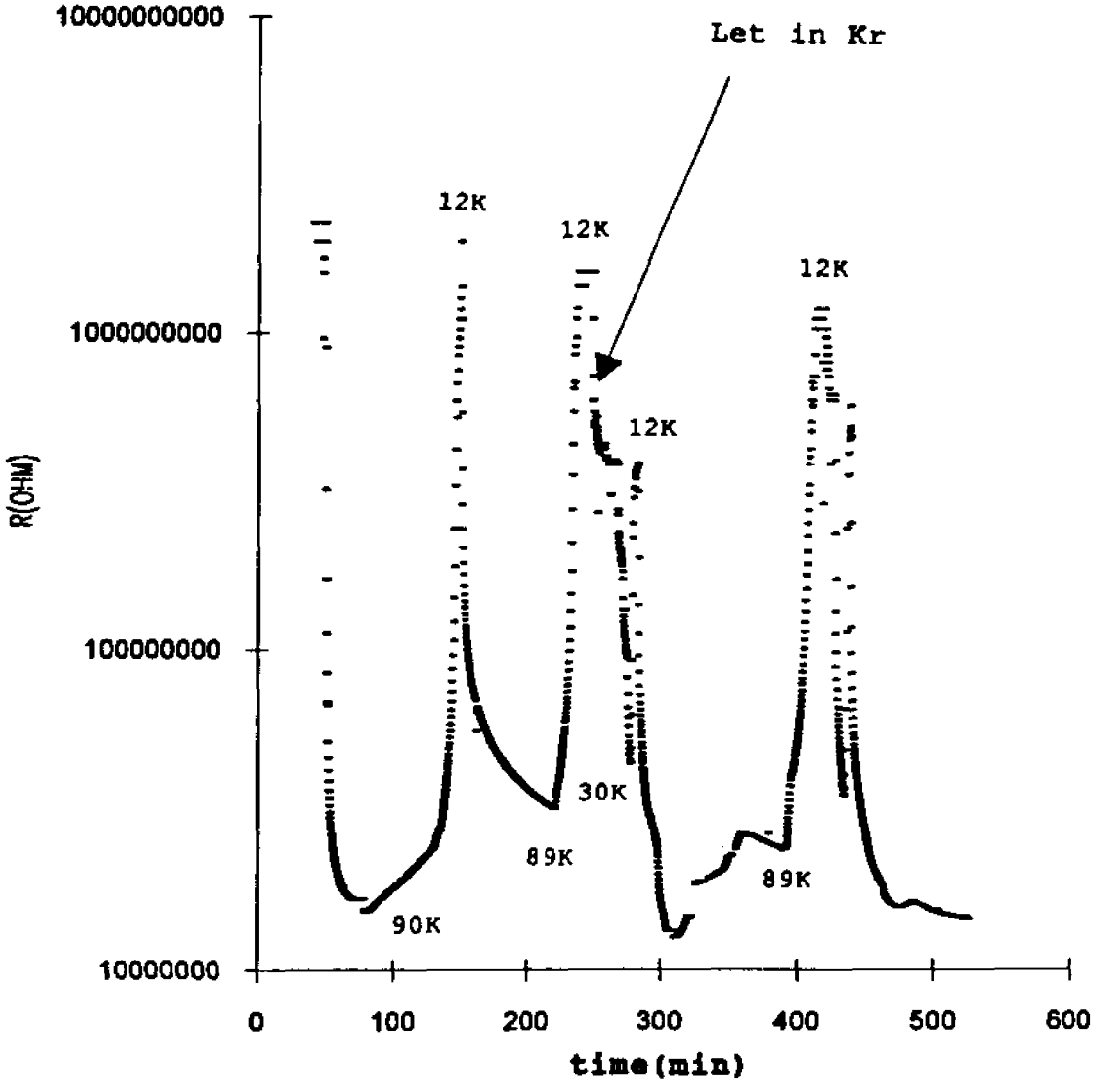

Figure 4.9. The time evolution of krypton condensed on granular gold film. From 50 to 230 minute, the gold film was annealed twice. The krypton was introduced into the chamber at t = 250 minute. The gold film with condensed krypton was annealed at t =280 minute. Then, it was warmed up to 89 K to remove krypton. The resistance almost went back to where it started with after cooled down to 12 K.

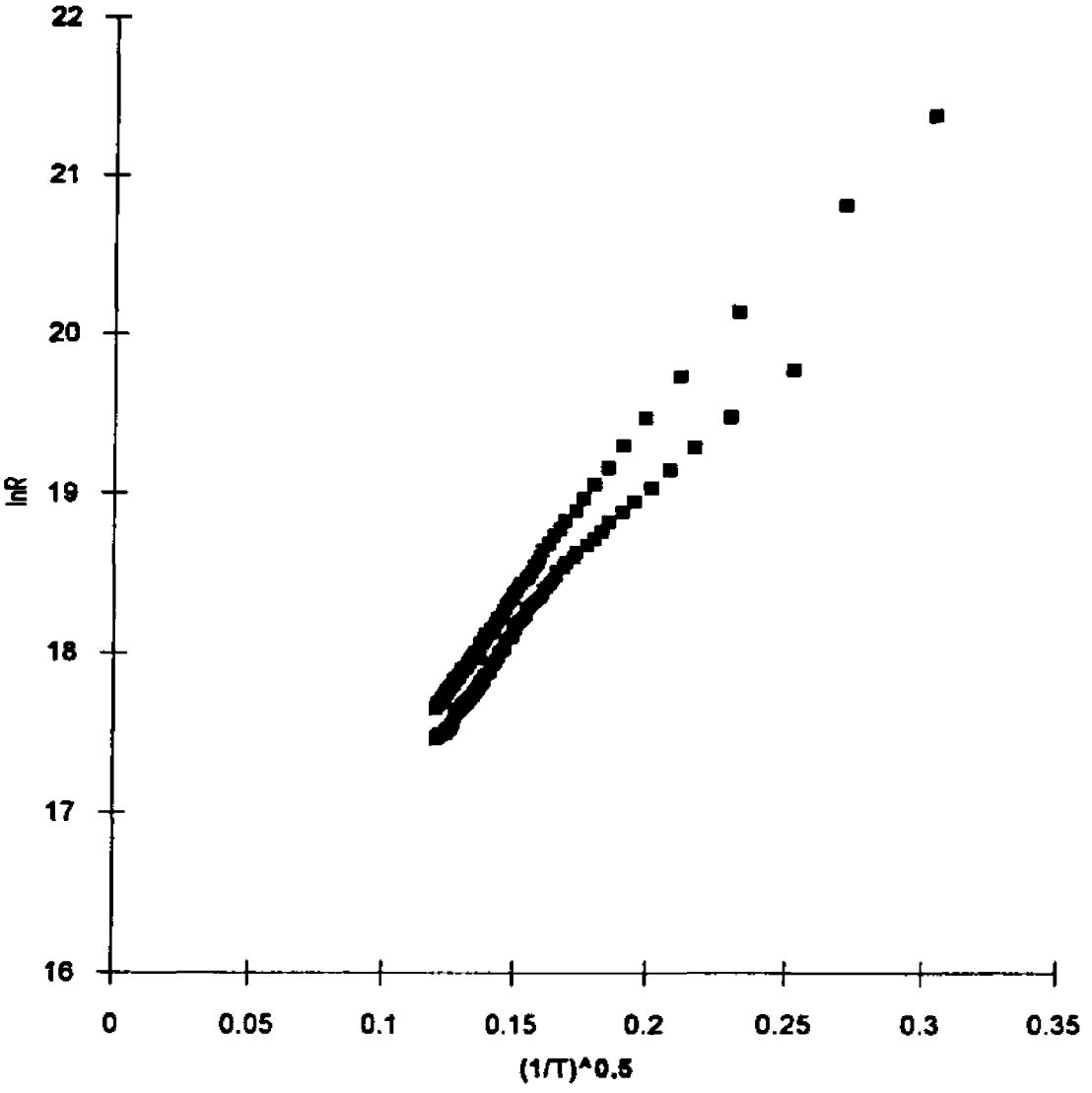

Figure 4.10. Comparison of the characteristic of granular gold film before introducing krypton and after removing krypton by warming up to 89 K. The upper curve was the characteristic of gold film. The lower curve was characteristic of the film after warming up to 89 K to remove krypton.

figure, the two curves were very close to each other. At the higher end of x-axis (lower temperature end) of the figure, the discrepancy between the two curves was probably caused by the recondensation of the residual krypton gas in the chamber onto the film. This result suggests that most of the film resistance changes were not due to any change of the film geometric structure caused by condensing inert gas on it.

Table 4.1 shows the dielectric constants of solid krypton and xenon from our experimental data. Comparing to the data in the literature, it shows general agreement. From these results, it seems that the substrate did little to contribute to the film conductivity. One possible explanation for this is that, although the high dielectric constant of the glass substrate lowers the tunneling barrier, the path of the tunneling electron is relatively long except when it is close to the substrate-vacuum interface. Since the distance appears in the exponent, this can be significant. Similarly, the results of detailed studies by Van Steensel [4.14] on Au and Pb films showed that the conductivity did not change as the dielectric constant of the $BaTiO_3$ substrate was varied.

Sources	Xenon	Krypton
[4.12]	2.09	1.79
[4.13]	2.033 ± 0.01	1.784 ± 0.01
our results	2.3 ± 0.8	1.9 ± 0.3

Table 4.1. Dielectric constant of solid xenon and krypton

Chapter 5. Low Temperature Charge Transfer in the Alkali Metal-Ammonia System

5.1. Introduction

The investigation of chemical reactions on metal surfaces at low temperatures offers a number of important advantages. Firstly, the thermal energy of molecules is very small at low temperatures. Near absolute zero all molecules move to the zero-point energy level. The quantum mechanical effects might be the dominant reason for chemical reaction. Secondly, the sticking coefficient of gases at 60 K is higher than at room temperature. Enough gaseous ammonia can be condensed onto alkali metal surface to form cavities, which accommodate solvated electrons and ions. Thirdly, intermediate products of a chemical reaction may be frozen-in. At a sample temperature as low as 10 K, there are some photoelectron spectroscopy studies on rare gases [5.1], isolated molecules such as CO, O_2 or N_2 [5.2, - 5.4], and even matrix-isolated metal atoms [5.5, 5.6]. Goldanskii *et al.* observed the low temperature quantum limit of the chemical reaction rate in spontaneous chain growth during the radiation induced polymerization of solid formaldehyde [5.7].

In their experiments the polymer chain lengths and growth rate were measured at 4.2 - 140 K by high-sensitivity and rather fast calorimeters. A quantum characteristic low temperature plateau of the rate of polymerization was observed in the experiments.

In this chapter, we will discuss the results of resistivity measurement for alkali metal-ammonia system in section 5.2. The resistivity of granular alkali metal film is a very sensitive indicator of small changes in the system (see chapter four for details). Although resistivity measurements are very sensitive to small changes within the system, it lacks the details of those changes. As to the question of what the reaction reaction products are, we have to employ other measurements, for example photoelectron spectroscopy (PES), to find out. Photoemission can provide more specific information about the reaction products, but it is not very sensitive to a small amount of reaction products. A combination of the two measurements gave us deeper insight into the ammonia-potassium system. The results for the photoemission study of ammonia-potassium system are discussed in section 5.3, which includes four subsections. In section 5.4, we have tried to relate the observations with the

simplest possible models in this still developing field. The models presented in section 5.4 serve the same purpose they do in all branches of physics, that is, to organize the experimental observations and to establish elementary relationships between observed effects at a more basic level. The models, which are used to interpret experimental results, are by no means perfect.

5.2. Resistivity Study of Alkali Metal-Ammonia System

So far we have discussed a system in which the condensed inert gas acts only as a dielectric media which changes the film resistance by lowering the Coulomb energy for hopping. This is not a chemical-reaction related process. The film resistance versus temperature curve was reversible after annealing. When the inert gas was vaporized, the film resistance went back to the same value it had before introducing the gas. In this section, we are going to discuss an even more complicated system which involves a chemical reaction between the potassium clusters and the ammonia media.

Figure 5.1 shows the typical experimental results for condensing ammonia onto the potassium film. The x-axis

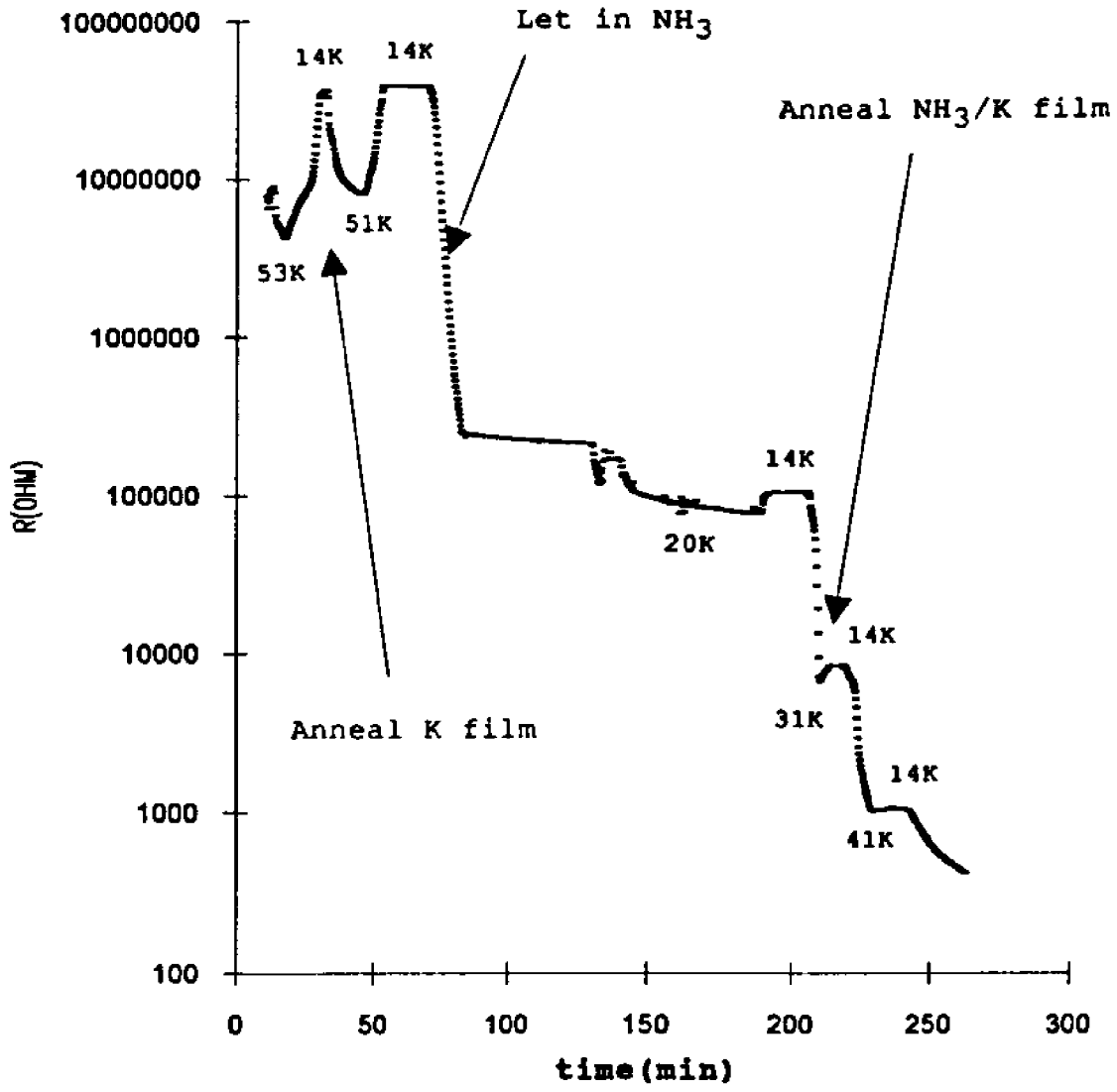

Figure 5.1. The time evolution of ammonia condensed on granular potassium film. From 20 to 60 minute, the potassium film was annealed twice. The ammonia was introduced into the chamber at t = 64 minute. From 75 to 120 minute, the sample was held at 14K. Then the sample was cycled between 20 to 14 K, 31 to 14K and 41 to 14K.

denotes the time after starting the experiment. After being quench condensed onto the glass substrate, the potassium film was annealed to 53 K and then cooled down to 14 K. Ammonia was leaked into the chamber through a gas manifold at 64 minute on our scale and stopped at 75 minute, by which time additional exposure of ammonia had almost no effect on the film resistance. The fast decrease of film resistance as ammonia was introduced into the chamber is mostly a physical effect, due to the change of dielectric constant of media similar to the effect seen when condensing xenon or krypton onto granular metal film. After that, the residual ammonia was pumped out and the sample was held at 14 K for 39 minutes. During this period, the film resistance still decreased slowly, even though the experimental conditions were the same. This is in contrast to the case where inert gases were condensed onto potassium or the pure potassium film, the film resistance increased very little or not at all in contrast to the result of ammonia condensed onto potassium films.

Before we further discuss experimental results, it is useful to point out that atomic diffusion is not the most likely cause for the change of film resistance. The diffusion coefficient can be estimated by a simple calculation. The

diffusion coefficient of solvated electron is 1.3×10^{-4} cm^2/s at 218 K, which is larger than that of potassium. The activation energy W of diffusion is 1.93 kcal/mol (~0.084 eV) [5.8], which is smaller than that of potassium. The experimentally measured diffusion coefficient is usually presented as

$$D = D_0 \exp(-W/kT) \qquad (5.1)$$

If the experiment is carried out at 10 K, then the upper limit of the diffusion coefficient of potassium is about 10^{-44} cm^2/s.

All the theoretical models proposed so far, deal with systems where the grain size of the granular film or composition of the cermet (ceramic metal) is constant. When ammonia was introduced into the UHV chamber and condensed onto the potassium clusters, the slow decrease of film resistance can be formulated by assuming that the effective radius of a given potassium cluster has the following form

$$r(t) = r_0 + \beta(T)t \qquad (5.2)$$

where "r_0" is the effective radius of a potassium cluster before introducing ammonia, "t" the time after introducing ammonia, and $\beta(T)$ is the temperature dependent coefficient of the ammonia-potassium system, which describes the growth rate of the effective grain size. The experiment showed that at a

temperature below 20 K, the growth of the grain size was very small, even after a long period. Therefore, it is safe to assume that $\beta(T)t$ is much smaller than r_0. Substituting equation (5.2) into (2.12) and taking the first order Taylor expansion:

$$\sigma = \sigma_0 \exp[-(e^2/\varepsilon r_0 k_B T)^{1/2}(2r_0 - \beta t)/2r_0] \qquad (5.3)$$

or in terms of resistance,

$$\ln(R/R_0) = (e^2/\varepsilon r_0 k_B T)^{1/2}(1 - \beta t/2r_0) \qquad (5.4)$$

Formulas (5.4) implies that the logarithm of film resistance is a linear function of time as long as $\beta(T)t$ is much smaller than r_0. If one knows the size of the potassium cluster before introducing ammonia, then the rate of increase of the effective radius of the cluster after introducing ammonia can be obtained from experimental data using equation (5.4). Basically, $\beta(T)$ is proportional to the potassium dissolution rate at a certain temperature, which was very low in our experiments. This provides an alternative method to study the low temperature chemical reactions. The experimental results of the slow change of film resistance with time at constant temperatures are shown in figure 5.2. In order to compare the slopes of different lines, the time-axis of one of the two lines has been shifted by a constant to overlap that of the

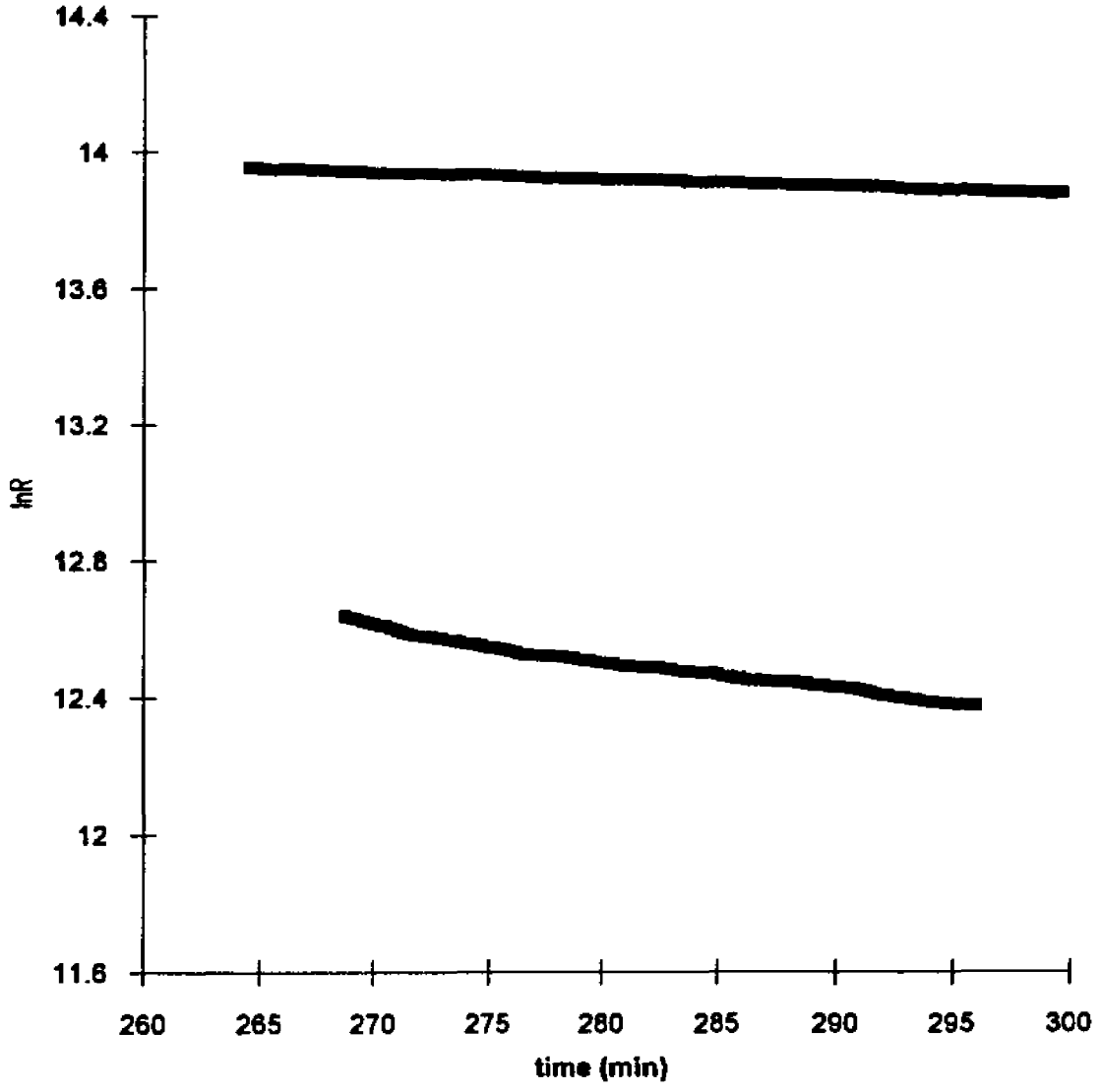

Figure 5.2. The change of film resistance with time for potassium with condensed ammonia at constant temperatures. The temperature of the upper curve was at 12.5 K, that of the lower curve was at 21.2 K.

other line. It is clear that the change of natural logarithm of the film resistance versus time at 21.2 K is bigger than that at 12.5 K. This result is expected using the solvation model discussed in section 5.4.1 (for the details of the model please see section 5.4.1). As the sample temperature increases, more cavities could be formed in the ammonia as a result more electrons could tunnel into the ammonia and the potassium dissolve into the ammonia more rapidly.

When the temperature was raised above 20 K, the film resistance dropped quickly and the change was irreversible (see Figure 5.1) which is quite different from the xenon-potassium and krypton-potassium systems. The rapid decrease of film resistance was caused by a combination of the temperature dependence of granular film and the potassium dissolving process discussed before. When the sample temperature was increased, more ammonia molecules had enough energy to move around and as a result more potassium would dissolve into ammonia media. The solvated electrons and potassium cations might also gain enough energy to delocalize themselves. As a result, some of them may contribute directly to the increase of film resistance, which is similar to those of classical electrochemistry reactions. Some of them may be

able to recombine and become neutral atoms again. In this way, either the size of the potassium cluster increased or the distances between clusters decreased. Both of these factors could contribute to a smaller film resistance. The third possible contribution might come from protons. We could not determine this just by the resistivity measurement but the photoemission experiments, which we are going to discuss in detail in next section, showed the formation of nitrogen molecules. That means the bonds between hydrogen and nitrogen in ammonia molecule must have been broken, resulting in the release of protons. The positively charged proton could contribute to the film conductivity before it captures an electron and becomes a neutral atom. The irreversible nature of the film resistivity with temperature in the ammonia-potassium system, which is clearly different from that of the xenon-potassium or krypton-potassium system, is strong evidence of the chemical changes in the system.

As the sample was warmed up to 170 K or so, the film became discontinuous which means the film resistance was bigger than 30 GΩ. The vapor pressure of ammonia is 1 Torr at 160 K, which means at this temperature almost all the ammonia had already left the sample. Films stays continuous at 100 K even though most ammonia is gas. But even right before the

film broke, the film resistance stayed at almost the same value as that before the ammonia came off the sample. For similar pure potassium metal film or the potassium film with condensed xenon or krypton on it, the film usually breaks when warming up to about 80 K. This result implies that the microgeometrical structure of potassium film has been changed due to chemical reactions in ammonia-potassium system.

The results for condensing ammonia onto lithium, sodium and cesium films are shown in figures 5.3, 5.4 and 5.5, respectively, which is quite similar to the results for condensing ammonia onto potassium films. The effect due to differences in the size, mass and work function among the sodium, potassium and cesium could not be distinguished in our experiments, due to the distributed nature of the film growth process. In another words, the fluctuations between different runs is bigger than the differences among lithium, sodium, potassium and caesium. These results also prove indirectly that the atomic diffusion is not a major cause of the changes in the film resistance.

When potassium was deposited into ammonia matrix, it only took one eighth of the amount of the potassium as it had when deposited directly onto the glass slide to reach the

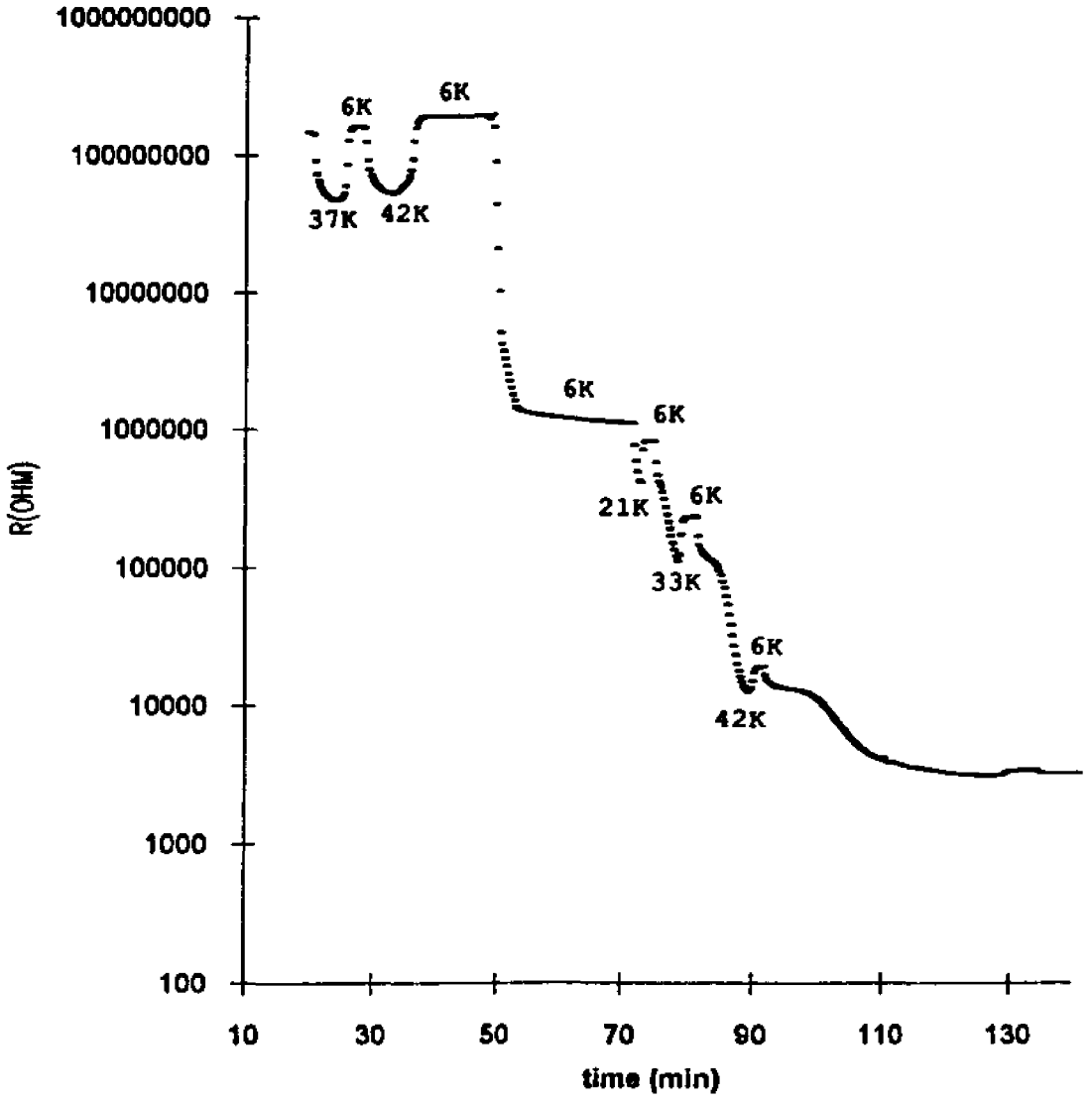

Figure 5.3. The time evolution of ammonia condensed on granular lithium film. From 17 to 40 minute, the lithium film was annealed twice. The ammonia was introduced into the chamber at t = 48 minute. From 54 to 72 minute, the sample was held at 6 K. Then the sample was cycled between 21 to 6 K, 33 to 6 K and 42 to 6 K.

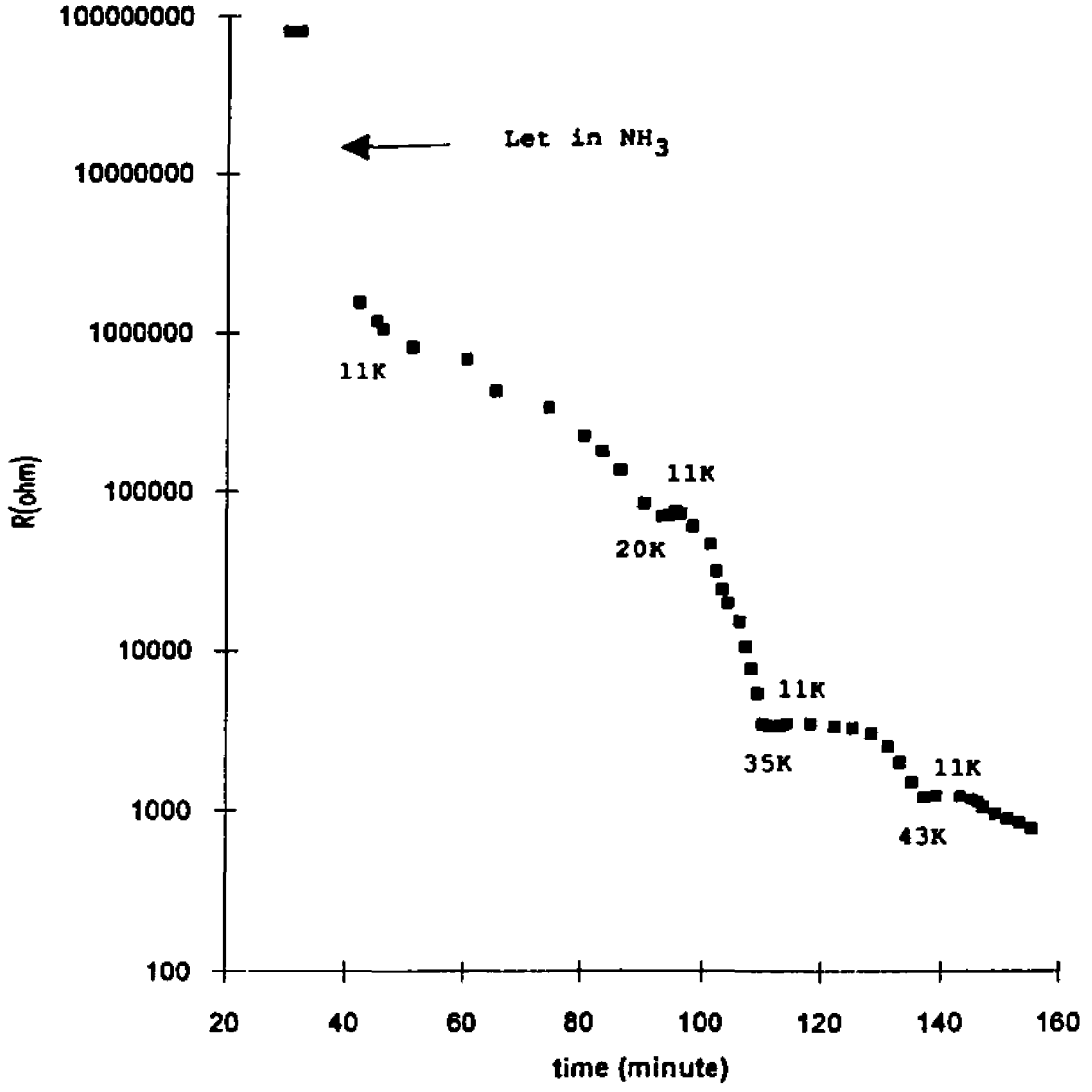

Figure 5.4. The time evolution of ammonia condensed on granular sodium film. The ammonia was introduced into the chamber at t = 35 minute. Then the sample was cycled between 20 to 11 K, 35 to 11 K and 43 to 11K.

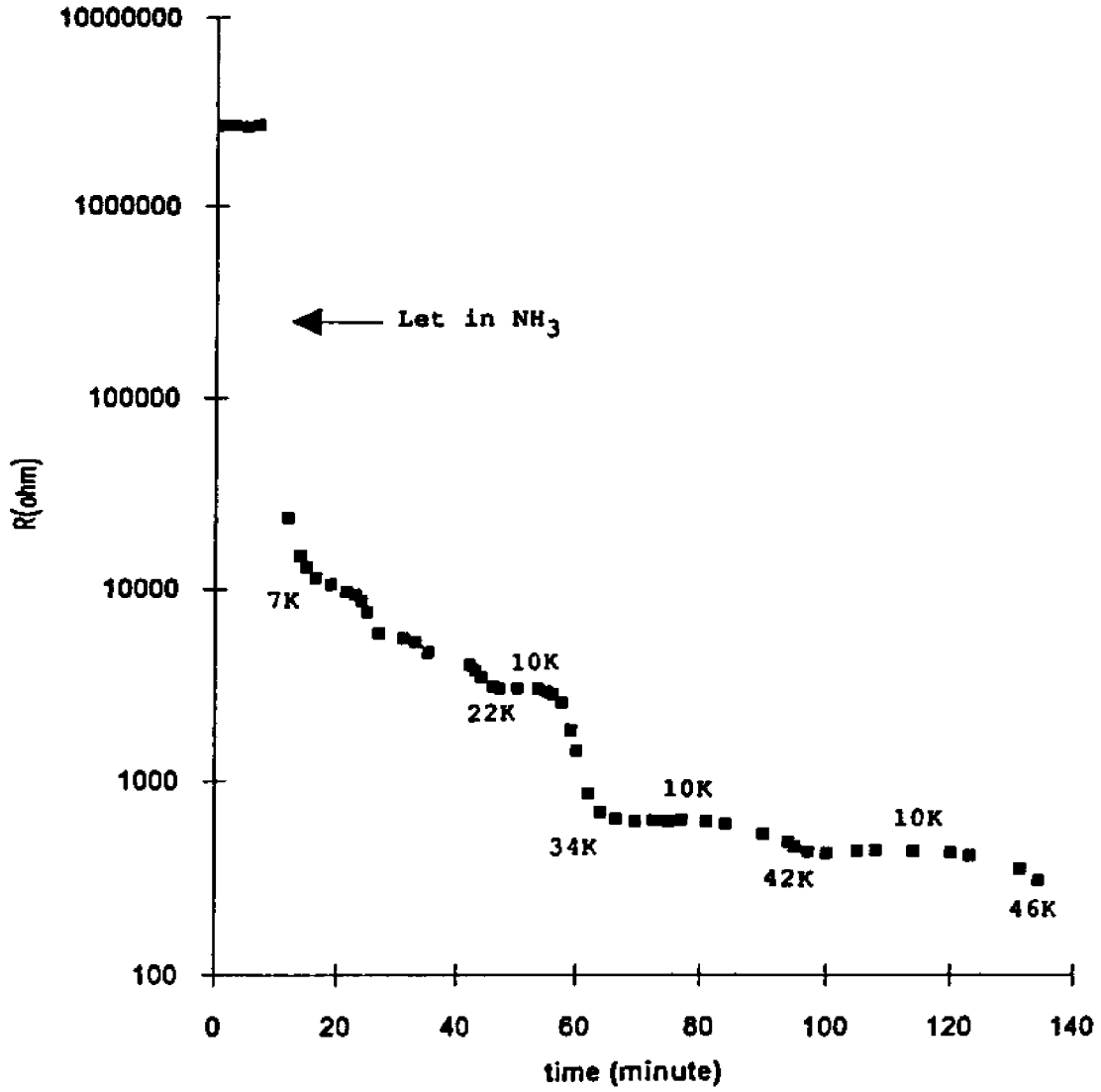

Figure 5.5. The time evolution of ammonia condensed on granular caesium film. The ammonia was introduced into the chamber at t = 10 minute. Then the sample was cycled between 22 to 10 K, 34 to 10 K and 42 to 10 K.

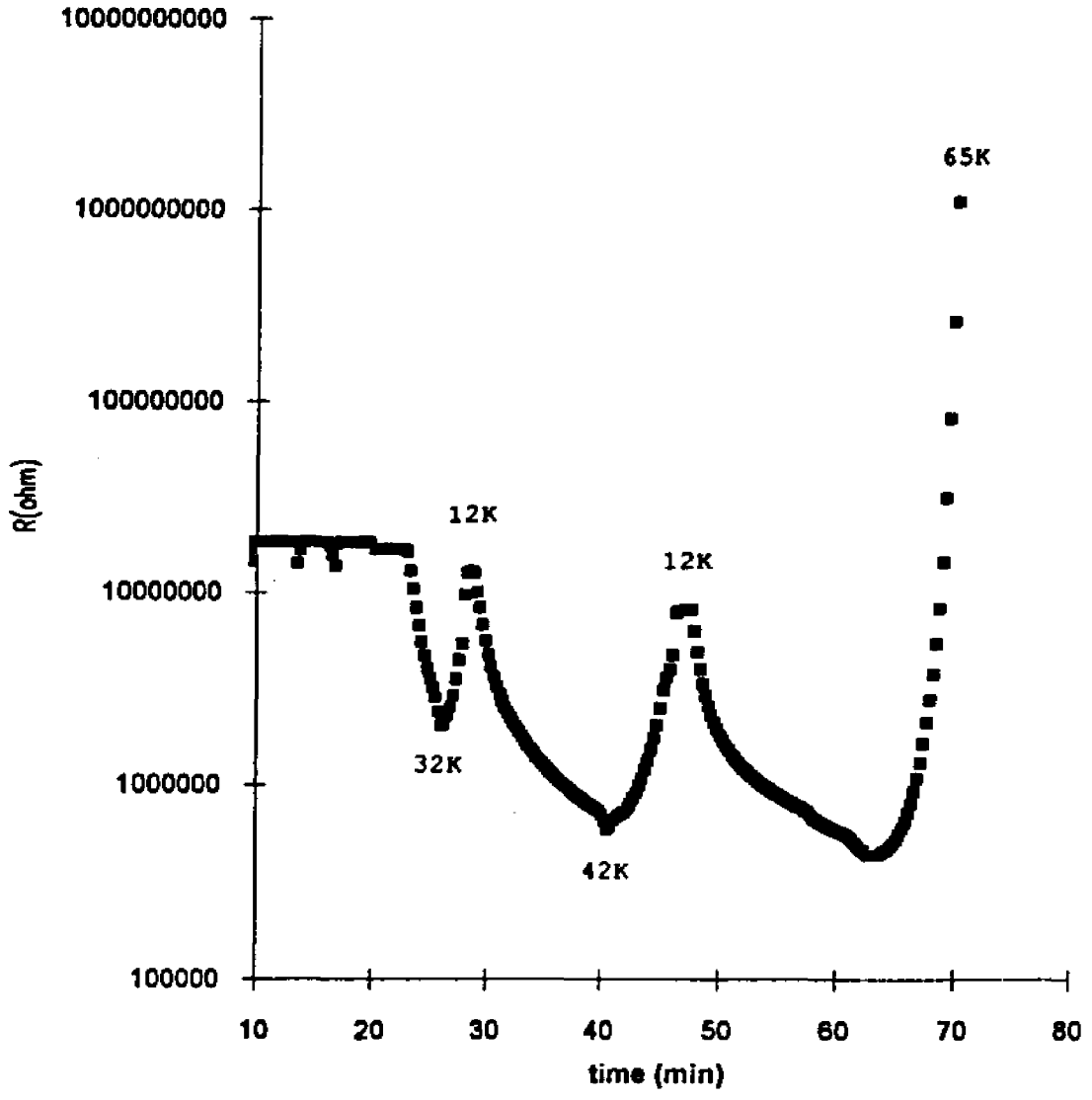

Figure 5.6. The time evolution after depositing potassium into solid ammonia matrix. Then the film was cycled between 32 to 12 K and 42 to 12 K. The film became discontinuous when warmed up to 65 K.

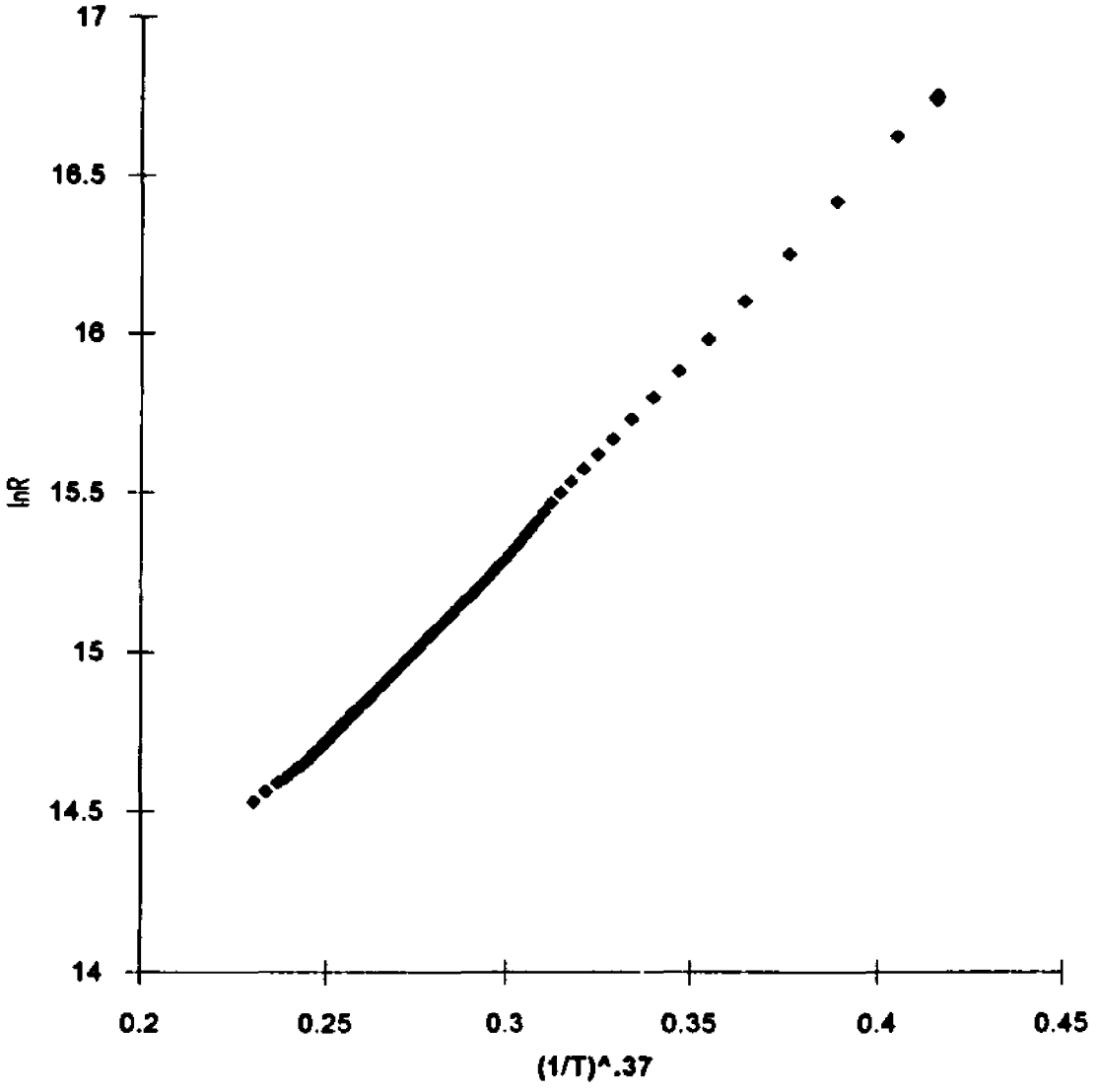

Figure 5.6a. The lnR versus (1/T)^0.37 plot: computer curve fitting result for potassium deposited onto a solid ammonia matrix.

same film resistance. This shows that potassium has the tendency to dissolve into the ammonia matrix. The film resistance change with temperature was reversible (see Figure 5.6 for details), but the film broke at lower temperatures (around 60 K). The resistances of the films prepared in this way seem also to follow the fractional power dependence of the temperature:

$$R = R_0 \exp(T_2/T)^x \qquad (5.5)$$

Due to the relatively short temperature range available in this arrangement, we could not determine the x value precisely. Computer curve fitting result of x was 0.37. The importance of this experiment is to show that potassium tends to form some kind of "bond" with ammonia.

The electric field between neighboring clusters was less than 200 Volts/cm, it was in the low electric field region. Even though, to ensure the phenomena in the ammonia-potassium system are real and not caused by the small DC electric field, AC measurements were carried out with a lock-in amplifier (Princeton Applied Research, Model 124A). The AC signal used was a sinusoidal wave with 1.5 volts peak-to-peak value and 700 Hz in frequency from a function generator (Wavetek, Model 19). Similar results, which is shown in Figure 5.7, as those using DC measurements were obtained.

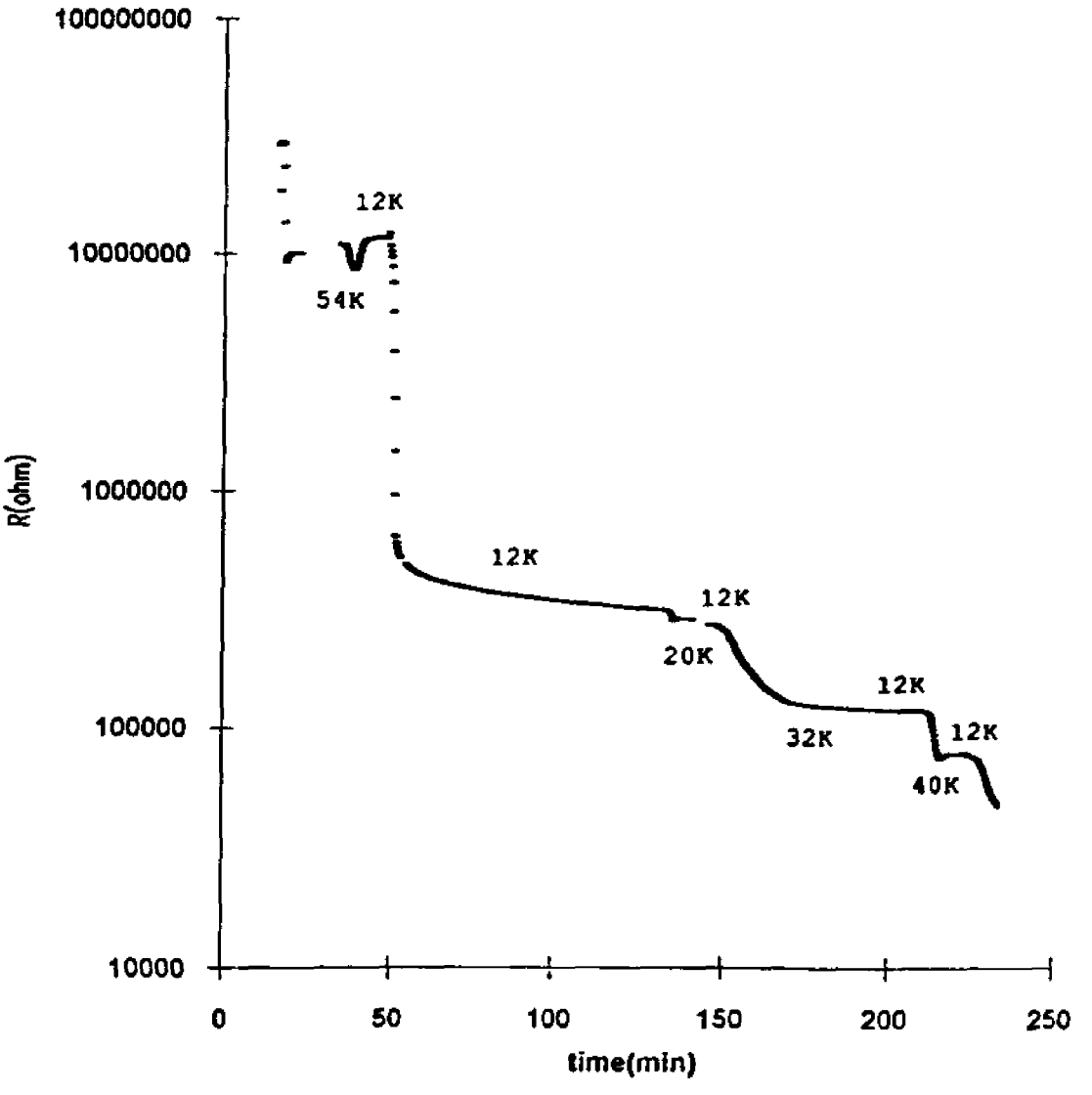

Figure 5.7. The time evolution of ammonia condensed on granular potassium film using AC measurement. From 20 to 45 minute, the potassium film was annealed. The ammonia was introduced into the chamber at t = 45 minute. From 54 to 130 minute, the sample was held at 12 K. Then the sample was cycled between 20 to 12 K, 32 to 12 K and 40 to 12 K.

5.3. Photoemission Study of Ammonia-Potassium System

5.3.1. Experimental details

The work function measurement was conducted using a differentially pumped helium resonance lamp, which supplies photons at fixed energies of HeI (21.2 eV) and HeII (40.8 eV). The HeI emission is always much stronger than that of the HeII. The lamp was operated at 1 kV and 50 - 70 mA. The photoelectrons were analyzed by a PHI double pass CMA, which was operated at a pass energy of 15 eV. The sample was biased at -6 V relative to the ground to get a clear secondary electrons cutoff.

The rest of the photoelectron spectroscopy was conducted using monochromatic synchrotron radiation at the National Synchrotron Light Source (Beam line U7a) in a ultrahigh vacuum system equipped with a hemispherical photoelectron analyzer. The spectra were collected at a pass energy of 22 eV. The ambient pressure in the experimental chamber was 1 x 10^{-10} Torr and reached the mid 10^{-10} range during potassium evaporation. Silver films were deposited onto the liquid helium cooled copper cold finger first. Then, Potassium films, which were thick enough to suppress any

photoelectron features from silver, was deposited onto the sample holder. Ammonia was introduced into the chamber after the characterization of potassium film.

5.3.2. Work Function Change of Ammonia-Potassium System

When ammonia molecules were condensed onto the alkali metal surface, the work function of the sample changed accordingly [5.9, 5.10]. The work function of the sample could be measured using the photoemission technique if the energy of the monochromatic incident photon beam was known and was 21.2 eV in this case, the difference between the photon energy and the energy span of the photoelectron spectrum determines the work function. Figure 5.8 (a) shows the work function changes after condensing ammonia onto a potassium film at 13 K. The work function of the sample decreased by about 0.7 eV. The reduction of the work function could be explained by the electrostatic effect according to Bagus and his co-workers [5.11 - 5.13]. When the first layer of ammonia is condensed on the metal surface, the ammonia bonds with the nitrogen end of the molecule nearest the

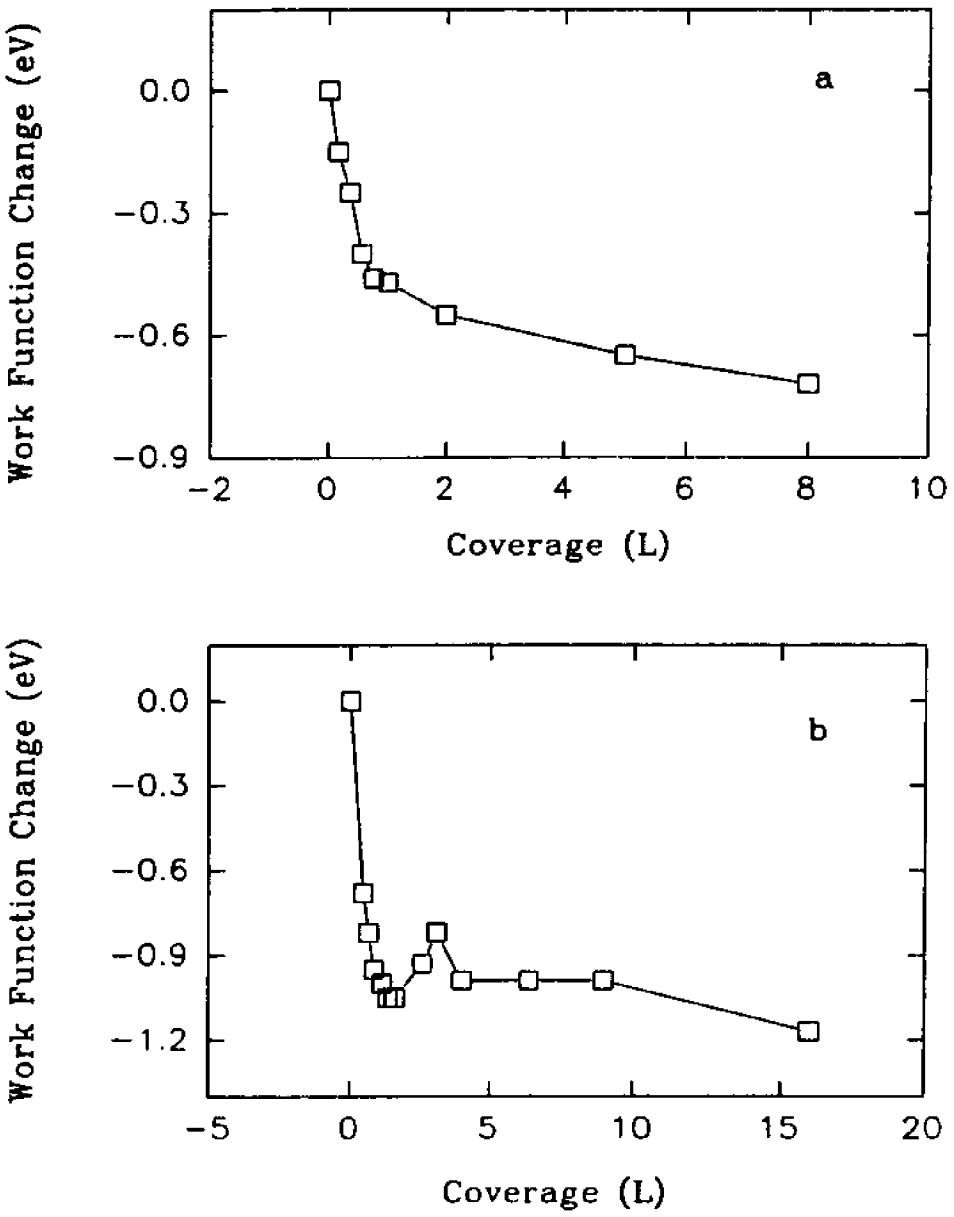

Figure 5.8. Work function change of potassium film after different amount of exposure of ammonia at different temperatures: (a) 13 K, (b) 45 K.

surface and its C_{3v} symmetry axis normal to the surface [5.14 - 5.21]. The bonding is mostly electrostatic in nature, involving the permanent dipole of ammonia and an induced dipole in the surface; actual charge donation from the nitrogen lone pair is of lesser importance.

Figure 5.8 (b) shows the work function change after condensing ammonia onto the potassium surface at 45 K. While the ammonia exposure was less than 2 L, the work function decreased with increasing ammonia exposure. The change of the work function at 45 K was larger than that at 13 K, given the same amount of ammonia exposure. This might be due to the fact that at higher temperatures ammonia molecules had more energy to move around and were well oriented. As more ammonia was condensed, the work function went up and peaked at about 4 L of ammonia exposure, then flattened off. According to the solvation model discussed in detail in section 5.4.1, electrons can tunnel into the ammonia media as long as there are "cavities" to accommodate the tunnelling electrons. When the sample temperature was very low (e.g. 13 K), the number of the tunneled electrons was too small to be seen by the photoemission technique. When the ammonia exposure was low, there were not enough ammonia molecules available to form the "cavities" [5.22], even though ammonia molecules had enough

energy to move around. Increasing the ammonia exposure after that point, enough electrons could tunnel into the ammonia media for the work function to increase again. The work function increase would stop at a point, where the maximum local electric field had been built up and any increase of the electric field would pull the cations into the ammonia. When this happens, the work function of the sample might decrease slightly and then flatten off due to the limited solubility of potassium in ammonia at low temperatures. If the experiment is done at higher temperatures, this detailed process may not be seen because the sample will reach equilibrium quickly due to the higher dissolving rate.

5.3.3. PES Study of Ammonia-Potassium System

Figure 5.9 shows a series of valence band photoemission spectra of 3 L ammonia condensed on a thick potassium film for different temperatures, taken at 200 eV incident photon energy. The potassium film was thick enough to suppress any signal from the silver-coated copper sample holder. The spectrum of the clean potassium film (Figure 5.9, curve a)

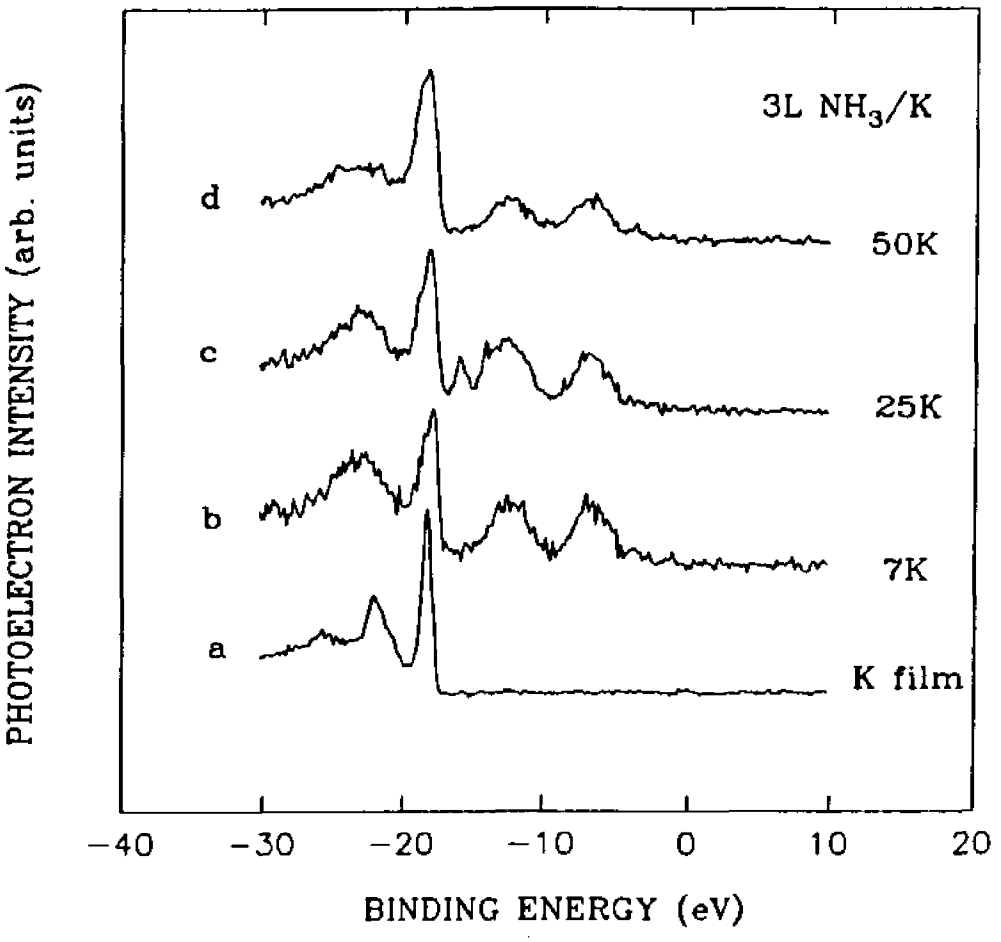

Figure 5.9. Valence band photoemission spectra of 3 L ammonia condensed on potassium film taken at hυ = 200 eV for different temperatures.

shows a sharp peak at 18.3 eV binding energy which is the K 3p peak. The FWHM of this peak is estimated to be 0.9 eV without the corrections for instrumental broadening. Another small peak at 22 eV binding energy and the small shoulder at 25.7 eV binding are attributed to the plasmon-loss in the metal. Both the 18.3 eV binding energy of K 3p and the 3.7 eV plasmon-loss energy are in good agreement with previously published data [5.23].

When ammonia is condensed onto a polycrystalline potassium film (Figure 5.9, curve b), the electronic structure of the potassium surface changes. Admission of 3 L of ammonia led to the disappearance of the plasmon-loss features. The intensity of the K 3p peak also weakened. The new peaks showed up at 23.2 eV, 12.3 eV and 7.2 eV binding energy are features associated with the molecular orbitals of ammonia [5.24], and are assigned to $2a_1$, 1e and $3a_1$, respectively. The $3a_1$ orbital corresponds to the molecular orbital for the lone pair electrons and the 1e orbital corresponds to the molecular orbital for the valence electrons of the N-H σ bond of ammonia [5.25].

When the sample was warmed up from 7 K to 25 K, a new peak showed up at 16.1 eV binding energy (Figure 5.9, curve

c). The binding energy of the new feature is close to that of the physisorbed CO 4σ orbital [5.26] when the appropriate work function is added. To make sure this peak is not from CO contamination, oxygen 1s and carbon 1s core level spectra were taken. There were no peaks above the background level. Because the binding energy of the molecular nitrogen 4σ orbital also appears in that neighborhood [5.26], there is a great chance that the new peak might come from molecular nitrogen. The results of N 1s core level spectroscopy and NEXAFS support this interpretation. We will discuss these experimental results in detail later.

As the sample temperature increased to 50 K (Figure 5.9, curve d), the new feature which showed up at 25 K disappeared. Although the low binding energy side of K 3p peak showed no sign of change, but the high binding energy side broadened significantly. The FWHM of the potassium 3p peak at 50 K was 1.6 eV, which is an increase of 12% compared to that at 7 K (Figure 5.9, curve b). The peak shape was asymmetric, indicating that some charge transferred out of the neutral potassium atoms or a small change in the oxidation state of potassium occurred. Compared to the peaks associated with the ammonia molecule, the relative intensity of the potassium 3p peak also increased.

In Figure 5.10, the energy distribution curves (EDCs) for the potassium 2p core level are shown. The clean potassium film (Figure 5.10, curve a) shows peaks at 294.5 eV and 297.5 eV binding energy which are associated with the K $2p_{3/2}$ and K $2p_{1/2}$, respectively. The broad feature at 301 eV binding energy is the plasmon loss peak, which disappeared after admission of 3 L of ammonia at 7 K (Figure 5.10, curve b). When the sample was warmed up to 25 K (Figure 5.10, curve c), no visible change occurred. As the sample temperature was increased to 50 K (Figure 5.10, curve d), the peaks associated with the K 2p core level shifted by 0.7 eV to higher binding energy. The shift of the K 2p lines indicates that potassium was removed from the metal surface and reacted with ammonia.

Figure 5.11 shows the N 1s core level spectra changes with temperature. The introduction of 3 L of ammonia onto the potassium film at 7 K gives a nitrogen 1s core level peak at 402.5 eV binding energy (Figure 5.11, curve a). When the sample is warmed up to 25 K (Figure 5.11, curve b), a new peak appears at 408.4 eV binding energy. The binding energy of this new peak is very close to the binding energy of solid molecular nitrogen condensed on potassium film (Figure 5.11,

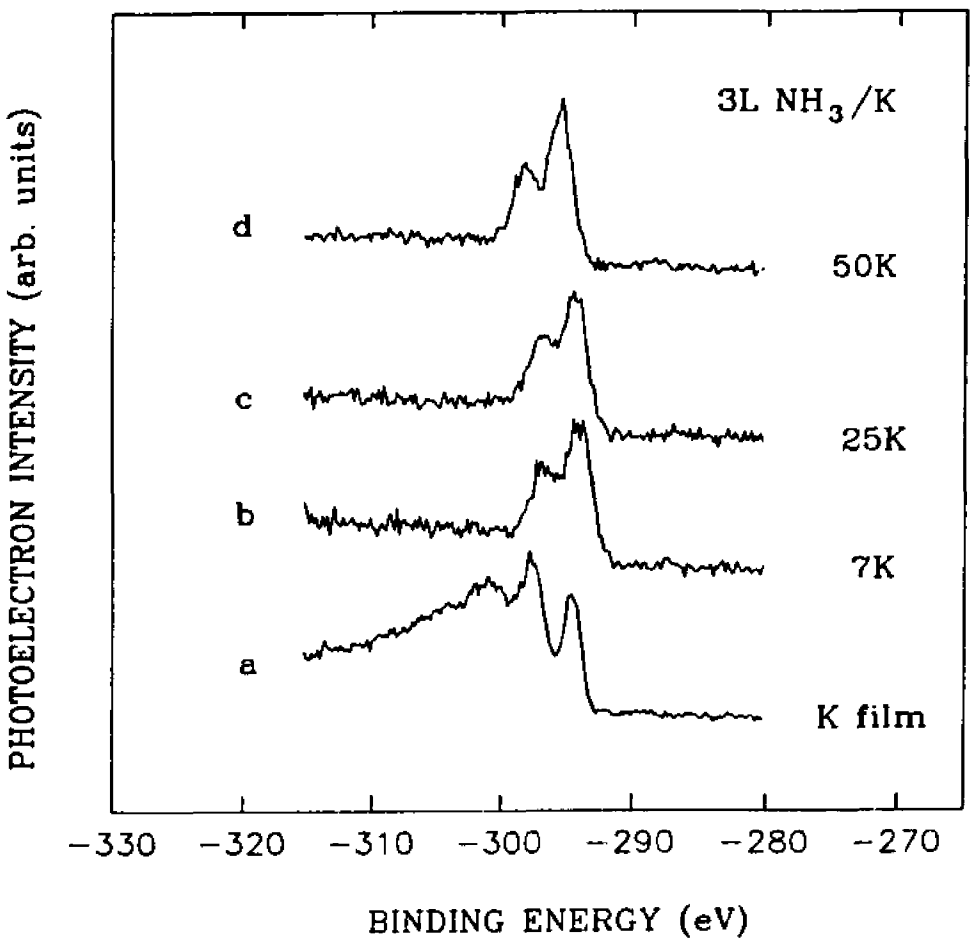

Figure 5.10. The K 2p core level spectra of 3 L ammonia condensed on potassium film taken at hυ = 400 eV for different temperatures.

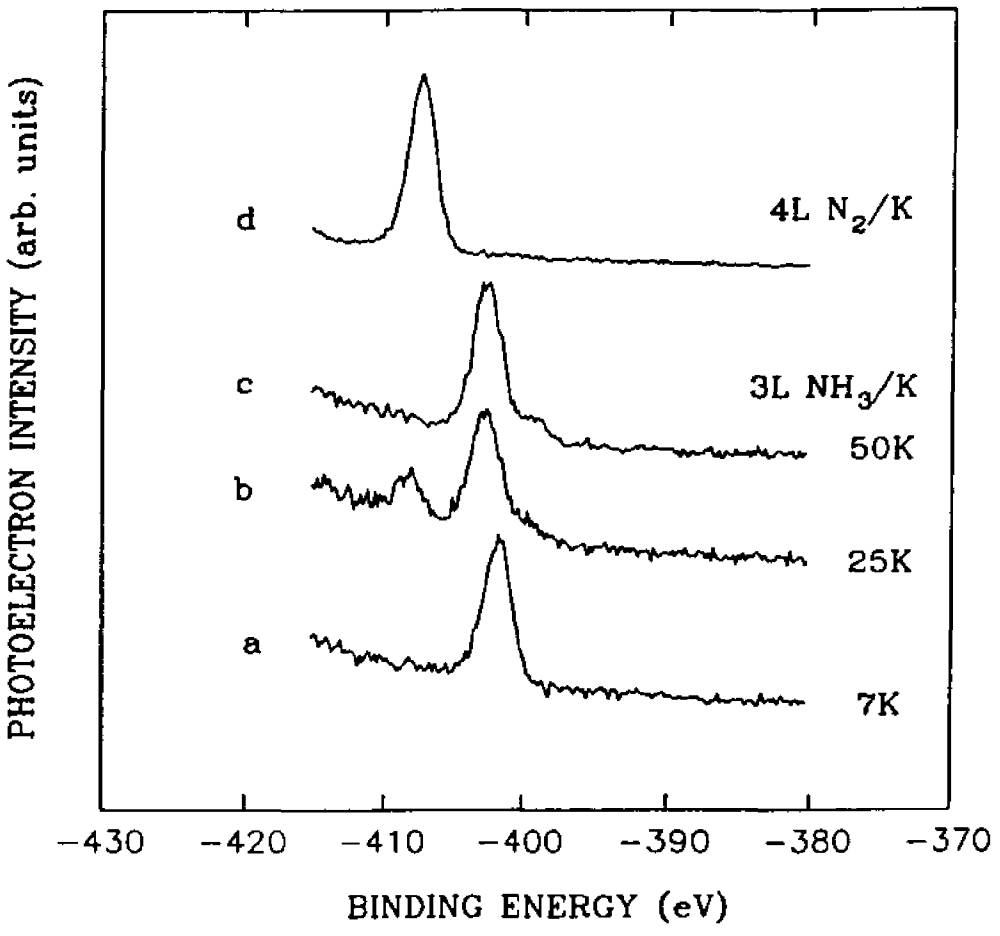

Figure 5.11. The N 1s core level spectra of 3 L ammonia condensed on potassium film taken at hυ = 450 eV for different temperatures.

curve d). This is a further proof of the molecular nitrogen formation. The new peak might also be a intermediate state of the ammonia decomposition process. The fact that the binding energy of N 1s orbital of this new peak is higher than that of ammonia left us hydrazine (N_2H_4) as another candidate, because the binding energies of N 1s orbital of NH_2, NH and atomic nitrogen are smaller than that of ammonia. The result of NEXAFS discussed in the following section excluded the hydrazine possibility. There is also a small shoulder at 399 eV binding energy. As the sample temperature increases to 50 K (Figure 5.11, curve c), the peak at 408.4 eV binding energy disappears. This is consistent with the molecular nitrogen assignment because the vapor pressure of molecular nitrogen at 50 K is more than 1 Torr. The intensity of the weak feature at 399 eV binding energy increases as the sample temperature rises. This peak could be from the ammonia molecules which polarize around the solvated electrons or the fragments of ammonia molecule, such as NH_2 or NH.

The partial dissociation of ammonia molecules on iron surfaces at 160 K [5.27] and tungsten surfaces at 200 K [5.28, 5.29] has been observed. The chemistry of nitrogen hydrides on metal surfaces presents many interesting aspects

and raises many questions which remain to be answered. To date, there is no comprehensive understanding of the role of metal catalysts in the ammonia decomposition process. In our experiment, the decomposition of ammonia appears at very low temperatures. The fact that ammonia decomposes more easily in the ammonia-potassium system than at the ammonia-transition metal interface makes sense if we assume the intuitive picture of electrostatic forces weakening the bonding in the ammonia molecule. Due to the solvation process discussed before, an ammonia molecule in the potassium-ammonia system is attacked by the solvated electrons and cations from both the hydrogen and nitrogen sides of the N-H bond. At the ammonia-transition metal interface, only the nitrogen side of the N-H bond can interact with the metal surface [5.30, 5.31]. This difference may lower the activation energy barrier for the decomposition of ammonia in the ammonia-potassium system. Due to the Boltzmann distribution, there are still many ammonia molecules which have enough energy to overcome this small activation energy at low temperatures.

The synthesis reaction of ammonia is exothermic and is accompanied by a decrease in volume.

$$N_{2(g)} + 3H_{2(g)} \rightarrow 2NH_{3(g)} \qquad (5.6)$$

Chemical reactions can proceed towards both forward and

reverse directions depending on the reaction conditions. Therefore, on thermodynamic grounds, the highest concentration of ammonia in the product gas is obtained at high pressures and low temperatures. On the other hand, sufficient high temperatures are necessary to achieve high reaction rates. In the UHV experimental environment, small amount of ammonia dissociation is possible even at low temperature, because hydrogen could not be condensed on the sample around 20 K. So the reaction (5.1) has the tendency to proceed along the reverse direction in UHV chamber.

5.3.4. NEXAFS Study of Ammonia-Potassium System

Before I discuss the NEXAFS of the ammonia-potassium system, I will discuss the NEXAFS of solid nitrogen and ammonia condensed on potassium films. The ground electronic state of the nitrogen molecule has the electron configuration of $(1\sigma_g)^2(1\sigma_u)^2(2\sigma_g)^2(2\sigma_u)^2(1\pi_u)^4(3\sigma_g)^2$. Transitions involving the promotion of a 1s electron to $1\pi_u$ and np Rydberg orbitals are electric dipole allowed. Figure 5.12, curve a is the total electron yield NEXAFS spectrum of 10 L of nitrogen condensed on potassium at 7 K. The strong

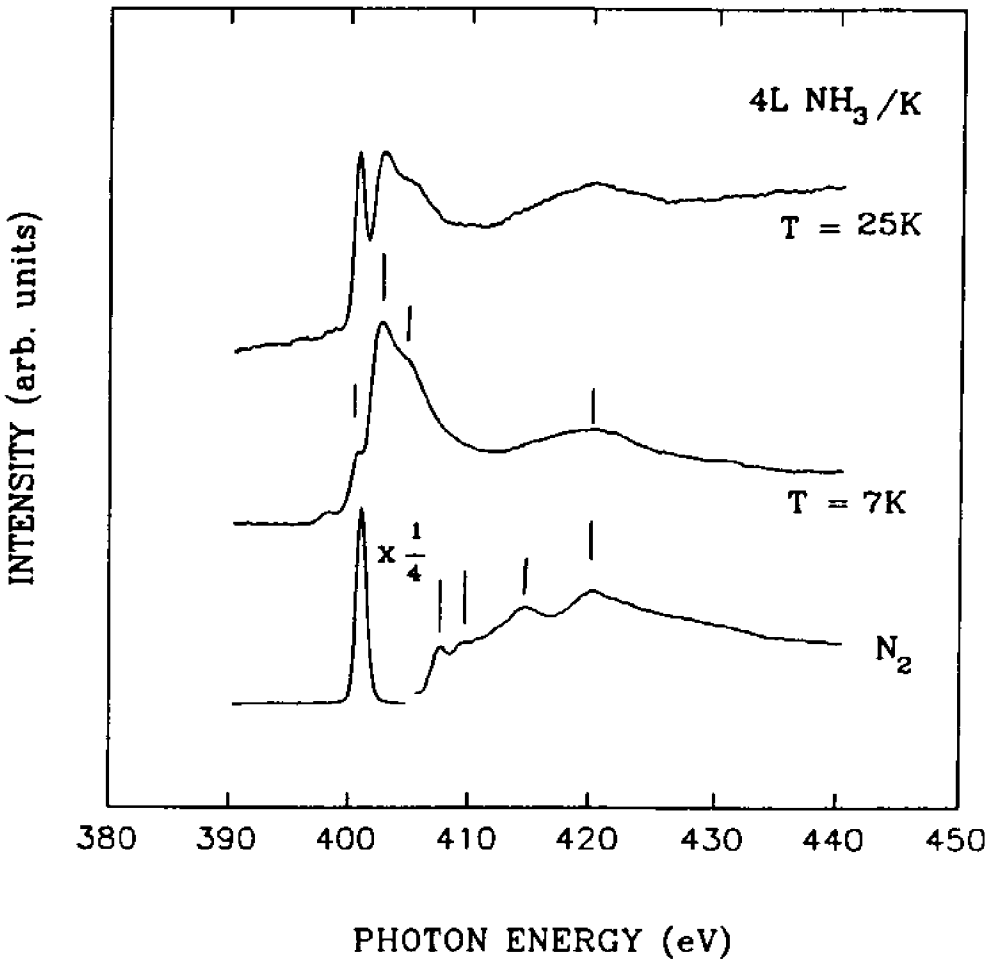

Figure 5.12. The N 1s K-edge NEXAFS spectra of 3 L ammonia condensed on potassium film for different temperatures.

absorption peak at 401 eV is due to the transition from the N 1s core level to the unoccupied $1\pi_g$ molecular orbital. The FWHM of this peak is 1 eV. The small peaks around 407.3 eV and 409.1 eV are Rydberg resonances which in general can be identified by their separation from the ionization potential [5.32, 5.33]. The structure near 414.5 eV is a multi-electron excitation feature [5.34 - 5.37]. The broad peak at 419.7 eV is assigned to the transition of the 1s electron to the N-N σ_u^* antibonding orbital [5.32].

The ammonia molecule has pyramidal geometry in it's ground electronic state. The electron configuration of the ground electronic state of ammonia in C_{3v} symmetry is $(1a_1)^2(2a_1)^2(1e)^4(3a_1)^2$, $^1A_1$. There is a convention that states of molecules are denoted with capital letters and orbitals with small letters. The $1a_1$ molecular orbital is formed from the nitrogen 1s atomic orbital. Promotion of a $1a_1$ electron to nsa_1, npe and npa_1 Rydberg orbitals is electric dipole allowed.

The nitrogen K-edge absorption spectrum of 4 L of ammonia condensed onto a potassium film at 7 K is shown in Figure 5.12, curve b. The photon energy scale was calibrated by comparing our experimental data with previously reported data for gas phase NH_3 [5.31] and N_2 [5.32]. The peak at

400.7 eV photon energy has been assigned to the excitation of one electron from $1a_1$ to $3sa_1$. The peak observed at 402.5 eV is assigned to the promotion of a $1a_1$ electron to the lowest energy 3p Rydberg orbital (3pe). This peak lies 0.3 eV higher in photon energy than the energy loss peak due to $1a_1$ to 3pe Rydberg transition in the gas phase. This shift is likely due to the modification of the higher Rydberg orbitals in solid ammonia, due to the interaction between nitrogen atoms and hydrogen atoms from different ammonia molecules, as discussed by Rosenberg *et al.* [5.38] for H_2O. Another possible cause for the shift is due to dielectric constant effect, as suggested by Chen *et al.* [5.39]. Because molecules are highly polarizable in the solid state, condensed molecules have larger dielectric constants than those in the gas phase. Since the separation between the vacuum level and Rydberg states is inversely proportional to the dielectric constant, the large dielectric constant in the solid will tend to shift Rydberg states closer to the vacuum level than in the gas phase. The shoulder around 404.7 eV consists of different weak peaks associated with transitions to $3pa_1$, 3d, $4sa_1$ and 4pe Rydberg orbitals [5.31]. The energy difference between any adjacent orbital is estimated to be less than 0.6 eV

[5.40, 5.41], which is marginal for the resolution of our monochromator (0.5 eV at $h\upsilon$ = 400 eV) [5.42]. The broad structure around 419.8 eV is identified with the simultaneous transitions of a K-shell and valence shell electrons.

As the sample temperature was increased to 25 K (Figure 5.12, curve c), a sharp peak shows up at 400.8 eV, while the other ammonia related peaks remain unchanged. The position and shape of the peak at 400.8 eV are similar to that of the molecular nitrogen (Figure 5.12, curve a), which strongly suggests that molecular nitrogen is being formed. The characteristic of major leading peak of hydrazine would show up at 402.6 eV photon energy, followed by a broad peak [5.43], which was not shown up in our experiment. When the sample was warmed up to 35 K, the peak at 400.8 eV disappeared and the spectrum resumed ammonia character. Desorption of solid nitrogen molecule is expected to occur about 30 K because the vapor pressure of the nitrogen molecule is above 10^{-5} Torr.

In summary, the NEXAFS spectrum suggests that the new feature, which showed up around 25 K, was from molecular nitrogen and not from hydrazine. This is consistent with the photoemission results discussed in the last sections. Energetic photon beam can break the N-H bonds of ammonia

molecule. The result of controlled experiment showed that the contribution from direct photon beam was small in our experiments. The decomposition of ammonia at very low temperatures must be due quantum chemical reactions.

5.4. A Discussions of Possible Models

5.4.1. Solvation Model

The slow change of film resistance with time in figures 5.1 and 5.2 might be caused by slow chemical reactions between the potassium clusters and the ammonia matrix. In the solutions of alkali metals in liquid ammonia, it is generally believed that alkali metals can dissolve into the ammonia and the solvated electrons and alkali metal cations are "dressed" by the polarization of the ammonia media separately. Jortner [5.44] proposed that the solvated electron is localized in a cavity formed in the ammonia media, the radius of the cavity is about 3 Å. The binding energy of the ground state of solvated electron is -2.160 eV, the binding energy of the first exited state is -1.306 eV. The calculated binding energy of the solvated electron agrees reasonably with the

experimental results [5.45]. The work function of potassium film is about 2.2 eV [5.46]. By condensing one layer of ammonia, the work function could decrease by 0.5 eV due to the permanent dipole moment of ammonia molecule (see section 5.3.2 for details). Electrons near the Fermi level of potassium film have the tendency to move into the low energy state in cavities in the ammonia media. The energy diagram is shown in figure 5.13. Qiu [5.47] and his co-workers did photoemission studies of sodium on solid ammonia at liquid nitrogen temperature. They found that sodium can dissolve into solid ammonia at that temperature and there was a time dependance of the dissolving process. Based on the above argument, we use the following model to explain our experimental results. In order to form the cavities which are necessary to accommodate the solvated electron, ammonia molecules must have some minimum rotational energy. At the lowest temperature in our experiment (14 K in this particular trial), very few molecules had enough energy to move around to form the cavity to host the tunneling electron. When the electron tunneled into the ammonia media, it was localized due to the very low temperatures. A strong electric field could be developed between the tunneled electrons and potassium cations. When the local electric field becomes

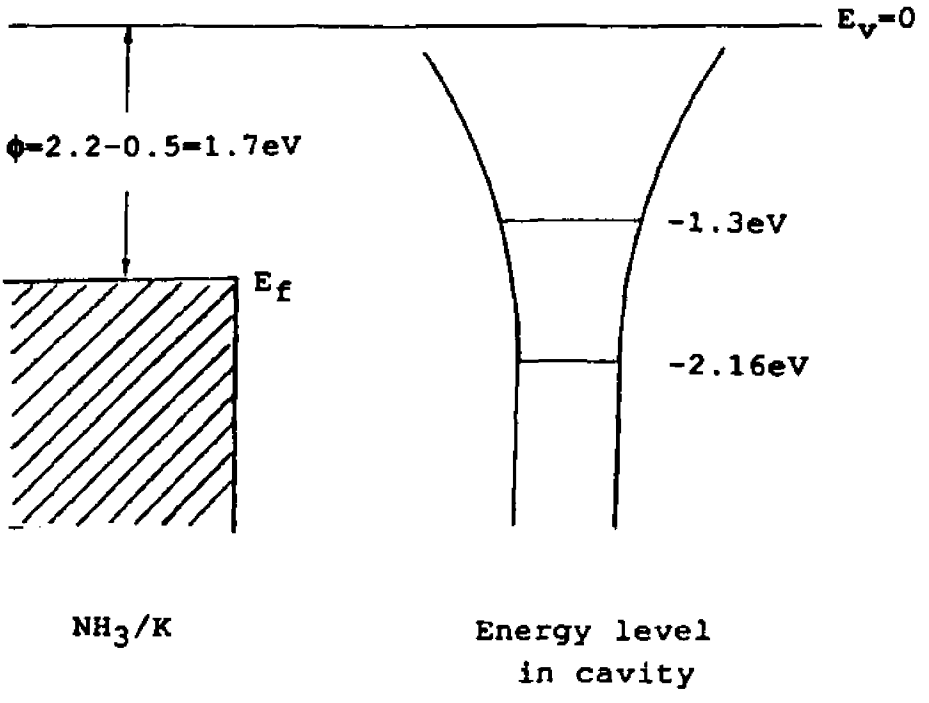

Figure 5.13. Schematic energy diagram for ammonia-potassium system.

strong enough, the cation on the potassium cluster could be pulled off and dissolved into the ammonia media. In this way, the effective radius of the potassium cluster increased and the film resistance decreased slowly with time. As the concentration of solvated ions increased, there is increasing chance for them to capture electrons and become neutral atoms again. This is another possible contribution to the increase of the effective radius of potassium cluster.

The aforementioned model, which we used to explain the low temperature solvation process for ammonia-potassium system, is similar to the model Mott proposed to interpret the formation of protective oxide films on metals [5.48, 5.49]. He assumed that the solubility of metal ions in the oxide is at the temperature considered too small for any passage of metal by diffusion and the work function is small enough to allow the thermionic emission of electrons from the metal into the conduction levels of the oxide. If, then, oxygen is adsorbed on to the surface of the oxide and oxide ions are formed, a strong electric field will be set up in the oxide. The electrostatic force across the oxide is the driving force for the growth of the protective oxide film. As the thickness of the oxide film increases, the static electric field becomes weaker and weaker. At certain point,

it can not pull the ions through the oxide layer, then the growth of the oxide film stops. In our experiments, where the sample temperature was around 10 K, the thermionic emission is impossible even if the corresponding work function is about 1 eV. Then, the only possible mechanism for electron transfer at such a low temperature is the quantum mechanical tunneling effect. This can be demonstrated by a simple calculation. The energy of a particle which tunnels must be the same on both sides of the barrier (for otherwise, radiation will occur). From the energy conservation requirement, we have

$$p_1^2/2m + U_1 = p_2^2/2m + U_2 \qquad (5.7)$$

where p_1 and p_2 are the momenta of the electrons inside the metal and inside the ammonia media, respectively; U_1 is the potential energy of the electron inside the metal and U_2 that of the electron in the ammonia media. For a rough estimate, we can assume that $U_2 = 0$ and $U_1 = \phi$, the work function of the metal. P_1 is the momentum of electrons in the Fermi level and $P_1^2/2m$ ~ kinetic energy ~ the Fermi energy of an electron in the metal. But the Fermi energy of an electron differs from its work function only by the surface potential, which is much less than the work function. Hence

$$p_1^2 \sim 2m\phi \qquad (5.8)$$

Then, the de Broglie wavelength

$$\lambda_e = h/p = h/(p_1^2 + 2m\phi)^{1/2} = h/(4m\phi)^{1/2} \qquad (5.9)$$

Taking ϕ as some 3 eV, then

$$\lambda \sim 10^{-3} \text{ cm} \qquad (5.10)$$

Usually, as a rule of thumb, if the happenings described concern motions much larger than their de Broglie wavelengths, the treatment can be approximated by classical mechanics. However, at the ammonia-potassium interface, the distance over which an electron jumps is of the order of a few angstroms. Comparing to the calculated value of 10^{-3} cm, the transition with which one is associated in an interfacial electron transfer is much less than the length of the relevant de Broglie wave. The transitions must be treated according to quantum theory.

5.4.2. Reaction Model

An alternative explanation for the decomposition of ammonia and the formation of molecular nitrogen at low temperatures can be obtained by the combination of the solvation model and the results of Kirschke and Jolly [5.50]. These authors show that ammonia decomposition reactions are

reversible under their experimental conditions, in which the hydrogen partial pressure in the experimental chamber was kept higher than 7600 Torr. They also showed that the solvated electron can exist in equilibrium with elemental hydrogen and the amide ion. According to them, solution of alkali metals in liquid ammonia decomposes slowly to form metal amides and hydrogen. For potassium, the reaction may be written as

$$e_s^- + NH_3 = NH_2^- + 0.5\ H_2 \qquad (5.11)$$

At low temperatures, due to the lower mobilities of ions and solubility of KNH_2, the following reaction may also happen

$$K^+ + e_s^- + NH_3 = KNH_2 + 0.5\ H_2 \qquad (5.12)$$

Both of the reactions would proceed along the forward direction (the direction for which ammonia is decomposed) under the ultrahigh vacuum and low temperatures, e.g., 6 - 100 K, which are too high for condensing hydrogen molecules and yet low enough to condense multilayers of ammonia. Under these conditions, the reaction product hydrogen is removed from the surface and the reaction favors the forward direction. The NH_2^- is not a stable compound, it would continue to decompose forming molecular nitrogen and hydrogen or capture an potassium ion forming substable compound KNH_2.

A more detailed mechanism of ammonia synthesis and decomposition has been proposed to consist of the following elementary steps [5.51]

$$NH_{3,s} = NH_{2,s} + H_s \quad (5.13)$$

$$NH_{2,s} = NH_s + H_s \quad (5.14)$$

$$NH_s = N_s + H_s \quad (5.15)$$

$$2H_s = H_{2,s} = H_{2,g} \quad (5.16)$$

$$2N_s = N_{2,s} = N_{2,g} \quad (5.17)$$

where the subscript s and g indicate that the particle is sticking on the surface and in the gas phase, respectively. Shustorovich and Bell recently calculated the activation barriers for both forward and reversed reactions comprising elementary steps (5.13) - (5.17) of ammonia synthesis and decomposition on Pt, Ru, Fe and Re surfaces [5.52]. They found that the highest activation barrier for the forward (ammonia decomposition) reaction in steps (5.13) - (5.16) is 25 kcal/mol (~1.08 eV). If the the reactants have enough energy to overcome the activation barriers then the chemical reaction can proceed. The heat of solution of an electron in liquid ammonia is 1.76 eV [5.53, 5.54]. If the activation barrier for ammonia decomposition reaction on the alkali metal clusters has the same order of magnitude as those on the transition metal surfaces, it is possible that some

ammonia molecules could have enough energy to surmount the activation barriers for the ammonia decomposition due to the heat of solution of the solvated electrons and the Boltzmann distribution of energy of ammonia molecules.

More carefully designed experiments were carried out to find the mechanism for the decomposition of ammonia and the irreversible change of film resistance. Figure 5.14 shows resistivity measurement results for condensing different amounts of ammonia onto a lithium film. When a small amount of ammonia (~ 1L) was condensed onto the lithium film at t = 33 min, the film resistance was still reversible as the film was warmed up to 30 K. After more ammonia (~ 8.4L) was condensed on the same film at t = 42 - 47 minute, the film resistance became irreversible as the sample was warmed up to 31 K. Valence band photoemission spectra for small amounts of ammonia condensed on a potassium film also showed no change in the spectra when the sample was gradually warmed up to 30 K which is contrary to the results discussed in section 5.3.3 where significant amount ammonia were condensed onto the potassium film surface. These results prove that the low temperature chemical reactions on alkali metal-ammonia films are not surface chemical reactions and enough ammonia

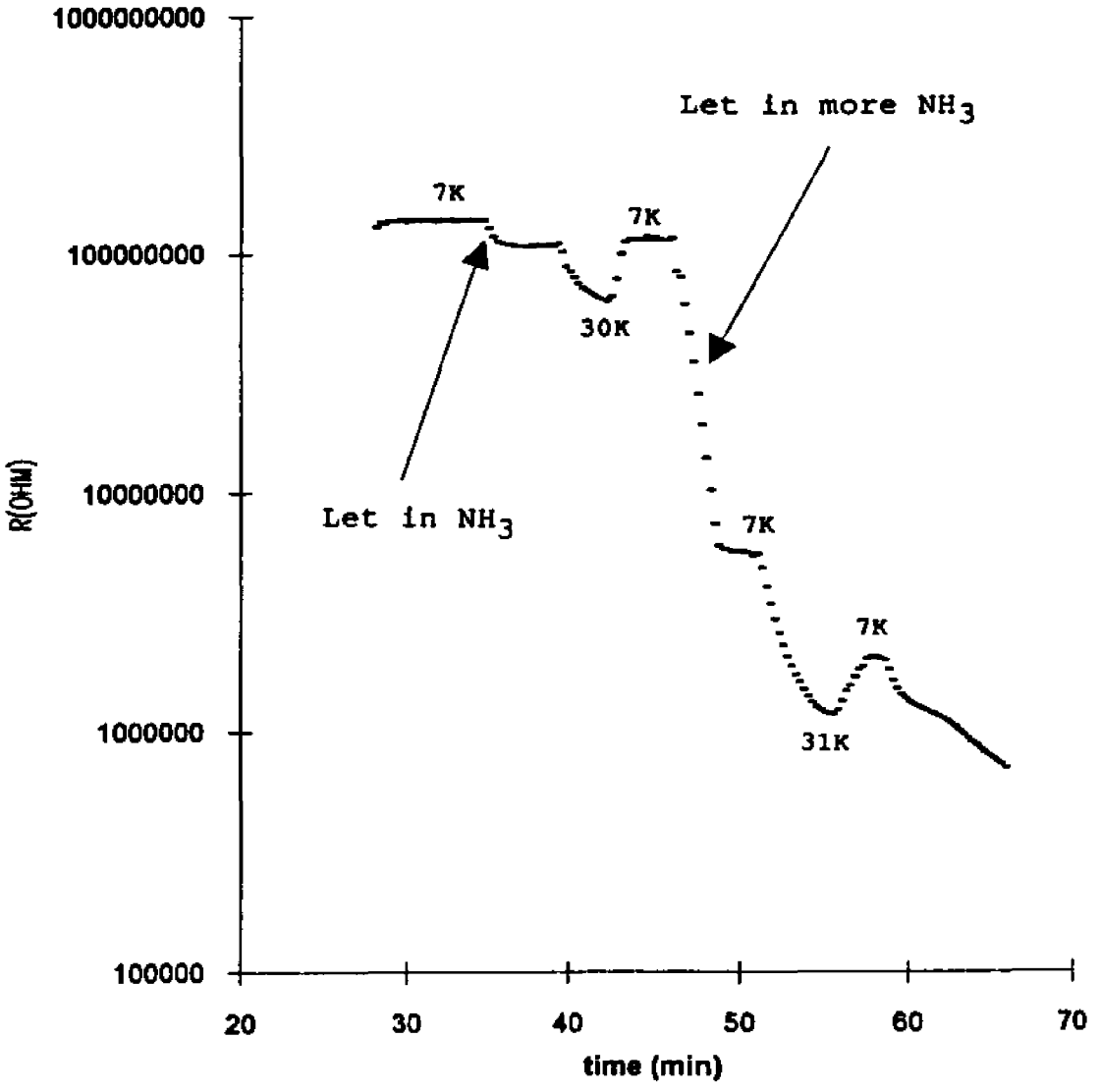

Figure 5.14. The time evolution of different amount of ammonia condensed on a granular lithium film. Small amount of ammonia was introduced into the chamber at t = 33 min, then the film was annealed to 30 K. More ammonia were condensed onto the film at t = 47 min, then the film was annealed to 31 K.

condensed on alkali metal films to accommodate solvated electrons and ions is a prerequisite for the low temperature chemical reaction on alkali metal-ammonia films.

A possible mechanism for low temperature chemical reactions on alkali metal-ammonia films can be summarized as follows. After condensing enough ammonia onto the alkali metal film at low temperatures, electrons can tunnel into the low energy state inside ammonia media. This is the beginning step of all the chemical changes observed in the alkali metal-ammonia films for both resistivity and photoemission measurements. Tunneling is a temperature independent process, but the formation of cavities inside the ammonia media might be a temperature dependent process. This might be the reason why rapid changes appeared in both photoemission and resistivity measurements as sample was warmed up about 25 K. After electron tunneling into the ammonia media, the local electric field is built between tunneled electrons and alkali metal ions left on metal clusters. As more and more electrons tunnel into the ammonia media, the local electric field is getting stronger and finally metal ions are pulled off the metal clusters and dissolved into ammonia media. This is the first stage of the low temperature chemical reaction in

alkali metal-ammonia films. The second stage chemical reaction in this system is very complicated and involves many mechanisms which may contribute to the observed changes in photoemission and resistivity measurements. First, as the concentrations of solvated electrons and ions increase, some of them may recombine together to become neutral atoms and segregate out. This could contribute to the irreversible change of film resistance in the resistivity measurement. Second, as the sample temperature increases, the unstable KNH_2 may decompose to form molecular nitrogen and neutral potassium atoms or potassium ions. The intermediate steps are not clear yet. One possible path is given by equations (5.13) - (5.17). In this case, the subscript s should be interpreted as a site near the solvated electrons or ions. Because solvated electrons and ions are more active than the neutral metal atoms and experimental results showed that the chemical reaction did not occur at alkali metal surfaces. Another possible path is that hydrazine (N_2H_4) forms first and then hydrazine decomposes into molecular nitrogen and hydrogen. Photoemission spectra did not show features related to hydrazine, but they might be buried by the strong peaks from ammonia and nitrogen. Third, the heat of solution of an electron in ammonia may give some ammonia molecules enough

energy to overcome the activation barriers in steps (5.13) - (5.16) and decompose into nitrogen and hydrogen. Fourth, all the charged particles mentioned above could contribute to the rapid change of film resistance to some extent, but this is not the major factor since the film resistance remains low after most ammonia has already left the sample. Also, at low temperatures and weak electrical fields the mobility of the charged particles is very small.

Chapter 6. Photoemission Study of Yb-C_{60} System

The discovery of C_{60} molecule [6.1] and the development of procedures for producing sizable quantities of them [6.2] attracted intense scientific studies. C_{60} is a molecule with 60 carbon atoms arranged in the form of a soccer ball [6.3]. Figure 6.1 is the schematic illustration of a C_{60} molecule. Carbon atoms sit at the vertices of a truncated icosahedron. Pentagonal faces are linked with single bonds. Single and double bonds alternate around a hexagonal face [6.4]. C_{60} is closely related to the geodesic domes invented by R. Buckminster Fuller, which are also icosahedral networks of pentagons and hexagons. It has therefore been named buckminsterfullerene, or buckyball. The recent discovery that in the solid state it can be doped and that it exhibits fascinating electronic properties has greatly intensified the interest in this and related materials. In particular, when doped with alkali metal, fullerene crystals exhibit metallic conduction and superconductivity at unprecedentedly high temperatures for a molecular solid [6.5, 6.6]. It is known that K and Rb react with C_{60} to form compounds of the form A_xC_{60} where $x = 3, 4, 6$ and the A_3C_{60} phase becomes

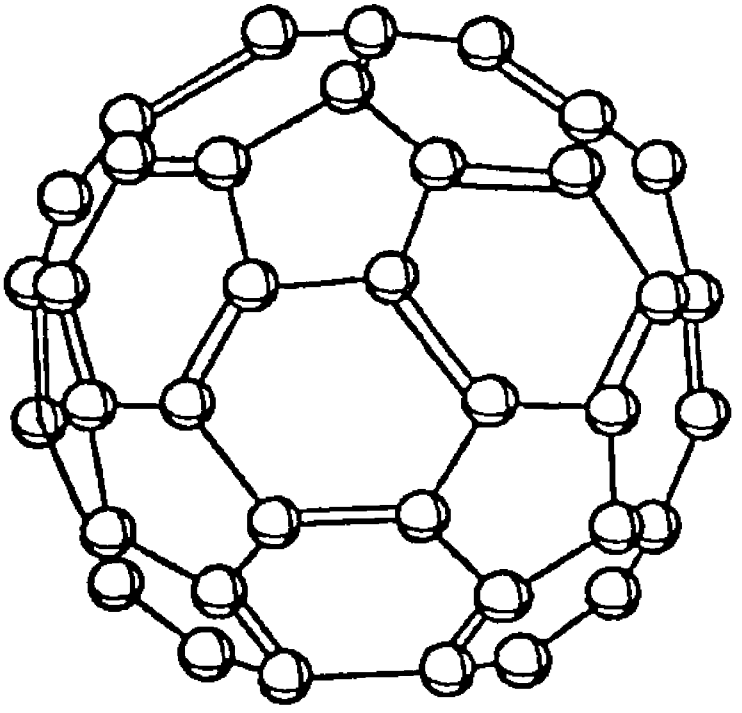

Figure 6.1. Schematic illustration of a C_{60} molecule. Carbon atoms sit at the vertices of a truncated icosahedron. Pentagonal faces are lined with single bonds.

superconducting when cooled [6.7]. Photoelectron spectroscopy and related techniques have shown that the K_3C_{60} phase has a Fermi edge [6.8, 6.9]. Other alkali metal fullerides have been studied and x-ray diffraction has shown that Li and Na produce the A_2C_{60} and A_6C_{60} phases which are not superconducting [6.10]. Alkaline earth and transition metal fullerides also have been made and studied to find other fulleride superconductors and make C_{60} compounds with modified chemical and physical properties [6.11, 6.12]. One such non-alkali metal worth an examination is ytterbium. Ytterbium, like the alkali metals, can be solvated in polar solvents like ammonia and might be an effective electron donor. Possible superconducting behavior in Yb fullerides was reported by Bharathi et al. [6.13]. The transition temperature is relatively low 5.4 K, but its confirmation would be the first demonstration of superconductivity in an electron-doped fulleride that does not contain an alkali or alkaline metal. All the metals , which can form superconducting fullerene compounds so far, can dissolve into liquid ammonia. Europium might also be a promising candidate for the superconducting fullerides.

This chapter presents valence band photoelectron results for ytterbium fullerides formed at the interfaces of

Yb-C_{60} at room temperature. The valence band photoelectron spectra are compared to alkali fullerides and are also compared to the data for Yb in xenon and condensed ammonia. The examination of ytterbium in xenon or ammonia helps to identify whether the Yb-C_{60} phase develops states indicative of a chemical interaction between Yb and C_{60} or whether Yb simply donates charge to fullerene. The data for ytterbium in xenon also provides an example of cluster growth and provides information about how the Yb 4f states change with increasing cluster size. The characteristics of the Yb 4f states are a good indication of the occupancy of the 4f states or the valence of the ytterbium [6.14]. They were examined to determine the Yb valence in C_{60}. We looked at the case where Yb vapor is deposited on a C_{60} film and the opposite case where fullerenes are deposited on a metallic Yb film. Yb-C_{60} phases assembled by vapor deposition have been studied by Ohno et al. [6.15]. They concluded that the Yb-C_{60} phase formed was Yb_2C_{60} and also reported that the formation of this phase on a fullerene film is diffusion limited at 300 K.

Figure 6.2 shows the result of depositing fullerenes on a thick ytterbium film at 300 K. The clean ytterbium film shows the expected surface and bulk Yb 4f peaks and a

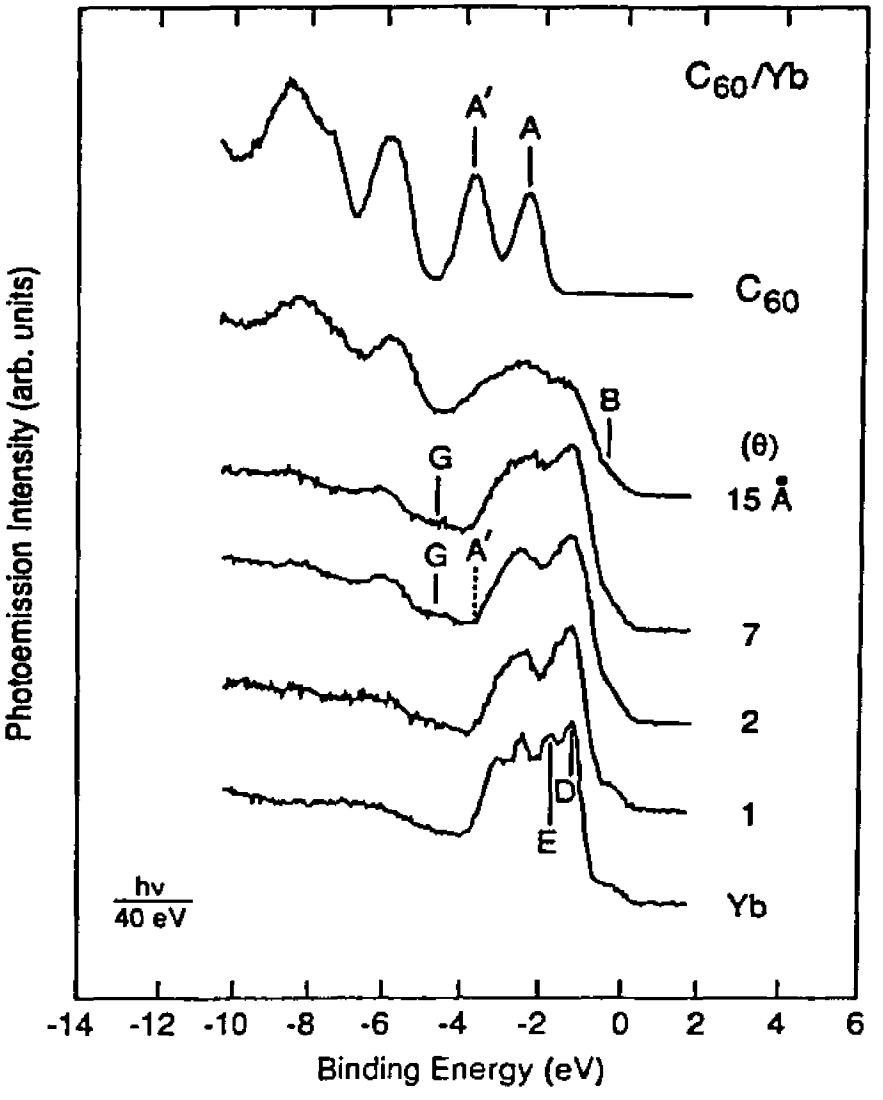

Figure 6.2. Valence band photoelectron spectra for the incremental deposition of C_{60} on Yb.

relatively weak step at the Fermi edge. Deposition of 1 Å of C_{60} decreases the size of the surface 4f peak (peak E). The most intense Yb 4f state is found at the position of the metallic Yb bulk peak (peak D). Further deposition of C_{60} adds broad peaks near -6 and -8 eV which are the σ states of the fullerene. Peaks associated with the π states are weak or merged into the strong Yb 4f features. It took a C_{60} coverage of 15 Å to generate peaks associated with the π states marked A and A', respectively. At 15 Å C_{60} coverage, the states 0.5 to 1 eV below the Fermi level maintain their intensity while the states at Fermi level become weaker. It is not obvious that the surface layer has a Fermi edge at 15 Å C_{60} coverage. The Yb 4f peaks are not readily discriminated in the EDCs for the thicker C_{60} overlayers shown in Figure 18. The Yb 5p core levels do not change their binding energy.

A weak feature marked G is seen for Yb coverages between 2 and 7 Å in Figure 6.2. A weak satellite feature is seen near this energy in photoemission data taken from the Yb vapor. Svensson *et al.* [6.16] identified the feature as a shake-up peak. In other studies of mixed-valent intermetallic Yb compounds [6.17] and studies of Yb on Ni (100) [6.18], strong 4f features are seen in the same vicinity for trivalent Yb which has a hole in the 4f bands. Trivalent Yb

shows 4f features extending from 5 to 15 eV binding energy and the strongest components are near 5 eV binding energy. The $4f^{13}$-$4f^{12}$ features are strong in data taken at XPS energies but relatively weak when compared to the $4f^{14}$-$4f^{13}$ features that give the doublet. If we interpret peak G as the $4f^{13}$-$4f^{12}$ transitions, Yb in C_{60} has a trivalent component.

Figure 6.3 is the valence band photoelectron spectra for the deposition of ytterbium metal vapor onto a thick C_{60} film at room temperature. The lowest curve shows the unmodified fullerene. The data shown for C_{60} is in good agreement with that obtained for C_{60} films by other researchers [6.19, 6.20]. The two peaks (labeled as A and A') are assigned to two orbitals with π orbitals and the orbitals below 4 eV binding energy have mostly σ character. The π orbitals form two concentric shells which encase the sphere containing the carbon atoms and have a node on the carbon containing sphere. The σ orbitals tend to lie on the sphere and are localized on the carbon-carbon bond axes [6.21]. It is obvious that the π states will play a central role in the interactions between Yb and C_{60}.

As small amount of ytterbium (2-4 Å) is deposited on the fullerene surface the fullerene levels broaden and new

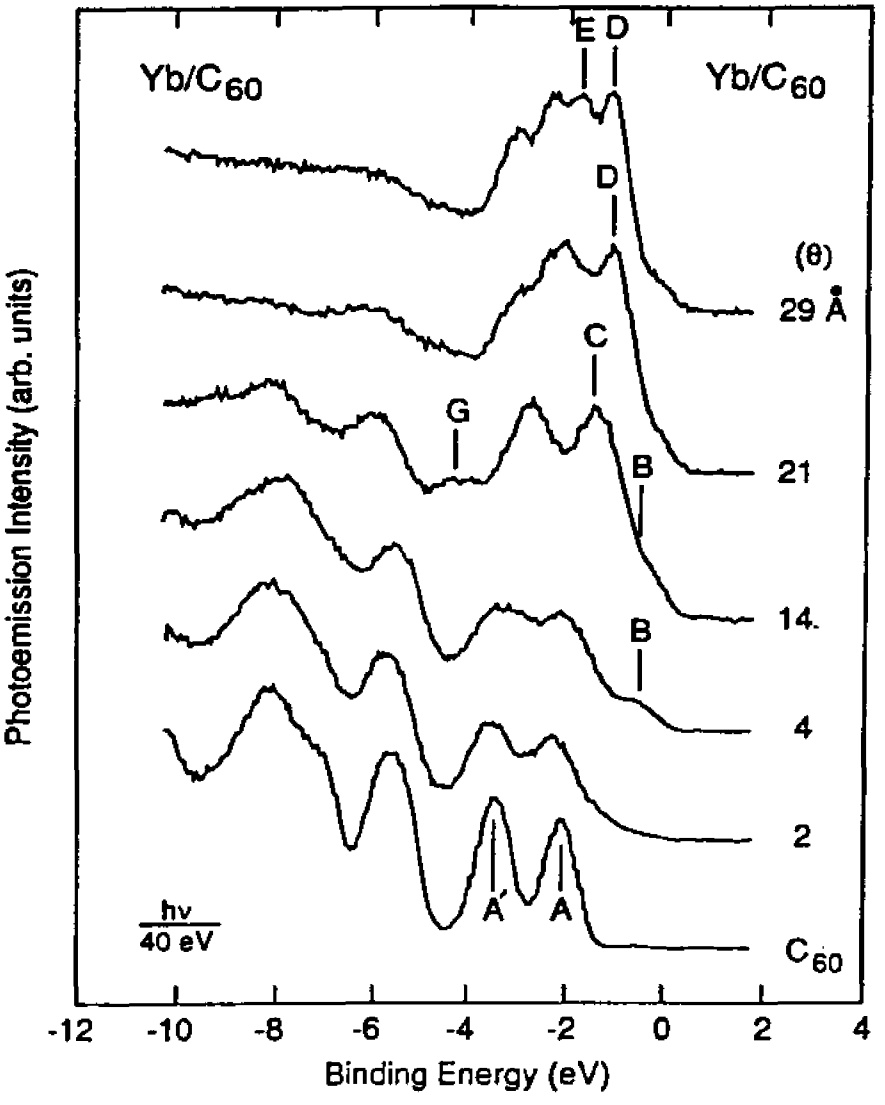

Figure 6.3. Valence band photoelectron spectra for the incremental deposition of ytterbium on a thick fullerene film.

features marked "B" and "C" develop between the lowest binding energy C_{60} peak and the position of the Fermi level as referenced to the tantalum support. Of particular interest is the data for the 14 Å case. In that spectrum, peak "C" is the most intense and a new feature marked "G" is evident. These peaks have no counterpart in the in the pure C_{60} (Figure 6.3, bottom curve) or ytterbium (Figure 6.3, top curve). The peaks appear near the same binding energies as the fullerene induced features on ytterbium and we use the same designations. We argue these peaks are related to the Yb-C_{60} phase being formed by depositing ytterbium in the fullerene matrix. It is likely that peak C is the Yb $4f_{7/2}$ feature because a similar 4f feature is seen in Yb intermetallic compounds in this range of energies. Peak G is identified with the Yb 4f features and is either the shake-up satellite or a feature due to trivalent ytterbium. The feature marked B can be generated by a weak feature coming up about 1.6 eV below the Fermi level. Its origin will be discussed in more detail later.

As more ytterbium is deposited on the surface, the states tentatively attributed to the Yb 4f become more complex. A 21 Å ytterbium coverage was sufficient to induce a

second 4f doublet located about 0.5 eV near the Fermi level. The peak D resembles the bulk ytterbium component in a intermetallic compound like $YbPb_3$ and may be due to a change in the Yb-C_{60} bonding as the concentration of ytterbium increases in the surface layer. It could also be due to the beginning of the phase separation process and the growth of ytterbium clusters. Evidence for the nucleation and growth of a metallic ytterbium phase is seen when the coverage is increased to 29 Å. At this point , the Yb $4f_{7/2}$ splits into two features (peaks E and D) that resemble those seen for the metallic bulk and surface Yb 4f peaks (Figure 6.2, bottom curve).

The binding energy of the shallow Yb 5p core level was obtained to determine whether the ytterbium was ionized like the alkali metals. When compared to metallic ytterbium, little or no core level shift was observed. Clearly, the transfer of charge off the ytterbium site would make the core level move to higher binding energy and this would be expected in the case of ionization. However , the binding energy of the Yb 5p level could be controlled by other changes in the electronic state like localization. We think the Yb 5p levels are sufficiently below the fullerene states to preclude an interaction between them and the valence

states of the C_{60} as was argued by Benning et al. [6.22] to explain the lack of a core level shift of the shallow p core levels of the alkali metals. For Yb_2C_{60}, Ohno et al. [6.15] report that the C 1s core level moves approximately 1 eV to lower binding energy as would be expected for an increase in the electron charge on the fullerene.

The interactions between ytterbium and fullerene are controlled by the growth and nucleation of ytterbium clusters and their electronic interactions with fullerenes. These processes can be studied separately by putting ytterbium in other matrices. The deposition of ytterbium into a rare gas layer provides a case where the condensed gas should not interact with the ytterbium and the evolution of ytterbium clusters with deposition can be studied. The electronic structure of the ytterbium will change when it is deposited into a solid ammonia film at low temperatures. Ammonia molecules are polarizable and have a significant energy gap between the filled and unfilled levels. Those features of solid ammonia resemble the properties of fullerene solid. When ytterbium is deposited in liquid ammonia, it solvates and an electron is removed from the ytterbium. If electrons are removed from ytterbium and donated to the fullerene, it is likely that the ytterbium will have similar electronic

structure. It should be emphasized that the interactions between the ytterbium and ammonia or the fullerene are quite different. For the case of ytterbium in ammonia, the removal of the electron from the metal leads to a situation where the electron does not go on to the molecule but goes into the vacuum between the molecules. The molecules solvate the electron which is negatively charged species. In the case of ytterbium in the fullerene, the electron goes from the metal to the molecule to form a C_{60}^- species or a bond between the metal and the molecule.

Figures 6.4 and 6.5 show the valence band photoelectron spectra for ytterbium in xenon and ammonia matrices, taken by Qiu et al. [6.23]. For ytterbium deposited in xenon, the ytterbium clusters evolve rapidly and develop Yb 4f characteristic features of the bulk and surface components of ytterbium films by a coverage of 1.6×10^{14} atoms/cm^2. This coverage is but a fraction of that needed to grow a monolayer of ytterbium atoms. The spectra for the smallest ytterbium coverage (2.5×10^{13} atoms/cm^2) shows what appears to be a doublet. Atomic ytterbium has a doublet structure for the 4f states. The doublet structure is the expected spectrum for the multiplets generated by the $4f^{14}$ to $4f^{13}$ transition.

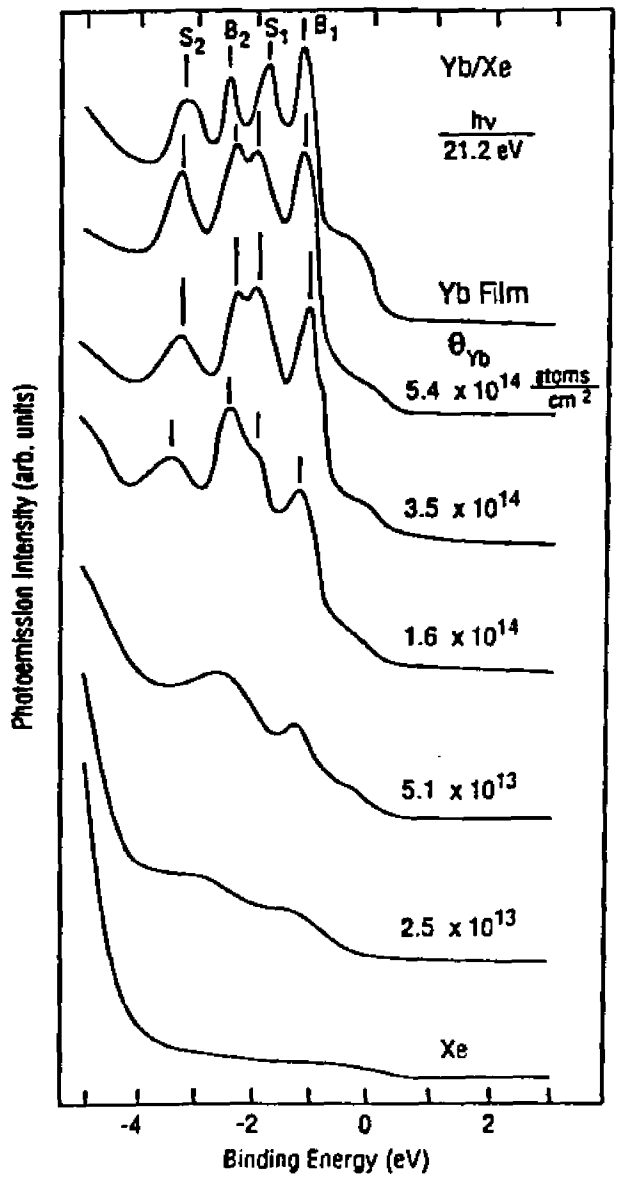

Figure 6.4. Valence band photoelectron spectra for ytterbium deposited on a thick xenon film at 20 K [6.23].

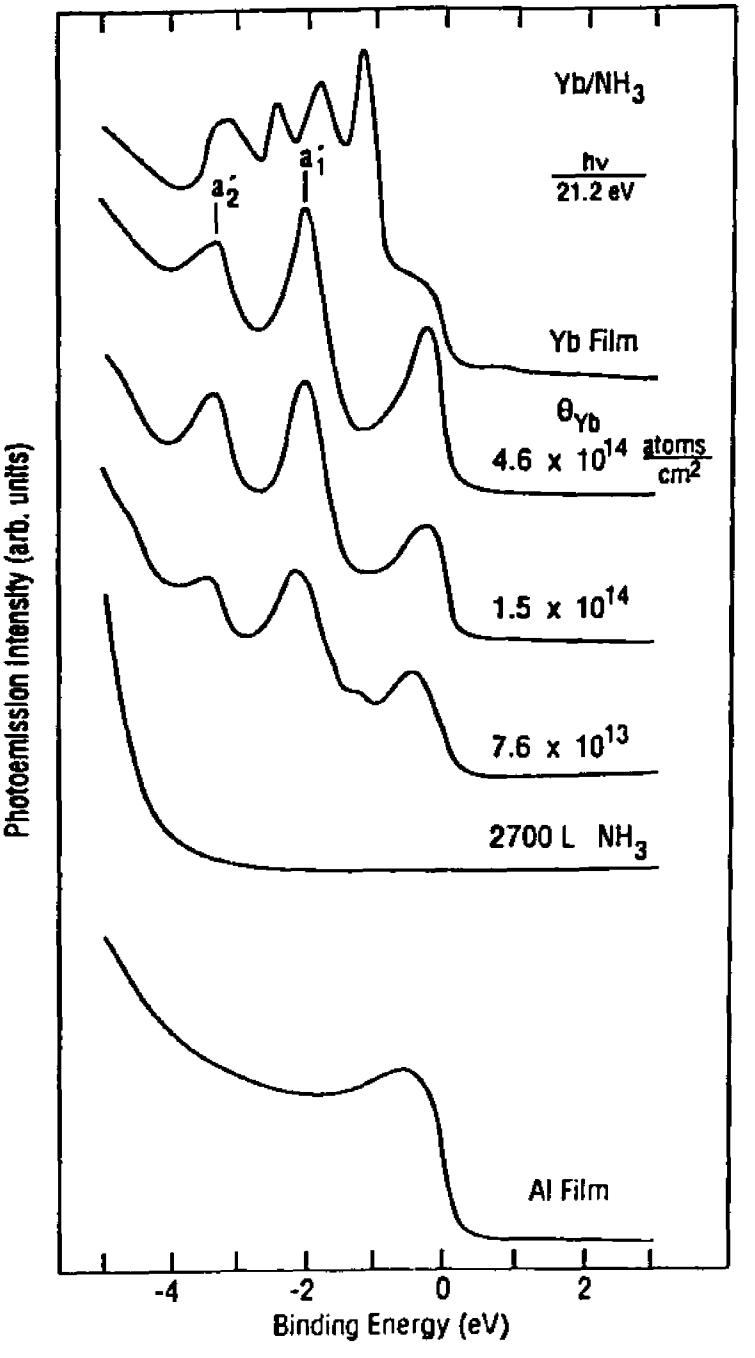

Figure 6.5. Valence band photoemission from ytterbium isolated in solid ammonia at 80 K [6.23].

Coincidently, Yb^{2+} also has a closed $4f^{14}$ shell and shows a 4f doublet. Hence, the observation of a doublet 4f spectrum for Yb isolated in C_{60} could imply that the ytterbium is divalent or atomic Yb^0. A way to discriminate between the atomic and divalent ytterbium is to look for the 6s state which appears at a 2 eV smaller binding energy. It is almost as intense as the 4f features at a photon energy of 27 eV.

The spectra for ytterbium isolated in solid ammonia are very different from those of ytterbium in xenon. Figure 6.5 shows photoemission data for ytterbium in ammonia. The 4f peaks (marked as a_1' and a_2') are a clear doublet and are at a higher binding energy than those of metallic ytterbium. An additional peak is seen near the Fermi edge. This feature was interpreted as a two electron shake down feature rather than a state related to the Yb-NH_3 bond because ammonia is a close shell molecule. The feature has a strong cross sectional dependence and nearly vanishes at 62 eV photon energy. The peak was not interpreted as the Yb 6s state because the feature at 5 eV binding energy, which can be interpreted as ytterbium in its trivalent configuration, was detected. The existence of ytterbium in the trivalent state implies that ytterbium has holes in the 4f states and makes it unlikely the 6s state would be occupied.

Figure 6.6 shows a plausible fitting of the electronic structure within -4 eV binding energy of Fermi level. This helps to identify contributions from the fullerene π states, the Yb 4f states and any new features due to the interaction between ytterbium and fullerene. The fullerene π states are at -1.8 and -3.1 eV binding energy. The initial 2 Å ytterbium deposition causes the π states to broaden about 50% and shift 0.3 eV to higher binding energy. To achieve a satisfactory fit, another doublet had to be added at the position expected for the 4f states characteristic of divalent ytterbium (peak C in Figure 6.3). In addition, the inelastic background had to be increased substantially. At this point, no additional features assigned to the Yb-C_{60} interaction were observed. When the ytterbium coverage was increased to 4 Å, the Yb 4f levels increased in intensity in proportion to the coverage, the fullerene π features became smaller relative to the scattered electron background, and a new component (marked as B) had to be introduced to account for increased emission between Fermi level and -1.0 eV binding energy. The new new feature can be approximated by a Voigt function centered at -0.5 eV binding energy. Our resolution is marginal for making a judgement about the existence of a Fermi edge. However, the

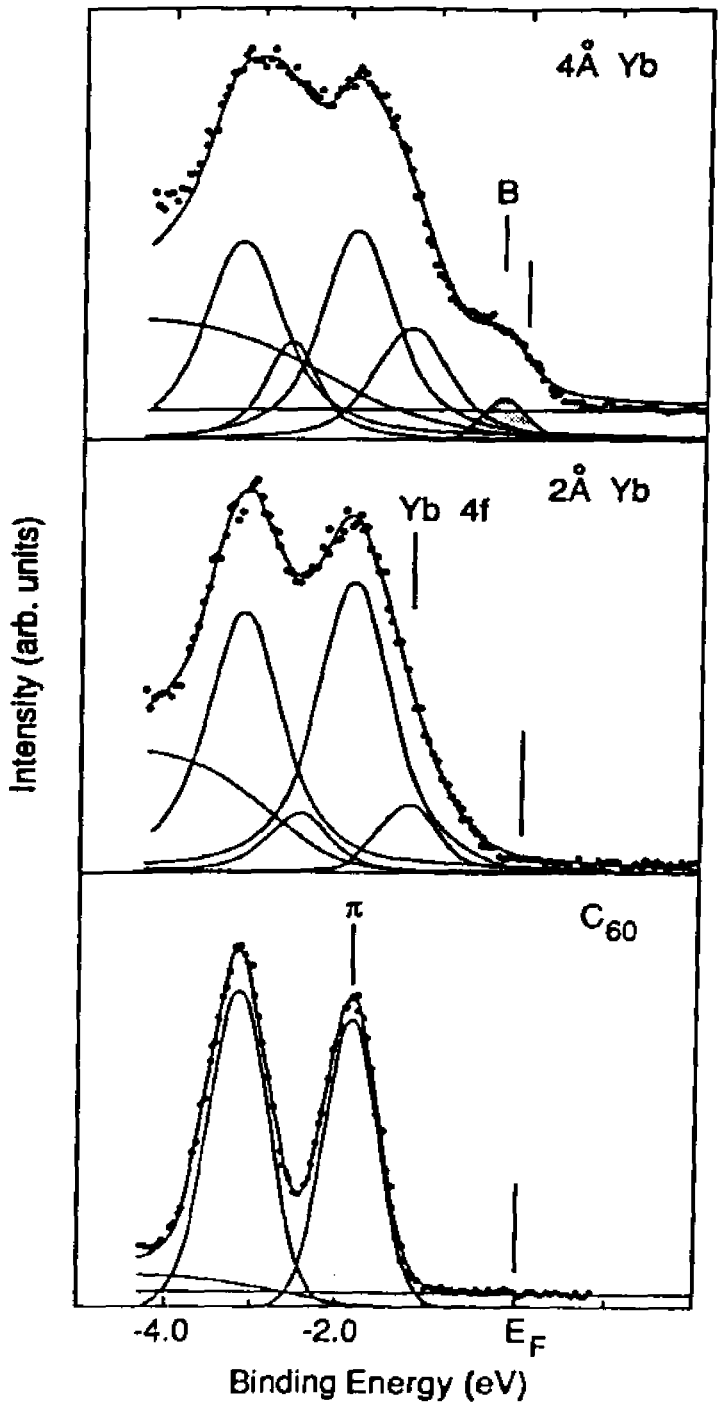

Figure 6.6 Computer based fitting of the valence states 0 - 4 eV below the Fermi level for Yb deposited on C_{60}.

fit by the symmetric Voigt function argues against the existence of a Fermi edge like that seen in detailed scans of the K or Rb induced metallic phase [6.8].

The results of the fitting should be compared to the data shown in figure 6.5 for for Yb/NH_3. It is clear there are some similarities that should be pointed out. In both cases, the Yb 4f states are a doublet but the Yb 4f states appear to be about an electron volt closer to the Fermi level for Yb/C_{60} and Yb/NH_3. In addition, both Yb/C_{60} and Yb/NH_3 develop another peak near the Fermi level. For Yb/NH_3 we believe these changes are related to the removal of some charge from the ytterbium to the ammonia. In the case of ytterbium in fullerene, we feel that similar behavior can occur. The relative positions of the fullerene and metal p, d and f states have a large impact on the sort of interactions and bonding that can be expected in the $Yb\text{-}C_{60}$ compound. From the placement of the highest energy occupied fullerene state relative to Fermi level (Figure 6.3, peak A), it can be shown that the lowest energy unoccupied fullerene states, the π^* level lays very close to the Fermi level of ytterbium. Under such circumstances the π^* level should hybridize with the metal states just above and below Fermi level to form a bonding level or resonance in the metal bands below Fermi

level [6.22, 6.24]. Above Fermi level, one or more unoccupied states with metal and π^* character should also form. The physical character of this interaction is different than that found for alkali metals in the fullerenes. In the later case, the alkali metal s band lies at least 1 eV above the fullerene π^* level. The large electron affinity of the fullerene relative to the alkali metal and the alkali metal's small first ionization potentials lead to the thorough ionization of alkali metal. In the specific case of Yb/C_{60}, it is conjectured from the initial placement of the π^* level relative to the Fermi level and the occupied metal bands that covalent bonds form between ytterbium and fullerene. We believe the small peak marked B in figure 6.6 is the bonding feature between fullerene and ytterbium and speculate that the π^* resonance seen in NEXAFS [6.8] will be smaller and close to the threshold because the π^* level will be partially occupied by electrons from the Yb s states. The peak could also be a shake-down peak like that observed for ytterbium in ammonia. Although, we have fitted the states near the Fermi level with a small peak, a Fermi function could also have been chosen and in that case the states would represent those of a band crossing the Fermi level. In the latter case, the

feature might be states derived from the Yb-C_{60} interaction or states derived from Yb-Yb and be due to the formation of ytterbium clusters like those seen for Yb/Xe.

In summary, ytterbium interacts chemically with fullerenes to form a compound at room temperature. The Yb-C_{60} phase has a divalent or mixed divalent-trivalent ytterbium species. When the surface concentration exceeds that needed to form the ytterbium compound, phase separation occurs and metallic clusters or islands grow on the surface. Computer-based analysis of the valence states near Fermi level suggests that the interaction between ytterbium and fullerene leads to the formation of a feature about 0.5 eV below the Fermi level. We interpret this feature as being either a Yb-C_{60} bonding related feature or a two electron (shake down) satellite. If the feature is bonding related, it could resemble the fullerene-derived peak seen for K_6C_{60} and other non-metallic metal fullerides. It should also be noted that the states near the Fermi level could also be fitted using a Fermi function and its appearance could also imply the formation of ytterbium metallic clusters. A study of the deposition of fullerene on ytterbium shows that the surface electronic state of ytterbium changes and the fullerene is chemisorbed.

References

1.1. V. I. Goldanskii, L. I. Trakhtenberg and V. N. Fleurov, Tunneling Phenomena in Chemical Physics, Gordon and Breach Science Publishers, (1989).

1.2. S. L. Qiu, M. W. Ruckman and M. Strongin, J. Vac. Sci. Technol. A 9(3), 1645 (1991).

1.3. S. L. Qiu, C. L. Lin, L. Q. Jiang and M. Strongin, Phys. Rev. B 39, 1958 (1989).

1.4. J. Jortner, J. Chem. Phys. 30, 839 (1959).

1.5. C. J. Adkins, J. Phys. C: Solid State Physics 20, 235 (1987).

2.1. A. Shal'nikov, Nature 142, 74 (1938).

2.2. W. Buckel and R. Hilsch, Z. Phys. 138, 109 (1954).

2.3. M. Strongin, R. S. Thompson, O. F. Kammerer and J. E. Crow, Phys. Rev. B1, 1078 (1970).

2.4. R. C. Dynes, A. E. White, J. M. Graybeal and J. P. Garno, Phys. Rev. Lett. 57, 2195 (1986).

2.5. C. A. Neugerbauer, Physics of Thin Films, Vol.II, G. Haas and R. Turn, eds. Academic, New York, (1964).

2.6. B. Abeles, P. Sheng, M. D. Coutts and Y. Arie, Adv. Phys. 24, 407 (1975).

2.7. Y. Shaperia and G. Deutscher, Phys. Rev. B 27, 4436 (1983).

2.8. P. Sheng, B. Abeles and Y. Arie, Phys. Rev. Lett. 31,44 (1973).

2.9. C. J. Adkins, J. M. D. Thomas and M. N. Young, J. Phys. C 13, 3427 (1980).

2.10. T. Chui, G. Lindenfeld and W. L. McLean, Phys. Rev. B 23, 6172 (1981).

2.11. B. I. Belvtsev, Y. F. Komnik and A. V. Fomin, J. Low Temp. Phys. 69, 401 (1987).

2.12. A. Miller and E. Abrahams, Phys. Rev. 120, 745 (1960).

2.13. N. F. Mott and E. A. Davis, "Electronic Processes in Non-Crystalline Materials", (Clarendon Press, Oxford), (1971).

2.14. N. F. Mott, J. non-crystal. Solids 1, 1 (1968).

2.15. N. F. Mott, Phil. Mag. 34, 911 (1969).

2.16. V. Ambegaokar, B. I. Halperin, and J. S. Langer, Phys. Rev. B 4, 2612 (1971).

2.17. C. A. Neugebauer, and M. B. Webb, J. appl. Phys. 33, 74 (1962).

2.18. R. M. Hill, Proc. R. Soc. A 309, 377 (1969).

2.19. A. L. Efros and B. I. Shklovskii, *J. Phys. C: Solid State Phys.* Vol. 8, L49 (1975).

3.1. N. J. Shevchik, J. Electron Spectroscopy and Related Phenom. 14, 411 (1978).

3.2. T. Koopmans, *Physica* 1, 104 (1934).

3.3. A. Zangwill, *Physics at Surfaces*. pp. 21. Cambridge: Cambridge University Press (1988).

3.4. T. N. Rhodin, and J. W. Gadzuk, In *The Nature of the Surface Chemical Bond* (eds. Rhodin and Ertl), pp. 113-273. Amsterdam: North-Holland (1979).

3.5. G. A. Somojai, *Chemistry in Two Dimensions: Surfaces*. Ithaca: Cornell (1981), p. 124.

3.6. D. R. Penn, *Phys. Rev.* B13, 5248 (1976).

3.7. C. N. Berglund and W. E. Spicer, *Phys. Rev.* 136, A 1030 (1964).

3.8. N. V. Smith, *Crit. Rev. Sol. State Sci.* 2, 45 (1972).

3.9. A. Rosen and I. Lindgren, *Phys. Rev.* 176, 114 (1968).

3.10. D. A. Shirley, *Chem. Phys. Lett.* 16, 220 (1972).

3.11. A. Barrie, *Chem. Phys. Lett.* 19, 109 (1973).

3.12. R. Holm and S. Storp, in: *Ullmanns Enzyklopadie der Technischen Chemie* Vol. 5. Verlag Chemie, Weinheim 1980, p. 519.

3.13. W. Kossel, *Z. Physik.* 1, 119 (1920).

3.14. R. de L. Kronig, *Z. Physik* 70, 317 (1931).

3.15. D. E. Sayers, E. A. Stern and F. W. Lytle, *Phys. Rev. Lett.* 27, 1204 (1971).

3.16. P. A. Lee and G. Beni, *Phys. Rev.* B 15, 2862 (1977).

3.17. C. A. Ashley and S. Doniash, *Phys. Rev.* B 11, 1279 (1975).

3.18. E. A. Stern, D. E. Sayers and F. W. Lytle, *ibid.* 11, 4836 (1975).

3.19. J. Stohr, *NEXAFS Spectroscopy*. Springer Verlag, Heidelberg (1992), p. 155.

3.20. J. Stohr, K. Baberschke, R. Jaeger, R. Treichler, and S. Brennani, *Phys. Rev. Lett.* 47, 381 (1981).

3.21. J. Stohr, F. Sette and A. L. Johnson, *Phys. Rev. Lett.* 53, 1684 (1984).

3.22. F. Sette, J. Stohr and A. P. Hitchcock, *Chem. Phys. Lett.* 110, 517 (1984).

3.23. J. Stohr, J. L. Gland, W. Eberhardt, D. Outka, R. J. Madix, F. Sette, R. J. Koestner and U. Doebler, *Phys. Rev. Lett.* 51, 2414 (1983).

3.24. J. Stohr and D. A. Outka, *Phys. Rev.* B 36, 7891 (1987).

3.25. R. Z. Bachrach and A. Bianconi, in *Proceedings of the Fifth International Conference on Vacuum Ultraviolet Radiation Physics*, edited by M. C. Castex, M. Pouey

and N. Pouey, Montpellier, France, 1977, Vol. 2, p. 213.

3.26. J. Stohr, C. Noguera and T. Kendelewicz, *Phys. Rev.* B 30, 5571 (1984).

4.1. J. G. Skofronick and W. B. Phillips, *Appl. Phys. Lett.* 7, 249 (1965).

4.2. C. A. Neugebauer and M. B. Webb, *J. Appl. Phys.* 33, 74 (1962).

4.3. T. Chui, G. Deutscher, P. Lindenfeld and W. L. McLean, *Phys. Rev.* B 23, 6172 (1981).

4.4. W. Buckel, *Z. Physik.* 138, 136 (1954).

4.5. G. Bergmann, *Phys. Reports* 4, 159 (1976).

4.6. H. M. Jaeger, D. B. Haviland, B. G. Orr and A. M. Goldman, *Phys. Rev.* B 40, 182 (1989).

4.7. M. Strongin, R. S. Thompson, O. F. Kammerer and J. E. Crow, *Phys. Rev.* B 1, 1078 (1970).

4.8. S. L. Qiu, C. L. Lin, L. Q. Jiang and M. Strongin, *Phys. Rev.* B 39, 1958 (1988).

4.9. K. L. Chopra, *Thin Film Phenomena*. p. 164 (1969). New York: Mcgraw-Hill Book Company.

4.10. C. J. Adkins, *J. Phys. C: Solid State Phys.* 20, 235 (1987).

4.11. P. Sheng and B. Abeles, *Phys. Rev. Lett.* 28, 34 (1972).

4.12. J. Marcoux, *Canadian Journal of Physics*. Vol. 40, 244 (1970).

4.13. R. L. Amey and H. R. Cole, *J. Chem. Phys. 40*, 146 (1964).

4.14. K. Van Steensel, *Phillips Res. Rept*. 22, 246 (1967).

5.1. R. Nurnberger, F. J. Himpsel, E. E. Koch and N. Schwentner, Phys. Status Solidi (b) 81, 503 (1977).

5.2. P. R. Norton, R. L. Tapping, H. P. Broida, J. W. Gadzuk and B. J. Waclawski, Chem. Phys. Lett. 53, 465 (1978).

5.3. S. L. Qiu, C. L. Lin, J. Chen and M. Strongin, Phys. Rev. B 41, 7467 (1990).

5.4. D. Schmeisser and K. Jacobi, Chem. Phys. Letters 62, 51 (1979).

5.5. K. Jacobi, D. Schmeisser and D. M. Kolb, Chem. Phys. Lett. 69, 113 (1980).

5.6. S. L. Qiu, C. L. Lin, J. Chen and M. Strongin, Phys. Rev. B 39, 6194 (1989).

5.7. V. I. Goldanskii, M. D. Frank-Kamenetskii and I. M. Barkalov, Science 182, 1344 (1973).

5.8. W. Gross and U. Schindewolf, J. Phys. Chem. 84, 1266 (1980).

5.9. L. Lee, J. Arias, C. Hanrahan, R. M. Martin and H.

Metin, Surface Sci. 165, L95 (1986).

5.10. G. B. Fisher, Chem. Phys. Lett. 79, 452 (1981).

5.11. P. S. Bagus, K. Hermann and C. W. Bauschlicher, Jr., J. Chem. Phys. 81, 1966 (1984).

5.12. K. Hermann, P. S. Bagus and C. W. Bauschlicher, Jr., Phys. Rev. B 31, 6371 (1985).

5.13. P. S. Bagus and K. Hermann, Phys. Rev. B 33, 2987 (1986).

5.14. G. B. Fisher and G. E. Mitchell, J. Electron Spectrosc. Related Phenomena 29, 253 (1983).

5.15. I. C. Bassignana, K. Wagemann, J. Kuppers and G. Ertl, Surface Sci. 175, 22 (1986).

5.16. C. Klauber, M. D. Alvey and J. T. Yates, Jr., Chem. Phys. Letters 106, 477 (1984).

5.17. T. E. Madey and C. Benndorf, Surface Sci. 152/153, 587 (1985).

5.18. B. A. Sexton and G. E. Mitchell, Surface Sci. 99, 523 (1980).

5.19. D. Lackey, M. Surman and D. A. King, Vacuum 33, 867 (1983).

5.20. J. L. Gland, B. A. Sexton and G. E. Mitchell, Surface Sci. 115, 623 (1982).

5.21. S. T. Ceyer and J. T. Yates, Jr., Surface Sci. 155, 584

(1985).

5.22. R. N. Barnett, Uzi Landman and A. Nitzan, Phys. Rev. Letters 62, 106 (1989).

5.23. L. G. Petersson and S. E. Kralsson, Phys. Scr. 16, 425 (1977).

5.24. W. Jorgensen and L. Salem, The Organic Chemist's Handbook of Orbitals, p.213, Academic, New York, 1971.

5.25. T. Kawai, K. Kunimori, T. Kondow, T. Onishi and K. Tamaru, Phys. Rev. Letters 33, 533 (1974).

5.26. E. W. Plummer and W. Eberhardt, Advances in Chemical Physics 49, 533 (1982).

5.27. M. Grunze, F. Bozso, G. Ertl and M. Weiss, Appl. of Surface Science 1, 241 (1978).

5.28. P. T. Dawson and R. S. Hansen, J. Chem. Phys. 48, 623 (1968).

5.29. M. Wilf and M. Folman, J. Chem. Soc., Faraday Trans. 1, 72 (1976) 1165.

5.30. F. P. Netzer and T. E. Madey, Surface Sic. 119, 422 (1982).

5.31. G. R. Wight and C. E. Brion, J. Electron Spectroscopy 4, 25 (1974).

5.32. A. P. Hitchcock and C. E. Brion, J. Electron

Spectroscopy 18, 1 (1980).

5.33. M. B. Robin, Higher Excited States of Polyatomic Molecules, Vol. 1. Academic, New York, 1974.

5.34. J. L. Dehmer and D. Dill, J. Chem. Phys. 65, 5327 (1976).

5.35. R. Arneberg, H. Agren, J. Muller and R. Manne, Chem. Phys. Lett. 91, 362 (1982).

5.36. L. Ungier and T. d. Thomas, Phys. Rev. Lett. 533, 435 (1984).

5.37. L. J. Medhurst, T. A. Ferrett, P. A. Heimann, D. W. Lindle, S. H. Liu and D. A. Shirley, J. Chem. Phys. 89, 6096 (1988).

5.38. R. A. Rosenberg, V. Rehn, A. K. Green, P. R. LaRoe and C. C. Parks, in Proc. First International Workshop on Desorption Induced by Electronic Transitions, DIET-1, Williamsburg, VA, 1982.

5.39. J. Chen, C. L. Lin, S. L. Qiu, M. Strongin and M. L. denBoer, J. Vac. Sci. Technol. A8, 2591 (1990).

5.40. W. R. Harshbarger and E. N. Lassettre, J. Chem. Phys. 58, 1505 (1973).

5.41. W. R. Harshbarger, J. Chem. Phys. 54, 2504 (1971).

5.42. Chi-Chang Kao, Steven L. Hulbert and Erik D. Johnson, BNL-42689, Informal Report, 1989.

5.43. J. Stohr, NEXAFS Spectroscopy. Springer Verlag, Heidelberg (1992), p. 423.

5.44. J. Jortner, J. Chem. Phys. 30, 839 (1959).

5.45. M. H. Cohen and J. C. Thompson, Adv. Phys. 17, 875 (1968).

5.46. L. Ley and M. Cardona, Photoemission in solid, Springer-Verlag, (1979), p. 1.

5.47. S. L. Qiu, C. L. Lin, L. Q. Jiang and M. Strongin, Phys. Rev. B 39, 1958 (1988).

5.48. N. F. Mott, *Trans. Faraday Soc.* Vol. 43. p. 429 (1947).

5.49. F. P. Fehlner and N. F. Mott, *Oxidation of Metals.* Vol. 2, No. 1, 59 (1970).

5.50. E. J. Kirschke and W. L. Jolly, Inorganic Chemistry 6, 855 (1967).

5.51. G. Ertl and M. Huber, J. Catal. 61, 537 (1980).

5.52. E. Shustorovich and A. T. Bell, Surface Sci. Lett. 259, L791 (1991).

5.53. L. V. Coulter, J. Phys. Chem. 57, 553 (1953).

5.54. W. L. Jolly, Chem. Revs. 50, 351 (1952).

6.1. H. W. Kroto, J. R. Heath, S. C. O'Brien, R. F. Curl and R. E. Smalley, Nature 318, 162 (1985).

6.2. W. Kratschmer, L. D. Lamb, K. Fostiropoulos and D. R.

Huffman, Nature 347, 354 (1990).

6.3. D. R. Huffman, Physics Today 44, 22 (1991).

6.4. P. A. Heiney, Condensed Matter News, Vol.1, No. 4,25 (1992).

6.5. A. F. Hebard, M. J. Rosseinsky, R. C. Haddon, D. W. Murphy, S.H. Glarum, T. T. M. Palstra, A. P. Ramirez and A. R. Kortan, Nature 350, 600 (1991).

6.6. R. C. Haddon, A. F. Hebard, M. J. Rosseinsky, D. W. Murphy, S. J. Duclos, K. B. Lyons, B. Miller, J. M. Rosamilia, R. M. Fleming, A. R. Kortan, S. H. Glarum, A. V. Makhija, A. J. Muller, R. H. Eick, S. M. Zahurak, R. Tycko, G. Dabbagh and F. A. Thiel, Nature 350, 320 (1991).

6.7. K. Holczar, O. Klein, S. M. Huang, R. B. Kaner, K. J. Fu, R. L. Whetten and F. Diederich, Science 252, 1154 (1991).

6.8. C. T. Chen, L. H. Tjeng, P. Rudolf, G. Meigs, J. E. Rowe, J. Chen, J. P. McCauley, Jr., A. B. Smith III, A. R. McGhie, W. J. Romanow and E. W. Plummer, Nature 352, 603 (1991).

6.9. P. J. Benning, J. L. Martins, J. H. Weaver, L. P. F. Chibante and R. E. Smalley, Science 252, 603 (1991).

6.10. C. Gu, F. Stepniak, D. M. Poirier, M. B. Jost, P. J.

Benning, Y. Chen, T. R. Ohno, J. L. Martins, J. H. Weaver, J. Fure and R. E. Smalley, Phys. Rev. B 45, 6348 (1992).

6.11. A. R. Kortan, N. Kopylov, S. Glarum, E. M. Gyorgy, A. P. Ramirez, R. M. Fleming, F. A. Thiel and R. C. Haddon, Nature 355, 529 (1992).

6.12. Y. Chen, F. Stepniak, J. H. Weaver, L. P. F. Chibante and R. E. Smalley, Phys. Rev. B 45, 8845 (1992).

6.13. A. Bharathi, C. S. Sundar, Y. Hariharan, V. S. Shastry, J. Geethakumary, J. Janaki, T. S. Radhakrishnan, A. L. F. Terrance, V. S. Raghumathan and M. C. Valsakumar, High T_c Update 6, 13 (1992).

6.14. A. Fujimori, T. Shimzu and T. Yasuoka, Phys. Rev. B 35, 8945 (1987).

6.15. T. R. Ohno, G. H. Kroll, J. H. Weaver, L. P. F. Chibante and R. E. Smalley, Phys. Rev. B 46, 10437 (1992).

6.16. W. A. Svensson, M. O. Krause, T. A. Carlson, V. Radojevic and W. R. Johnson, Phys. Rev. A 33, 1024 (1986).

6.17. E. J. Cho, J. S. Chung, S. J. Oh, S. Suga, M. Taniguchi, A. Kakizaki, A. Fujimori, H. Kato, T. Miyahara, T. Suzuki and T. Kasuya, Phys. Rev. B 47,

3933 (1993).

6.18. A. Nilsson, B. Erikson, N. Mattensson, J. N. Andersen and J. Onsgaard, Phys. Rev. B 38, 10357 (1988).

6.19. J. H. Weaver, J. L. Martins, T. Komeda, Y. Chen, T. R. Ohno, G. H. Kroll, N. Troullier, R. E. Haufler and R. E. Smalley, Phys. Rev. Lett. 66, 1741 (1991).

6.20. P. J. Benning, D. M. Poirier, N. Troullier, J. L. Martins, J. H. Weaver, R. E. Haufler, L. P. E. Chibante and R. E. Smalley, Phys. Rev. B 44, 1962 (1991).

6.21. J. L. Martins, N. Troullier and J. H. Weaver, Chem. Phys. Lett. 180, 457 (1991).

6.22. P. J. Benning, D. M. Poirier, T. R. Ohno, Y. Chen, M. B. Jost, F. Stepniak, G. H. Kroll, J. H. Weaver, J. Fure and R. E. Smalley, Phys. Rev. B 45, 6899 (1992).

6.23. S. L. Qiu, V. Murgai, M. Strongin and M. W. Ruckman, to be published.

6.24. R. C. Haddon, Acc. Chem. Res. 25, 131 (1992).